공학박사 학위논문

Thermomechanical homogenization of fiber-reinforced composite materials using artificial intelligence

인공지능을 활용한 섬유강화 복합재료의
열기계적 균질화에 대한 연구

2023 년 2 월

서울대학교 대학원

재료공학부

최 재 혁

Thermomechanical homogenization of fiber-reinforced composite materials using artificial intelligence

인공지능을 활용한 섬유강화 복합재료의 열기계적 균질화에 대한 연구

지도교수 유 웅 열

이 논문을 공학박사 학위논문으로 제출함

2023 년 2월

서울대학교 대학원

재료공학부

최 재 혁

최재혁의 공학박사 학위논문을 인준함

2023 년 2월

위 원 장	안 철 희	(인)
부 위 원 장	유 웅 열	(인)
위 원	이 명 규	(인)
위 원	나 원 진	(인)
위 원	홍 석 빈	(인)

Abstract

Thermomechanical homogenization of fiber-reinforced composite materials using artificial intelligence

Jae-Hyuk Choi

Department of Materials Science and Engineering

College of Engineering

The Graduate School

Seoul National University

Fiber-reinforced plastics (FRPs) have replaced metals in various industrial products to achieve weight reduction due to their excellent specific properties (i.e., high mechanical properties and low density). The capability to predict the homogenized thermomechanical properties of FRPs is essential to facilitate the product design process. Prediction of these effective properties, however, is not straightforward due to the microstructural variation of fibers (e.g., arrangement, orientation, or size) in FRPs. In this study, a machine learning-assisted thermomechanical homogenization framework considering the microstructural variation, which can calculate the effective thermomechanical properties with high accuracy, will be presented.

In Chapter 2, a machine learning-assisted tensile strength prediction model of unidirectional (UD) FRP considering the randomness of the

microstructural fiber array is proposed. Stress concentration factor (SCF) generated by the broken fiber is a dominating feature to determine the tensile strength of UD FRP. In general, however, no analytical model has been proposed for SCF calculation in randomly distributed fibers in UD composite. The author proposes a novel machine learning-assisted modelling of SCF in UD composites. Extensive finite element simulations were performed, calculating SCF for UD composites with various random fiber arrays. Then, an artificial neural network (ANN) was trained with the obtained SCF data and used it to predict the SCF for composites with an arbitrary random fiber array. A tensile strength prediction model was developed based on a new recurrence relation for fiber fracture propagation and a determination algorithm for the fracture sequence for random fiber arrays. The tensile strength of UD composites was predicted over a range of values, demonstrating that accuracy was superior to conventional prediction methods.

In Chapter 3, a machine-learning assisted two-step homogenization framework for short fiber-reinforced plastics (SFRPs) is proposed. Consideration of orientation is very important because the anisotropy of thermomechanical properties is differently generated depending on the orientation of inclusion. A series-parallel ANN system was constructed and trained to facilitate the time-consuming reconstruction of orientation distribution function and pseudograin decomposition procedures. Then, we implemented the series-parallel ANN system, Mori-Tanaka model, and Voigt model into ABAQUS user material subroutine (UMAT). The elastic modulus

values predicted by UMAT were in a good agreement with both DIGIMAT and experimental values, The low computation time of UMAT also justified the application of machine learning approach to the two-step thermo-mechanical homogenization framework.

In Chapter 4, the previously developed two-step homogenization framework for SFRP will be expanded to describe more general case by introducing the concept of interphase with constant nano-scale thickness between matrix and inclusion. This third phase enabled us to take inclusion size effect into account. The applicability of the extended three-phase homogenization framework in material design will be confirmed by comparing the effective thermomechanical properties obtained via finite element simulation.

Keywords: Fiber-reinforced plastics, composite materials, two-step homogenization, thermomechanical, microstructure, artificial neural network

Student Number: 2017-24086

Contents

List of Tables

List of Figures

Chapter 1. Introduction

1.1. Fiber-reinforced plastics (FRPs)

Fiber-reinforced plastic (FRP) or fiber-reinforced composite, comprised of polymer matrix and reinforcing fiber, have replaced metals in various industrial products to achieve weight reduction [14-22] due to their excellent specific properties (**Figure 1-1** [3]). Thermosetting polymers (e.g., epoxy, polyester, vinyl ester) or thermoplastic polymers (e.g., polypropylene, polyamide, polyether ether ketone) are widely used as matrix materials, while synthetic fibers (e.g., carbon, E-glass, aramid) or natural fibers (e.g., jute, flax, coir) are widely used as reinforcing materials.

FRPs can be categorized into continuous, discontinuous, and hybrid FRPs. Continuous and discontinuous FRPs are classified according to the length of the reinforced fibers (**Figure 1-2(a)** and **Figure 1-2(b)**). Hybrid FRPs are combination of multiple fiber types in a single matrix (**Figure 1-2(c)**) [4]. Continuous FRPs are manufactured via Hand Lay-up method, Vacuum-Assisted Resin Infusion (VARI), Resin Transfer Molding (RTM), Vacuum-assisted resin transfer molding (VARTM), Pre-impregnated (prepreg) form, Compression Molding, or Autoclave Molding etc. Discontinuous FRPs are manufactured via Extrusion Compounding, or Injection Molding etc.

The thermomechanical properties of FRPs strongly depend on the properties of constituents, relative volume fractions, microstructural information (e.g., orientation distribution, shape, size of fibers). The

orientation of the reinforcing fibers definitely affects the isotropy of thermomechanical properties. Unidirectional (UD) FRP, which is a typical example of continuous FRPs with aligned reinforcing long fibers, exhibit anisotropic nature in general. UD FRP is used in the form of a cross-ply laminate with minimized anisotropy, unless it is used for a component that requires maximum properties in a specific direction. Short fiber-reinforced plastics (SFRPs), which is a typical example of discontinuous FRPs with randomly oriented reinforcing short fibers, exhibit isotropic nature in general. However, fibers may align in a specific direction due to the processing conditions and then the composites may become anisotropic. The main advantage of FRPs is that the thermomechanical properties can be controlled to have desired amount of anisotropy by designing and manufacturing FRPs with appropriate fiber orientation.

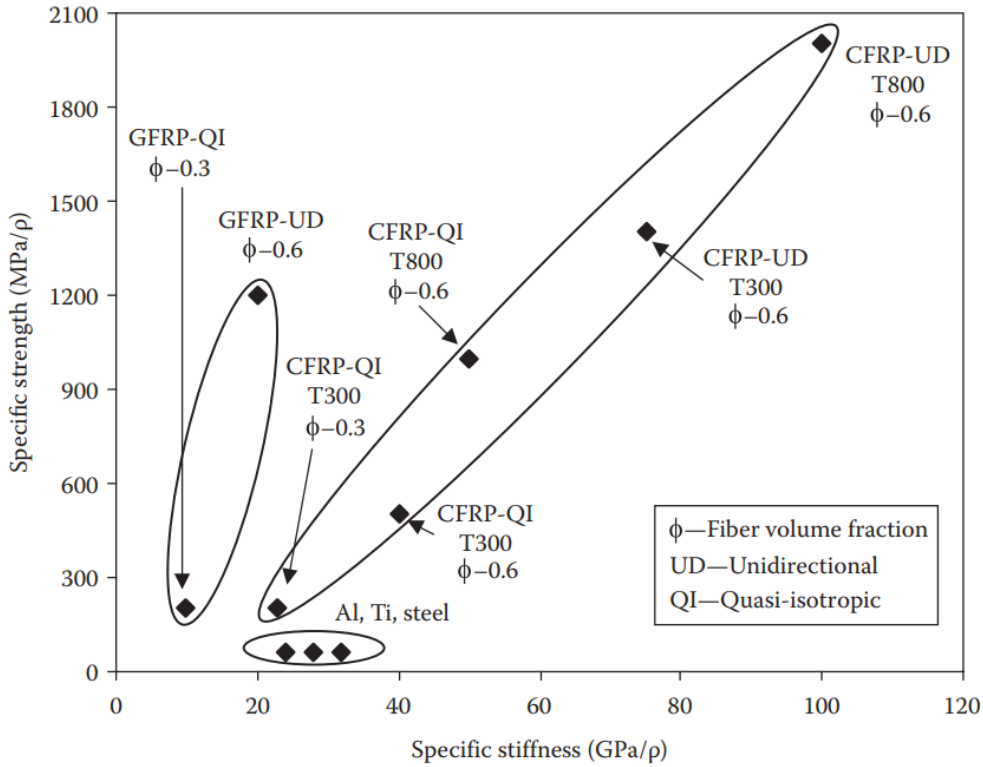

Figure 1-1 Specific strength and stiffness values of conventional materials and FRPs [3]

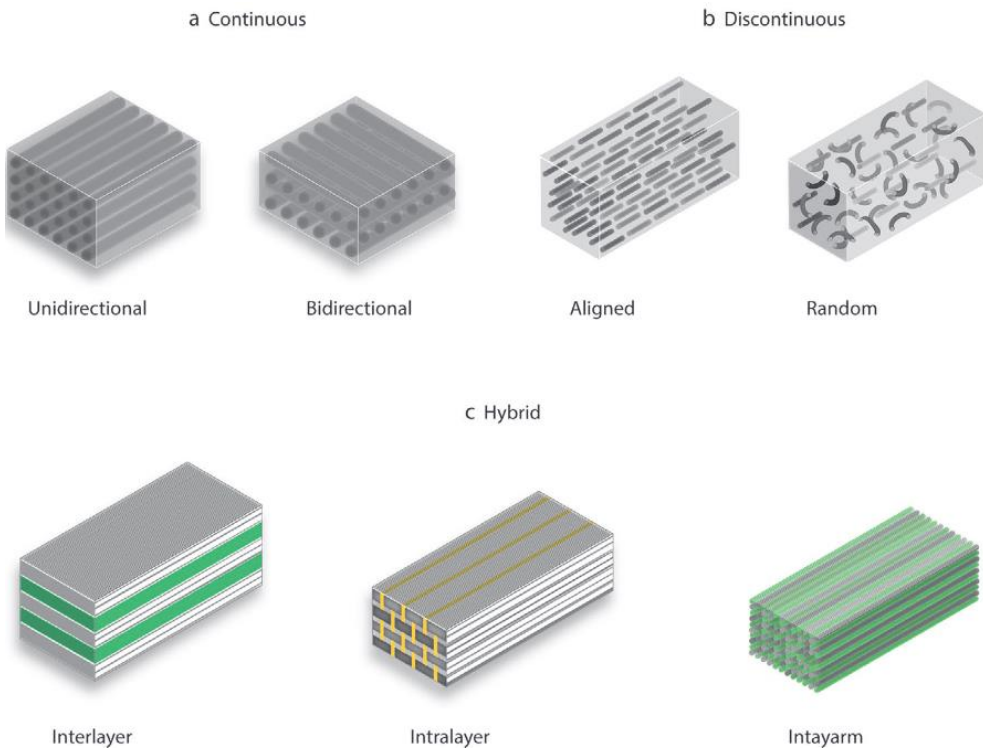

Figure 1-2 Schematic illustrations of FRP composites: (a) continuous FRP composites, (b) discontinuous FRP composites, (c) hybrid composites [4]

1.2. Artificial intelligence (AI) for FRPs

Artificial intelligence (AI) has been fundamental to almost all fields of science and engineering thanks to the recent advances in computing power. The term machine learning (ML), which is a branch of AI, was first introduced by Arthur Samuel, who defined machine learning as “A field of study that gives computers the ability to learn without being explicitly programmed” [23]. Alpaydin defined machine learning in other word that “Programming computers to optimize a performance criterion using example data or past experience” [24]. Naqa et al. summarized these various definitions that “Coaching computers to intelligently perform tasks beyond traditional number crunching by learning the surrounding environment through repeated examples” [25]. In other word, machine learning is a field of data science that predicts the outcome of future events based on given data (or experience) in similar situations. The general flow of machine learning is 1) accumulating data, 2) manipulating data, 3) training model, and 4) evaluation.

All the process parameters, including shape, size, composition of inclusions, should be considered for design, identification, and characterization of FRP materials since they greatly affect the overall properties of FRPs [26-29]. Traditionally, experiments have played a very important role in investigating such process parameters. However, defining a constitutive equation between these parameters is extremely strenuous, and

sometimes even impossible to define. Moreover, many experiments must be accompanied for reliable characterization, which usually requires enormous resources and time. To cope with such a high cost, researchers in the materials field are attempting an approach through experimentation and integration of computer simulations (i.e., computational prediction and experimental validation) when designing materials. Despite the recent advances in computing power, the limitations of computer simulation (e.g., Molecular Dynamics (MD) and finite element method (FEM)) that still requires a lot of computing resources have arisen the need for researchers to find an alternative solution. Application of the machine learning approaches, or data-driven strategies is widely studied nowadays [7, 30-39]. These strategies are composed of two steps. The first step is the generation of input dataset output (target) dataset. The second step is to establish a relation between input and target properties numerically (**Figure 1-3** [5]). Pattnaik et al. developed a flexible process methodology that can be used from the beginning of selection of raw materials to final output performance characteristics for laboratory scale applications, which also emphasizes the role of machine learning at the various stages of processing of FRPs (**Figure 1-4** [6]).

The outstanding point of using machine learning in the field of materials is that machine learning models trained with traditional input data can suggest unexpected composite designs with good or even higher properties. Gu et al. demonstrated a new bio-inspired hierarchical composite structure using machine learning approach (**Figure 1-5** [7]). They showed that their machine

learning-based model can generate a composite material with new microstructural patterns not included in the input data that has tougher and stronger properties.

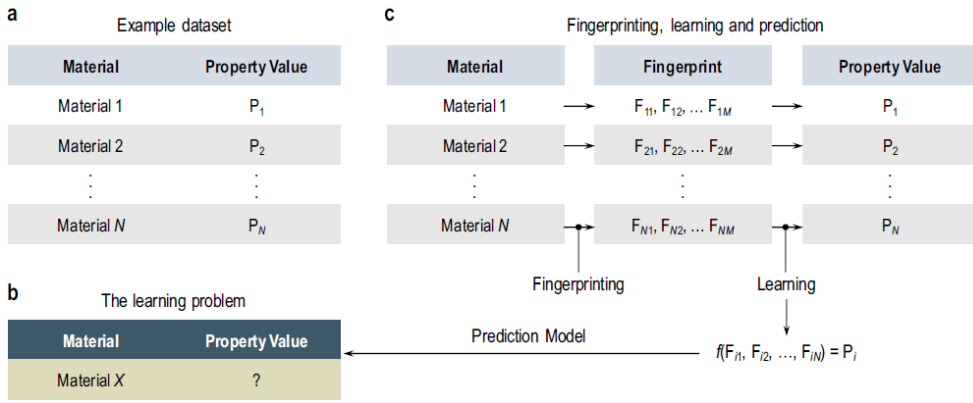

Figure 1-3 The key elements of machine learning in materials science, (a) schematic view of an example data set, (b) statement of the learning problem, and (c) creation of a surrogate prediction model via the fingerprinting and learning steps [5]

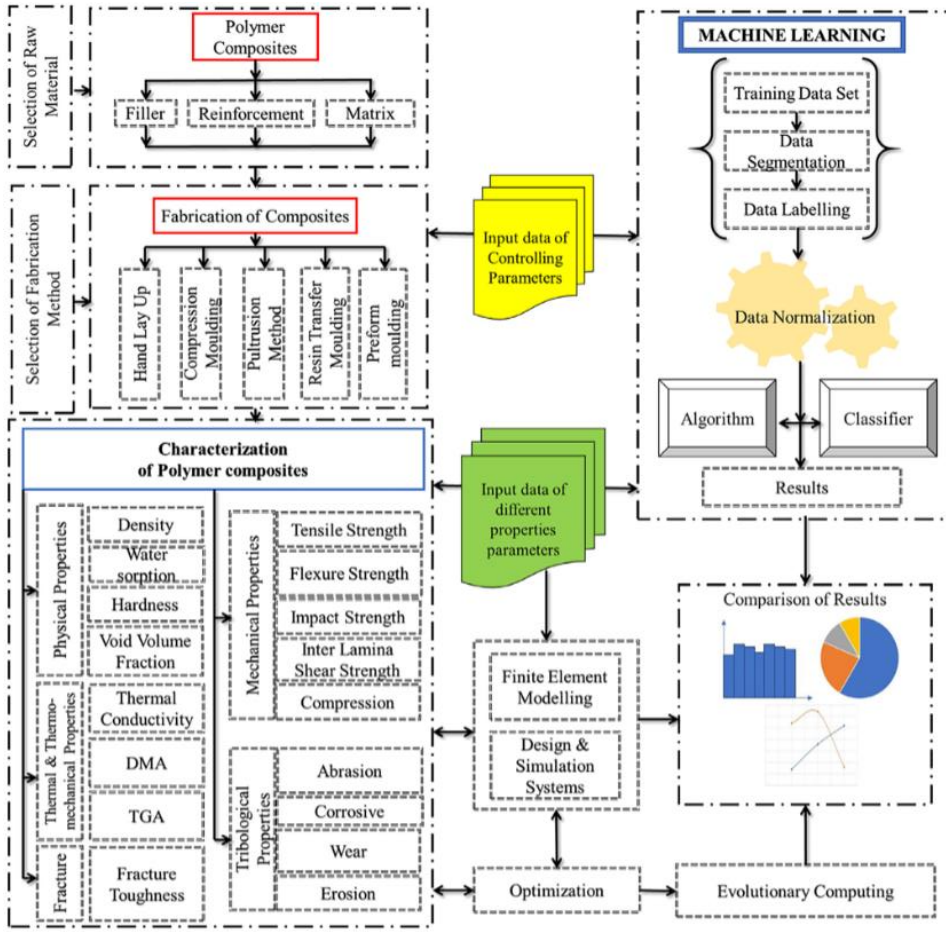

Figure 1-4 Role of machine learning in FRPs [6]

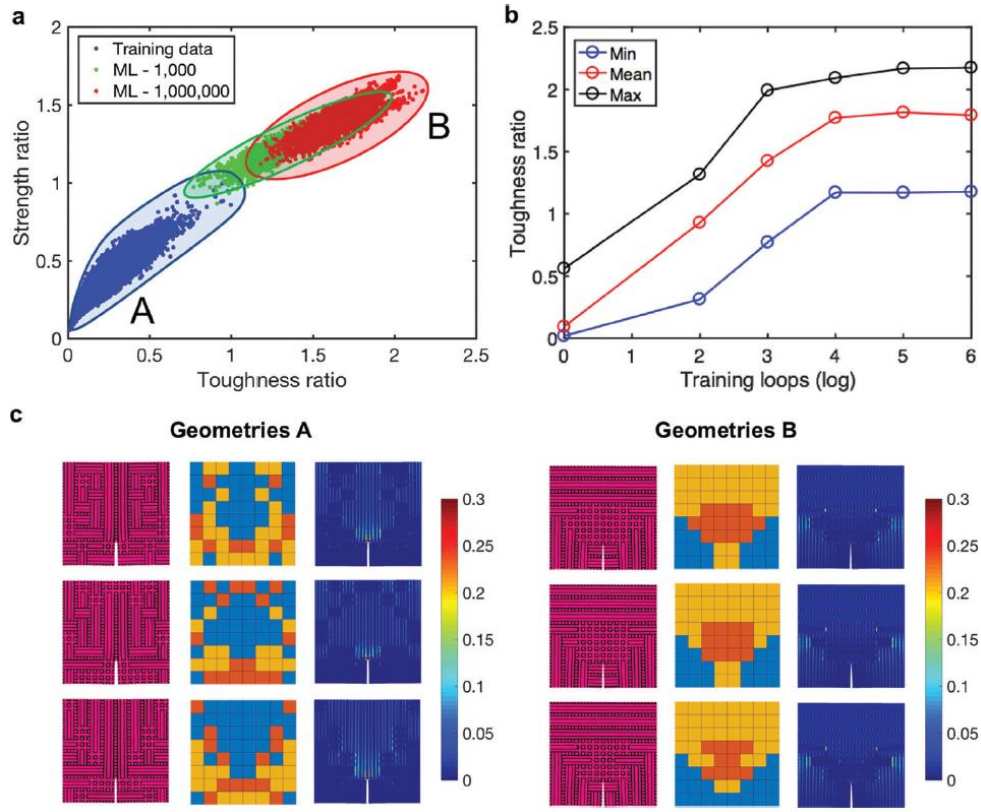

Figure 1-5 Machine learning generated designs, (a) strength and toughness ratios of designs computed from training data and ML output designs, (b) Effects of learning time on ML models, and (c) microstructures from partitions A and B [7]

1.3. Mean-field homogenization of FRPs

The mean-field homogenization based on Eshelby's single inclusion problem [40] is used to predict the effective thermomechanical properties of FRPs with arbitrary microstructures.

Consider a two-phase composite RVE with domain Ω and volume V consisting of the matrix phase (Ω_m and V_m) and inclusion phase (Ω_i and V_i). Both matrix and inclusion phases are assumed to be isotropic and elastic, and the interface between two phases is assumed to be perfectly bonded. The volume averaging operator quantity is defined as follows.

$$\langle \cdot \rangle_{\Omega} = \frac{1}{V} \int_{\Omega} (\cdot)_{\Omega} dV \qquad \textbf{Equation 1-1}$$

where $\cdot$ refers to an arbitrary integrable field. The relation between the volume average quantity of the RVE and matrix/inclusion can be expressed as follows.

$$\langle \cdot \rangle_{\Omega} = v_m \langle \cdot \rangle_{\Omega_m} + v_i \langle \cdot \rangle_{\Omega_i} \qquad \textbf{Equation 1-2}$$

where $v_m = V_m / V$ and $v_i = V_i / V$ are the volume fraction of matrix phase and inclusion phase, respectively. When the RVE exhibits the macro-strain field $\langle \varepsilon \rangle_{\Omega}$, the average micro-strain field in each phase can be correlated using the strain concentration tensor A^{ε} as follows.

$$\langle \varepsilon \rangle_{\Omega_i} = A^{\varepsilon} : \langle \varepsilon \rangle_{\Omega_m} \qquad \textbf{Equation 1-3}$$

Combining **Equation 1-2** with respect to the strain field and **Equation 1-3** provides the following two relations between the macro-strain field and the

micro-strain field in each phase:

$$\langle \varepsilon \rangle_{\Omega_m} = \left[\left(1 - v_i \right) I + v_i A^{\varepsilon} \right]^{-1} : \langle \varepsilon \rangle_{\Omega} \qquad \textbf{Equation 1-4}$$

$$\langle \varepsilon \rangle_{\Omega_i} = A^{\varepsilon} : \left[\left(1 - v_i \right) I + v_i A^{\varepsilon} \right]^{-1} : \langle \varepsilon \rangle_{\Omega} \qquad \textbf{Equation 1-5}$$

where I is the fourth-order symmetric identity tensor. Substituting Equation **Equation 1-4** and **Equation 1-5** into Equation **Equation 1-2** with respect to the stress field, we obtain,

$$\langle \sigma \rangle_{\Omega} = \left[\left(1 - v_i \right) C_m + v_i C_i : A^{\varepsilon} \right] : \left[\left(1 - v_i \right) I + v_i A^{\varepsilon} \right]^{-1} : \langle \varepsilon \rangle_{\Omega} \qquad \textbf{Equation 1-6}$$

where C_m and C_i are the stiffness tensor of the matrix and inclusion, respectively. Therefore, the effective stiffness tensor of the RVE $\langle C \rangle_{\Omega}$ is derived as follows.

$$\langle C \rangle_{\Omega} = \left[\left(1 - v_i \right) C_m + v_i C_i : A^{\varepsilon} \right] : \left[\left(1 - v_i \right) I + v_i A^{\varepsilon} \right]^{-1} \qquad \textbf{Equation 1-7}$$

Various homogenization models proposed thus far are distinguished by the definition of the strain concentration tensor A^{ε}, such as Generalized self-consistent model, Mori-Tanaka model, Voigt model, Reuss model, Bridging model, and Double inclusion model, etc. An exemplary comparison of these homogenization models in predicting the modulus of a composite materials is provided in **Figure 1-6** [8].

Among the various homogenization models, Mori-Tanaka model, and Voigt model, which is used in this study, will be explained in the following sections.

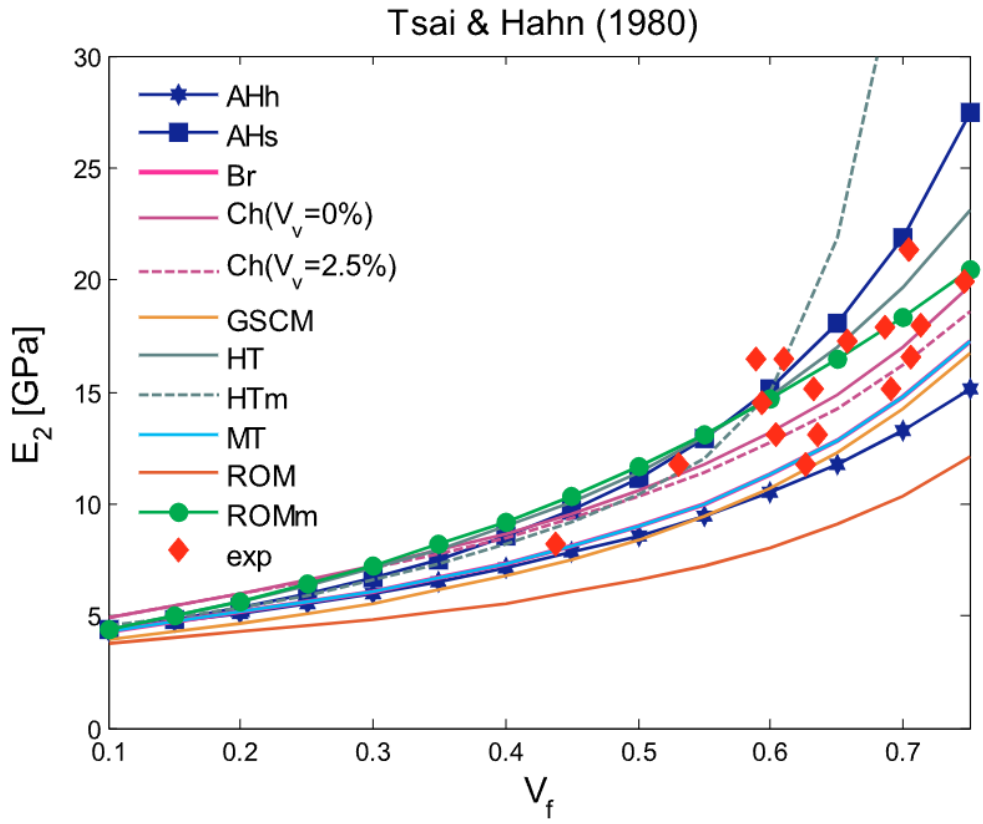

Figure 1-6 Example of the most traditional approach in micromechanics to compare models' predictions with experimental data [8]

1.3.1. Mori–Tanaka model

The Mori–Tanaka model [41, 42] assumes that each ellipsoidal inclusion is embedded in an infinite matrix, which is the same premise of Eshelby's single inclusion problem. Therefore, the Mori–Tanaka model is suitable for two-phase composites with a low volume fraction of approximately 30 % or less [43]. The single inclusion strain concentration tensor provided by the Mori–Tanaka model A^{ε}_{MT} is as follows.

$$A^{\varepsilon}_{MT} = \left[I + S : \left(C_m^{-1} : C_i - I \right) \right]^{-1} \qquad \textbf{Equation 1-8}$$

where S is Eshelby's tensor. The details of the Eshelby's tensor component for an ellipsoidal or cylindrical inclusion are discussed in **Section 1.3.3**. As described in the introduction, the Mori–Tanaka model was used in the first step of a two-step homogenization procedure in which each pseudograin is homogenized.

1.3.2. Voigt model

The Voigt model [44] adopts the iso-strain assumption that each phase of the two-phase composite has a parallel connection, which can be expressed as follows.

$$\langle \varepsilon \rangle_{\Omega} = \langle \varepsilon \rangle_{\Omega_m} = \langle \varepsilon \rangle_{\Omega_i} \qquad \textbf{Equation 1-9}$$

A comparison of **Equation 1-9** and **Equation 1-3** reveals that the strain concentration tensor of the Voigt model A^{ε}_{Voigt} should be identical with the fourth-order symmetric identity tensor I. Thus, **Equation 1-7** is simplified to

$$\langle C \rangle_{\Omega} = (1 - v_i) C_m + v_i C_i \qquad \textbf{Equation 1-10}$$

which is the final form of the Voigt model.

1.3.3. Eshelby tensor

The details of the Eshelby tensor's component for an ellipsoidal inclusion is provided by Mura's study [45].

Consider an ellipsoidal inclusion Ω_i (**Equation 1-11**) with principal half axes of $a_1 > a_2 > a_3$ in an isotropic infinite body, where Ω_i is given by,

$$x_1^2/a_1^2 + x_2^2/a_2^2 + x_3^2/a_3^2 \leq 1 \qquad \textbf{Equation 1-11}$$

Then, Green's function is defined by,

$$G_{ij}(x - x') = \frac{1}{16\pi\mu(1-v)|x-x'|}\left[(3-4v)\delta_{ij} + \frac{(x_i - x_i')(x_j - x_j')}{|x-x'|^2}\right] \qquad \textbf{Equation 1-12}$$

After some manipulation, one can obtain the strain components ($\varepsilon_{ij}(x)$) the surface integrals (I_1, I_{11}, and I_{12}) can be reduced to simple integrals based on an attractive conclusion that the strain and stress is uniform inside the inclusion as follows:

$$\varepsilon_{ij}(x) = \frac{\varepsilon_{mn}^*}{16\pi(1-v)} \int_{\mathbb{S}} \frac{\lambda_i g_{jmn} + \lambda_j g_{imn}}{g} d\omega \qquad \textbf{Equation 1-13}$$

$$I_1 = 2\pi a_1 a_2 a_3 \int_0^{\infty} \frac{ds}{\left(a_1^2 + s\right)\Delta s} \qquad \textbf{Equation 1-14}$$

$$I_{11} = 2\pi a_1 a_2 a_3 \int_0^{\infty} \frac{ds}{\left(a_1^2 + s\right)^2 \Delta s} \qquad \textbf{Equation 1-15}$$

$$I_{12} = 2\pi a_1 a_2 a_3 \int_0^{\infty} \frac{ds}{\left(a_1^2 + s\right)\left(a_2^2 + s\right)\Delta s} \qquad \textbf{Equation 1-16}$$

where $\Delta s=\left(a_1^2+s\right)^{1/2}\left(a_2^2+s\right)^{1/2}\left(a_3^2+s\right)^{1/2}$. These surface integrals are expressed by the standard elliptic integrals as follows.

$$I_1=\frac{4\pi a_1 a_2 a_3}{\left(a_1^2-a_2^2\right)\left(a_1^2-a_3^2\right)^{1/2}}\{F(\theta,k)-E(\theta,k)\} \qquad \textbf{Equation 1-17}$$

$$I_3=\frac{4\pi a_1 a_2 a_3}{\left(a_2^2-a_3^2\right)\left(a_1^2-a_3^2\right)^{1/2}}\left\{\frac{a_2\left(a_1^2-a_3^2\right)^{1/2}}{a_1 a_3}-E(\theta,k)\right\} \qquad \textbf{Equation 1-18}$$

If we write **Equation 1-13** as

$$\varepsilon_{ij}=S_{ijkl}\varepsilon_{kl}^{*} \qquad \textbf{Equation 1-19}$$

then,

$$S_{1111}=\frac{3}{8\pi(1-\nu)}a_1^2 I_{11}+\frac{1-2\nu}{8\pi(1-\nu)}I_1 \qquad \textbf{Equation 1-20}$$

$$S_{1122}=\frac{1}{8\pi(1-\nu)}a_2^2 I_{12}-\frac{1-2\nu}{8\pi(1-\nu)}I_1 \qquad \textbf{Equation 1-21}$$

$$S_{1133}=\frac{1}{8\pi(1-\nu)}a_3^2 I_{13}-\frac{1-2\nu}{8\pi(1-\nu)}I_1 \qquad \textbf{Equation 1-22}$$

$$S_{1212}=\frac{a_1^2+a_2^2}{16\pi(1-\nu)}I_{12}-\frac{1-2\nu}{16\pi(1-\nu)}\left(I_1+I_2\right) \qquad \textbf{Equation 1-23}$$

All other non-zero components can be obtained via cyclic permutation. S_{ijkl} is called Eshelby tensor.

The elliptic integrals in **Equation 1-14** to Equation **1-16** can be simplified by assuming the shape of the inclusion. In case of prolate spheroid inclusion ($a_1>a_2=a_3$), which is a typical shape of short fibers in FRPs, elliptic integrals are defined analytically as follows (**Equation 1-24** to **Equation 1-29**), and consequently Eshelby tensor S_{ijkl} can be easily obtained using **Equation 1-20** to **Equation 1-23**.

$$I_1 = 4\pi - 2I_2$$ **Equation 1-24**

$$I_2 = I_3 = \frac{2\pi a_1 a_3^2}{\left(a_1^2 - a_3^2\right)^{3/2}} \left\{ \frac{a_1}{a_3} \left(\frac{a_1^2}{a_3^2} - 1 \right)^{1/2} - \cosh^{-1}\left(\frac{a_1}{a_3} \right) \right\}$$ **Equation 1-25**

$$3I_{11} = 4\pi / a_1^2 - 2I_{12}$$ **Equation 1-26**

$$I_{12} = \left(I_2 - I_1 \right) / \left(a_1^2 - a_2^2 \right)$$ **Equation 1-27**

$$I_{23} = \pi / a_2^2 - \left(I_2 - I_1 \right) / 4\left(a_1^2 - a_2^2 \right)$$ **Equation 1-28**

$$I_{23} = I_{22} = I_{33}$$ **Equation 1-29**

1.4. Research objective

In Chapter 2, a machine learning-assisted tensile strength prediction model of unidirectional (UD) FRP considering the randomness of the microstructural fiber array is proposed. Stress concentration factor (SCF) generated by the broken fiber is a dominating feature to determine the tensile strength of UD FRP. In general, however, no analytical model has been proposed for SCF calculation in randomly distributed fibers in UD composite. The author proposes a novel machine learning-assisted modelling of SCF in UD composites. Extensive finite element simulations were performed, calculating SCF for UD composites with various random fiber arrays. Then, an artificial neural network (ANN) was trained with the obtained SCF data and used it to predict the SCF for composites with an arbitrary random fiber array. A tensile strength prediction model was developed based on a new recurrence relation for fiber fracture propagation and a determination algorithm for the fracture sequence for random fiber arrays. The tensile strength of UD composites was predicted over a range of values, demonstrating that accuracy was superior to conventional prediction methods.

In Chapter 3, a machine-learning assisted two-step homogenization framework for short fiber-reinforced plastics (SFRPs) is proposed. Consideration of orientation is very important because the anisotropy of thermomechanical properties is differently generated depending on the orientation of inclusion. A series-parallel ANN system was constructed and

trained to facilitate the time-consuming reconstruction of orientation distribution function and pseudograin decomposition procedures. Then, we implemented the series-parallel ANN system, Mori-Tanaka model, and Voigt model into ABAQUS user material subroutine (UMAT). The elastic modulus values predicted by UMAT were in a good agreement with both DIGIMAT and experimental values, The low computation time of UMAT also justified the application of machine learning approach to the two-step thermo-mechanical homogenization framework.

In Chapter 4, the previously developed two-step homogenization framework for SFRP will be expanded to describe more general case by introducing the concept of interphase with constant nano-scale thickness between matrix and inclusion. This third phase enabled us to take inclusion size effect into account. The applicability of the extended three-phase homogenization framework in material design will be confirmed by comparing the effective thermomechanical properties obtained via experimental and finite element simulation.

Chapter 2. Machine learning-assisted modelling of stress concentration factor in unidirectional fiber composites

2.1. Research background

An excellent mechanical properties of unidirectional (UD) fiber-reinforced composites are not fully utilized due to the significant variations in tensile strength [46, 47] caused by the differences in material properties [48-51] or microstructural randomness [52-55]. The safety factor of UD fiber-reinforced composites is therefore considerably higher than that of metals. Many researchers have tried to understand and model the uncertainty in UD fiber-reinforced composites [56-61], but have not yet developed predictive models of tensile strength that consider its uncertainty. An accurate model for predicting tensile strength capable of quantifying uncertainty is required to improve the applicability of fiber-reinforced composite materials.

The most widely used approach for tensile strength prediction uses a failure criterion, such as those of Tsai–Hill [62], Tsai–Wu [63], and Puck [64]. However, despite its outstanding intuitiveness, failure criteria-based tensile strength prediction is a posterior method that requires experimental data on tensile strength. Therefore, this approach cannot account for the degree of randomness involved. By contrast, the alternative constituent-level approach could be used to calculate tensile strength, taking the origin of the uncertainty into account when predicting the tensile strength.

There are currently two approaches to predicting the tensile strength of UD composites: statistical and analytical models. The former models consider UD composites as arrays of representative volume elements in which broken fibers are surrounded by a perfectly bonded cylinder of matrix [65]. Assuming that each element's strength follows the Weibull distribution, the fracture probability of an element when an external load is applied to the representative volume element array is determined. A failed element causes a local stress concentration in the nearest elements [66], resulting in multiple fractures. This approach is referred to as cumulative weakening theory; the statistical tensile strength of the UD composite is obtained by combining a failure criterion [67] with this theory. In an analytical model, the tensile strength of UD composites is calculated based on the shear lag theory, which accounts for the interfacial shear strength between each fiber and the matrix [68, 69]. This model does not consider multiple sequential fiber fractures; instead, it considers an existing broken fiber cluster. These statistical and analytical models have different perspectives on multiple fractures of fibers and interfacial shear strength, each with its own advantages and disadvantages.

Recently, Na et al. [1] proposed an integrated tensile strength prediction model that combines the statistical and analytical models. They assumed that continuous fibers within UD composites are in a hexagonal close packing (HCP) array, which leads to simplification of the recurrence relation for fiber fracture propagation and stress concentration factor (SCF) calculation. This

assumption, however, is unrealistic because various X-ray computed tomography analyses have demonstrated that the continuous fibers are randomly embedded in real UD composites [70-73].

In this chapter, we propose a series of machine learning-assisted modeling procedures that can predict the tensile strength of UD composites considering the uncertainty, i.e., the randomness of the microstructural fiber array. First, we derive the recurrence relation for fiber fracture propagation in an arbitrary random fiber array (RFA). Next, we introduce a machine learning approach to develop a model capable of predicting the SCF in an arbitrary RFA. For this, we performed extensive finite element calculations for 1,500 different RFAs to accumulate more than 20,000 pieces of SCF data. We then used these SCF data to construct an artificial neural network (ANN) model that can predict the SCF of UD composites with an arbitrary RFA. Finally, we propose a prediction model using the new recurrence relation and ANN model.

2.2. Methods

2.2.1. A new recurrence relation for fiber fracture propagation

Consider a situation in which a tensile stress σ is applied to a fiber array with a simple HCP structure, as shown in **Figure 2-1(a)**. Note that all fibers are under the isostress (σ_f) condition. Thus, without loss of generality, it can be assumed that a fracture occurs in the central fiber (fiber 1) according to the probability calculated by the Weibull distribution [74, 75] in the form of

$$F(\sigma_f) = 1 - \exp\left[-\frac{L}{L_0}\left(\frac{\sigma_f}{\gamma}\right)^{\beta}\right] \qquad \textbf{Equation 2-1}$$

where $F(\sigma_f)$ is the failure probability of a single fiber with length L under stress σ_f, L_0 is a reference length, and β and γ are Weibull distribution parameters.

Let us define p_k as the probability of k multiple fractures; then, p_1 is equal to $F(\sigma_f)$:

$$p_1 = F(\sigma_f) \qquad \textbf{Equation 2-2}$$

Next, consider a situation in which a second fracture (fiber 2) occurs after fiber 1 breaks according to p_1, as shown in **Figure 2-1(b)**. The rest of the fibers in the HCP fiber array experience greater stress to compensate for the loss of fiber 1's load-carrying capacity. The ratio of this extra stress is defined as the SCF, C_{ij}, where the subscript indicates the SCF generated in the *j*th fiber due to fracture of the *i*th fiber. Details of the SCF calculation using finite element analysis are provided in the following section. The transitional

probability (e_{ij}) is defined as [65]:

$$e_{ij}=\frac{F(C_{ij}\sigma_f)-F(\sigma_f)}{1-F(\sigma_f)} \qquad \textbf{Equation 2-3}$$

where the subscript ij indicates that e_{ij} is the probability that the fracture will propagate to the *j*th fiber due to overstress caused by the *i*th broken fiber.

According to the numerical simulation results of Na et al. [1], the SCF in the HCP fiber array tends to decrease as the distance from the broken fiber increases, and its value is the same for all fibers at the same distance. There are six geometrically identical fibers for which the highest SCF is near fiber 1; thus, they are all candidates for fiber 2 (brown fibers in **Figure 2-1(b)**). Without loss of generality, suppose fiber 2 is the fiber directly above fiber 1. Then, the probability of a second fracture p_2 can be expressed as the conditional probability that e_{12} will occur given that p_1 has already occurred:

$$p_2=p_1e_{12} \qquad \textbf{Equation 2-4}$$

This can be converted into the probability of a complementary event, as follows:

$$p_2=p_1\left[1-(1-e_{12})\right], \qquad \textbf{Equation 2-5}$$

which will help us understand the recurrence relationship later in the derivation process. Similarly, consider a situation in which a third fracture occurs (fiber 3) after fibers 1 and 2 break according to p_2, as shown in **Figure 2-1(c)**. After the second fracture, more than one broken fiber becomes

involved in fracture propagation. Hence, it is necessary to assume that the previous fiber's fracture independently affects fracture propagation to the next fiber. Under this assumption, there are two geometrically identical fibers with the highest SCF being near fibers 1 and 2; they are both candidates for fiber 3 (brown fibers in **Figure 2-1(c)**). Without loss of generality, suppose that fiber 3 is the fiber on the left of fibers 1 and 2. Let us define e_k as the overall transitional probability of the *k*th fiber (fiber *k*) due to there being *k*-1 broken fibers. Then, the probability of there being no fracture transition of fiber 3 ($\sim e_3$) due to fibers 1 and 2 can be expressed using e_{13} and e_{23}, as:

$$\sim e_3 = (1 - e_{13})(1 - e_{23}) \qquad \textbf{Equation 2-6}$$

The probability of fracture transition of fiber 3 (e_3) due to fiber 1 or 2 is

$$e_3 = 1 - (1 - e_{13})(1 - e_{23}) \qquad \textbf{Equation 2-7}$$

The probability of a third fracture p_3 can then be expressed by multiplying p_2 and **Equation (2-7)**:

$$p_3 = p_2[1 - (1 - e_{13})(1 - e_{23})] \qquad \textbf{Equation 2-8}$$

The fourth or subsequent fractures can be considered using the same logical procedure, as shown in **Figure 2-1(d)**. We can deduce that only **Equation (2-6)** and **Equation (2-7)** will change as the order of the fracture increases. For the *k*th fracture, **Equation (2-7)** can be rewritten as:

$$e_k = 1 - \prod_{i=1}^{k-1} (1 - e_{ik}) \qquad \textbf{Equation 2-9}$$

Therefore, the recurrence relation for the fiber fracture propagation in an HCP

fiber array can be generalized as:

$$p_k = p_{k-1}[1 - \prod_{i=1}^{k-1}(1 - e_{ik})] \qquad \textbf{Equation 2-10}$$

whose initial value p_1 can be obtained by **Equation (2-2)**. **Equation (2-10)** is our final form of the recurrence relation for fiber fracture propagation.

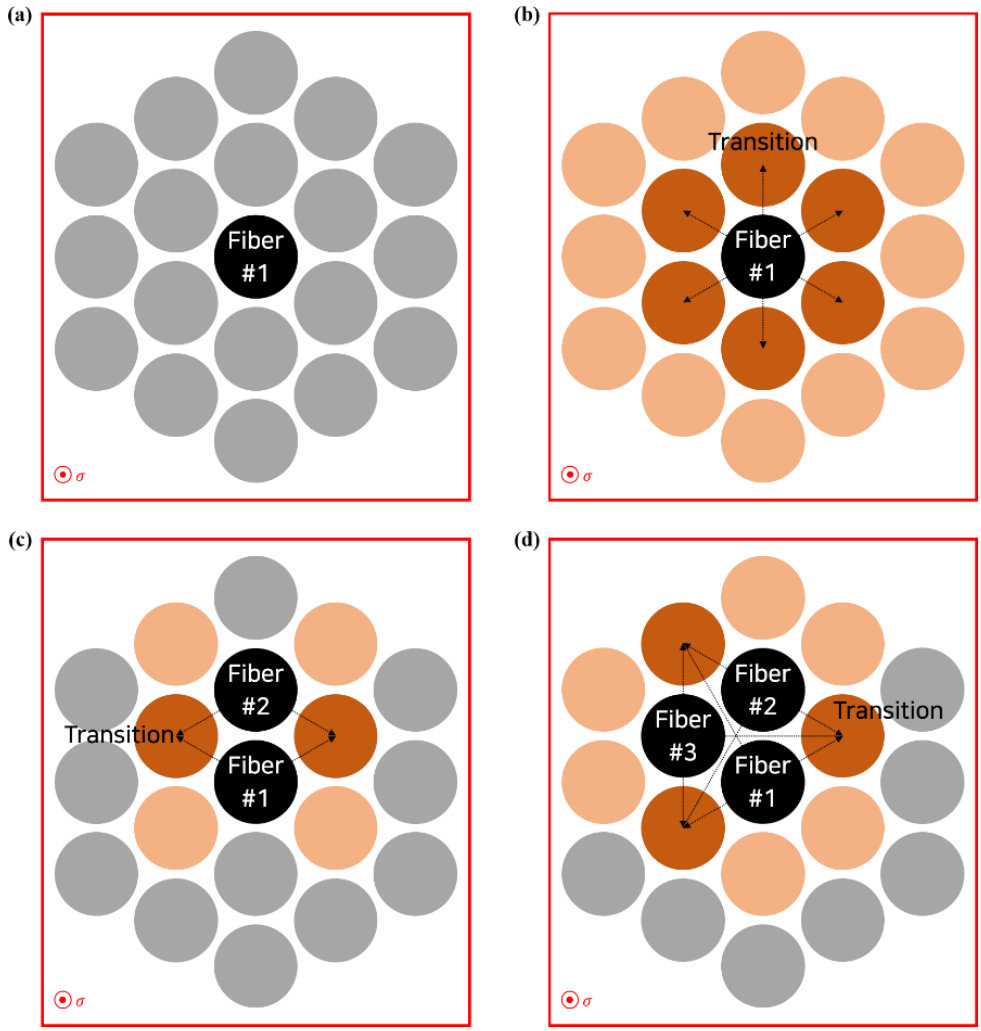

Figure 2-1 Schematic diagram of multiple fracture propagation in a hexagonal close packing fiber array under a tensile stress, σ. Black denotes a fiber that is already broken. Brown and orange denote fibers with the highest and second highest transition probabilities, respectively. (a) Initiation of first fiber fracture (fiber 1); (b) six candidates for the next fiber fracture (fiber 2); (c) two candidates for fiber 3; and (d) three candidates for fiber 4

2.2.2. Determination of the fiber fracture sequence

Fracture sequence determination in an HCP fiber array is straightforward because all the distances from a broken fiber are multiples of the nearest distance. Because all fibers are geometrically identical, the fiber fracture follows an arbitrary sequence (e.g., clockwise; **Figure 2-2(a)**) without loss of generality in the fracture sequence. In an RFA, however, the fracture sequence is somewhat ambiguous (**Figure 2-2(b)**). All pairs of fibers in an RFA have different distances separating them, resulting in different transitional probabilities. Hence, determination of the fracture sequence in an RFA should be performed based on a quantitative comparison of the transitional probabilities. Once the methodology for determining the fracture sequence of an arbitrary RFA is established, the recurrence relation (**Equation 2-10**) can be applied directly without modification.

An algorithm for determining the fracture sequence is shown in **Figure 2-3**. Our algorithm requires the number of fibers (N) in a target RFA and the coordinate matrix (x, y) of all fibers. Assume that fiber 1 is at the center of the unit cell, and its coordinates are (x_1, y_1). The initial value of k is set to 2 once the input data above are inputted into the algorithm, which means that the algorithm will sequentially seek the fiber with the highest transitional probability for the second fracture. The initial values of i and j are 1 and k, respectively. For given i and j values, the algorithm will calculate the distance (d_{ij}) between (x_i, y_i) and (x_j, y_j), SCF (C_{ij}), and the

transitional probability (e_{ij}). This calculation process is repeated until the values of i and j reach $k-1$ and N, respectively. Because all possible e_{ij} values are obtained, the overall transitional probability of the jth fiber (e_j) can easily be calculated using **Equation 2-9**. The algorithm then determines which fiber has the maximum e_j value and swaps the (x_k, y_k) and (x_j, y_j) coordinates in the original (x, y) matrix, which sorts the matrix according to the fracture sequence. These iterations are then repeated until the value of k reaches N.

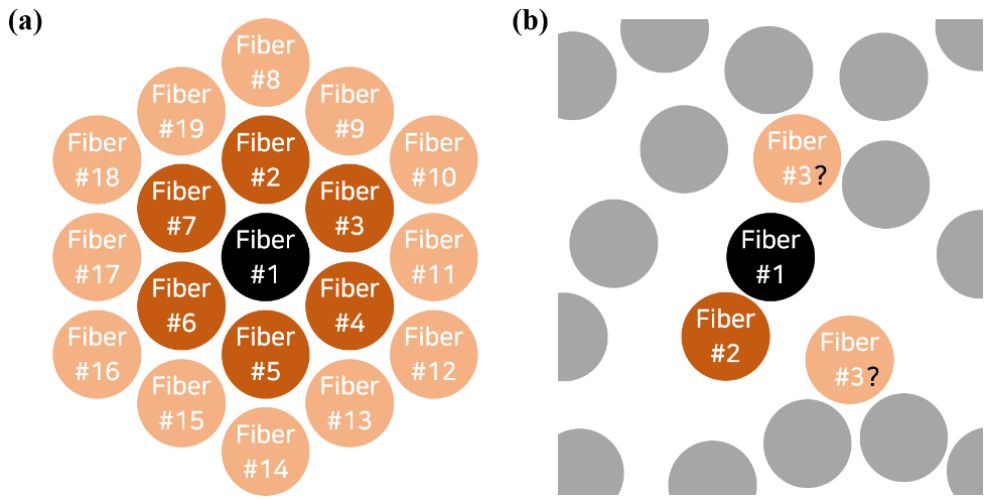

Figure 2-2 Comparison of the fracture sequence between (a) a hexagonal close packing (HCP) fiber array and (b) random fiber array (RFA)

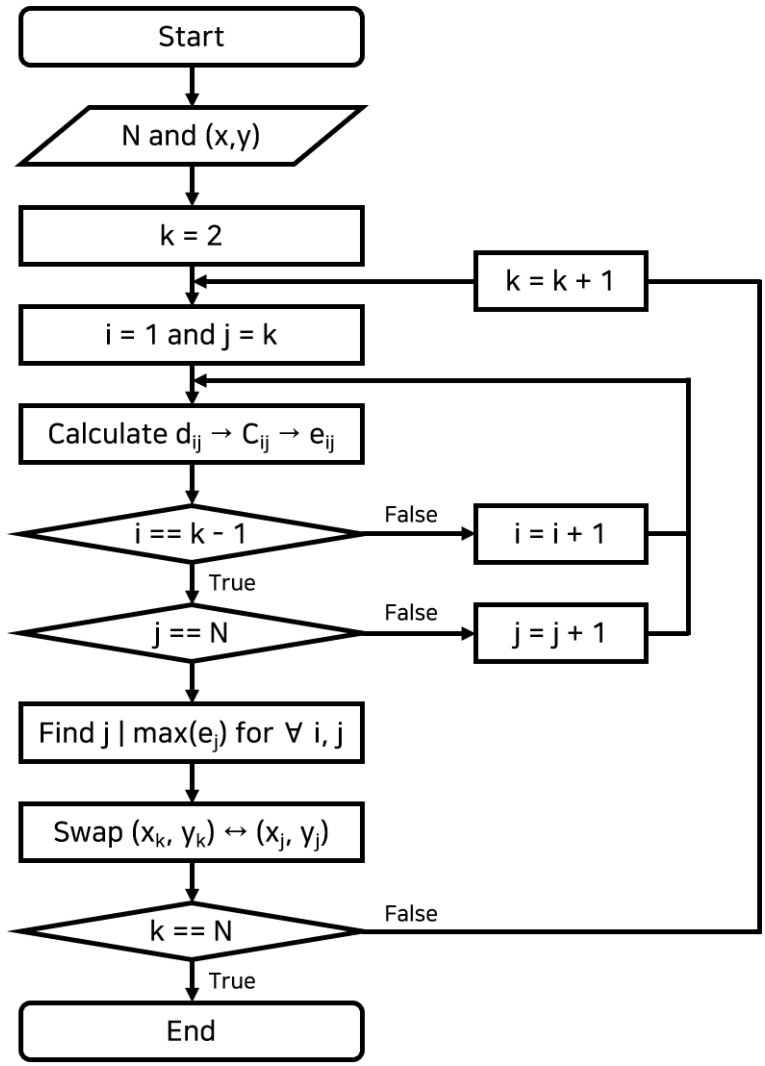

Figure 2-3 Flowchart to determine the fiber fracture sequence in a random fiber array

2.2.3. Machine learning-assisted tensile strength prediction

The analytical composite strength ($\sigma_{c,analytical}$) can be calculated by [1, 69],

$$\sigma_{c,analytical}=\min\left[\left(\frac{L_0}{2(\ln 10)\,e\beta\lambda k}\right)^{\frac{1}{\beta}}\gamma,\left(\frac{2L_0\tau_b}{e(\beta+1)R_f k}\right)^{\frac{1}{\beta+1}}\gamma^{\frac{\beta}{\beta+1}}\right]V_f \qquad \textbf{Equation 2-11}$$

where V_f is the fiber volume fraction, R_f is the fiber radius, β and γ are the Weibull distribution parameters, λ is the ineffective length, and τ_b is the interfacial shear stress. The statistical composite strength ($\sigma_{c,statistical}$) corresponds to an applied stress whose expectation value of multiple fractures exceeds unity:

$$FIND(\sigma_{c,statistical}|\int_{\sigma=0}^{\sigma_{c,statistical}} p_k(\sigma)\,d\sigma=1) \qquad \textbf{Equation 2-12}$$

According to Na et al. [1], the tensile strength of the UD composite is determined as the intersection of the analytical and statistical composite strength plots, and the corresponding multiple fracture number is called the critical multiple fracture number.

To use the composite strength prediction methodology above, we need a model that can calculate the SCF (C_{ij}) of a fiber in an arbitrary environment. However, no analytical equation has been proposed for the calculation of SCF in general, so this can only be obtained through finite element simulation. Machine learning-assisted modeling can be a useful method because it can obtain a good solution to problems where no analytical equation has been established. As can be seen in recent studies using tens to millions of data points for training machine learning models in the field of composite

materials [7, 30-39], the quantity of data provided would determine the quality of a machine learning-assisted SCF model. Hence, it is essential to establish a fully automated procedure capable of obtaining a massive amount of SCF data.

2.2.4. Calculation of stress concentration factors

Our fully automated procedure for calculating the SCF consists of two steps: generation of RFAs using MATLAB R2022a software and finite element simulation using ABAQUS/CAE 2018 software. Various RFA generation algorithms have been proposed, including random sequential adsorption, nearest neighbor, modified nearest neighbor, random sequential expansion, and random fiber removal [76-81]. In the present study, we implemented a random sequential adsorption algorithm into MATLAB, generating 1,500 RFAs with volume fractions (V_f) of 25−60%. From among these, 15 typical examples are presented in **Figure 2-4(a)**, with the volume fraction histogram of all arrays presented in **Figure 2-4(b)**. Note that the size of an RFA is $4\sqrt{2}d_f$, where d_f is the diameter of a fiber. This is because, according to Barzegar et al.'s calculation of the SCF in an RFA [82], the SCF converges to 0 if the distance between the centers of the fibers is greater than 4. The number of fibers N and fiber coordinate data (x, y) of each RFA were saved and utilized later for determination of the fiber fracture sequence in **Section 2.2.2**.

A simulation model for an RFA was generated by transferring geometrical information (e.g., fiber coordinates and diameter) to ABAQUS/CAE. A typical example of a simulation model is shown in **Figure 2-5**. Note that the diameter of a fiber (d_f) is 7.0 μm and the depth (z) of the simulation model in the z-direction was sufficiently long ($30d_f$) to ensure a stress recovery of over 99% (see **Figure 2-6**). A broken plane was

introduced into the center of the simulation model (**Figure 2-5(a)**). A broken fiber was defined based on the geometry of the central fiber in the broken plane. A cohesive layer with a thickness of 5% of d_f was introduced into the broken fiber at the center, as shown in **Figure 2-5(b)**. The other fibers' cohesive layers were not considered because the interfacial influence was not significant, and their consideration increased computational cost.

The material properties listed in **Table 2-1** were assigned to the fiber, matrix, and cohesive layers. Perfect bonding was assumed for all interfaces, including fiber-to-matrix, fiber-to-cohesive layer, and matrix-to-cohesive layer bonding. The fibers and matrix were meshed as six-noded linear triangular prisms (C3D6) with mesh size of $\pi \cdot d_f / 15$ better describe the cylindrical geometries. The cohesive layer was meshed as eight-noded three-dimensional cohesive elements (COH3D8). Note that a finer mesh with size of $d_f / 25$ was generated around the broken plane and cohesive layer to better simulate the stress concentration phenomenon, as shown in **Figure 2-5(c)** and **Figure 2-5(d)**. A schematic diagram of the boundary conditions applied to the simulation model is shown in **Figure 2-5(e)**. Displacement ($U3 = 0.1\%$ strain) and pinned ($U3 = 0$) boundary conditions were applied to both planes perpendicular to the z-axis. x- ($U1 = UR2 = UR3 = 0$) and y-symmetry ($U2 = UR1 = UR3 = 0$) boundary conditions were applied to the planes perpendicular to the x- and y-axes, respectively. Note that periodic boundary conditions were not applied because these increased the calculation time but

did not change the calculation result significantly. The ABAQUS/CAE modeling procedures described above were implemented using Python and repeated for all 1,500 RFAs.

Table 2-1 Material properties of unidirectional carbon fiber–polyamide composites for stress concentration factor simulation [1]

Material property	Value
Fiber longitudinal tensile modulus (E_{fl})	217.0 GPa
Fiber transverse tensile modulus (E_{ft})	21.7 GPa
Fiber Poisson's ratio (ν_f)	0.2
Matrix tensile modulus (E_m)	3.0 GPa
Matrix Poisson's ratio (ν_m)	0.3
Normal interfacial shear stress ($\tau_{IFSS,\perp}$)	100.0 GPa
Tangential interfacial shear stress ($\tau_{IFSS,\parallel}$)	20.0 GPa
Interface fracture energy (G_{IC})	270.0 J/m^2

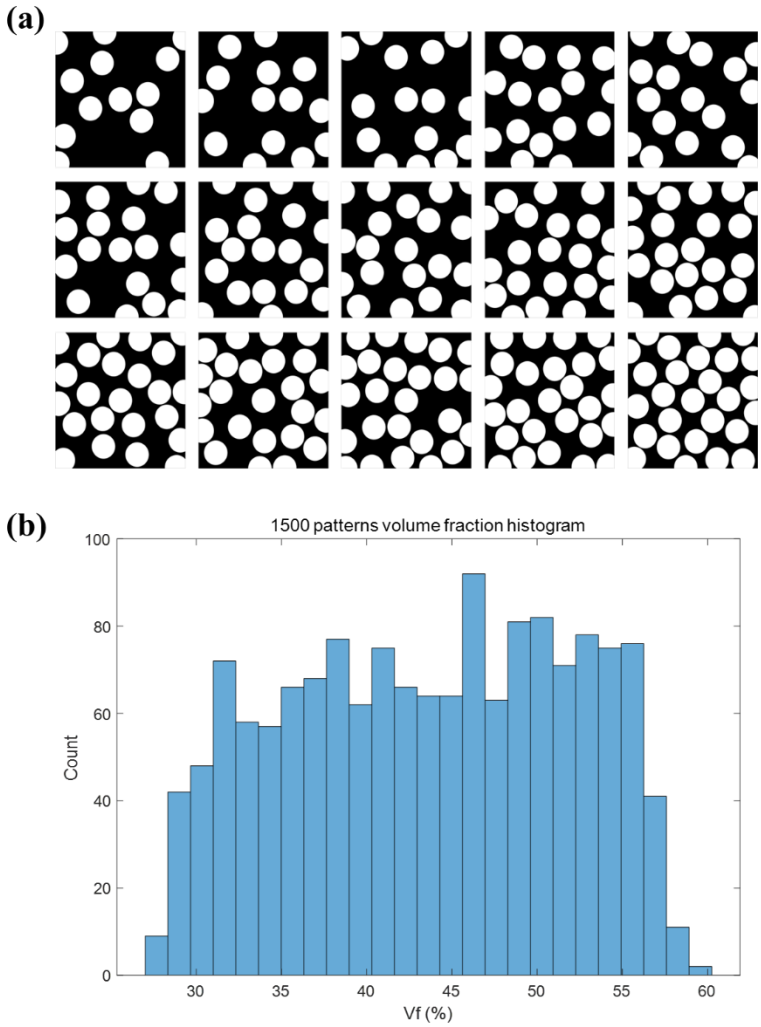

Figure 2-4 (a) Typical examples and (b) volume fraction histogram of 1,500 random fiber arrays generated in MATLAB

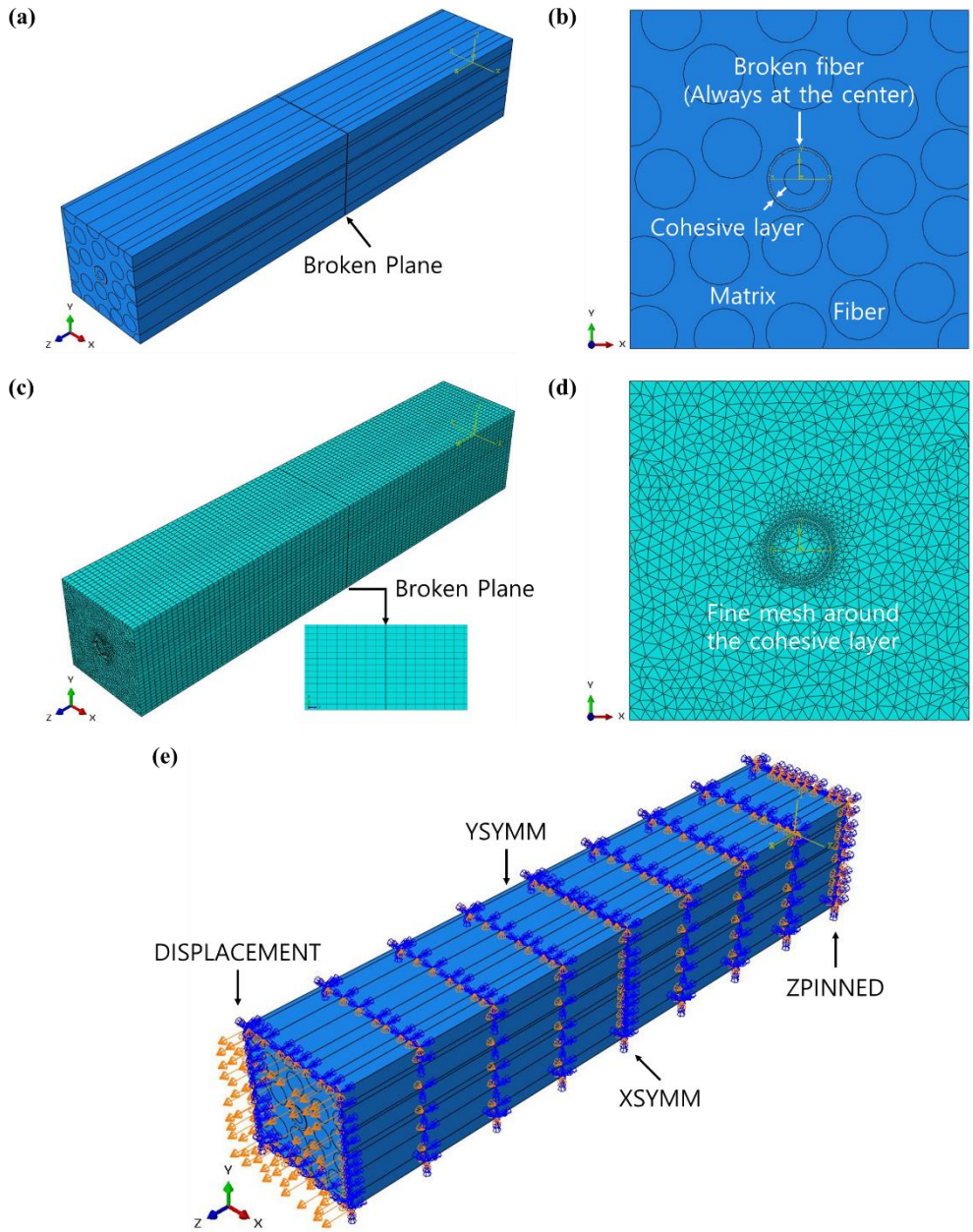

Figure 2-5 Typical example of (a, b) simulation model, (c, d) simulation mesh, and (e) boundary conditions of a random fiber array used for calculating the SCF

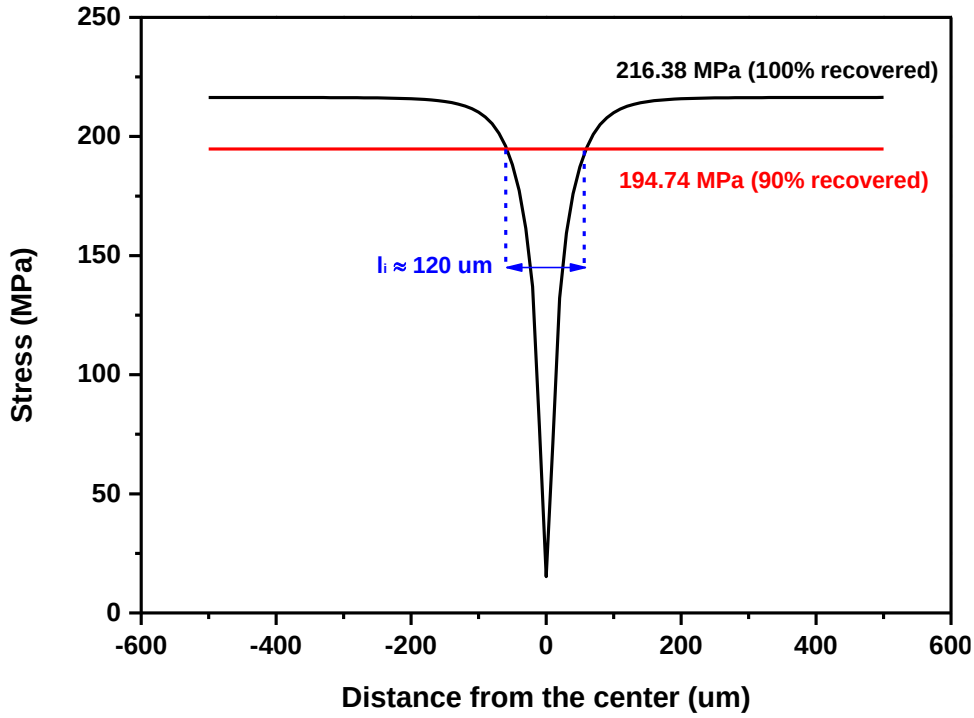

Figure 2-6 Determination of ineffective length for given simulation condition

2.3. Results and Discussion

2.3.1. Data accumulation for the stress concentration factor

A typical result of the simulation procedure in **Section 2.2.4.** is shown in **Figure 2-7**. To observe the stress concentration behavior of the surrounding fibers due to the broken fiber at the center, we cut each simulation model with a broken plane, as shown in **Figure 2-7(b)**. The SCF of a fiber whose normalized center distance from the broken fiber is D/d_f in a fiber array consisting of V_f, E_{fl}, and E_m can be expressed as:

$$C(D/d_f, V_f, E_{fl}, E_m) = \frac{\sum RF(D/d_f, V_f, E_{fl}, E_m)_{z=L/2}}{\sum RF(D/d_f, V_f, E_{fl}, E_m)_{z=L}} \qquad \textbf{Equation 2-13}$$

where D is the distance from the broken fiber and $\sum RF$ is the sum of the reaction forces across the fiber cross-section, and the subscript $z=z_0$ corresponds to the cross-section location. Note that $z=L/2$ corresponds to the broken plane's depth and $z=L$ corresponds to the plane where the stress concentration is fully recovered. An RFA contains 13−27 fibers depending on the fiber volume fraction. The total number of fibers across the 1,500 RFAs was 28,500. Hence, the number of $C(D/d_f, V_f, E_{fl}, E_m)$ data points accumulated through the simulation was 28,500.

Figure 2-8(a) shows a three-dimensional scatter plot of the SCF data. A two-dimensional scatter plot is presented in **Figure 2-8(b)** to better show the volume fraction dependency of the SCF. There is a difference in SCF for low and high-volume fraction composites. If there are stochastically many

undamaged fibers around the broken fibers, i.e., high volume fraction case, the stress concentration caused by the broken fibers will be dispersed easily, resulting in relatively low SCF. Otherwise, the stress concentration caused by the broken fibers will be concentrated, resulting in relatively high SCF. This trend can be observed in **Figure 2-8(b)**. Like the numerical calculation result of Barzegar et al. [82]; note that the SCF tends to decrease as D/d_f or V_f increases.

The scatter plots In **Figure 2-8** indicate that, due to the microstructural randomness of RFAs, the SCF of a fiber at a specific normalized center distance from a broken fiber under a particular volume fraction is not unique. Using such highly variable data to train a machine learning regression model will inevitably yield unsatisfactory results, because such methods provide only one possible solution under each set of given conditions. In the present paper, we used a statistical approach to manipulate the SCF data. First, a two-dimensional mesh grid was generated on the $D/d_f - V_f$ plane. Then, we calculated the average value ($\overline{C}(D/d, V_f, E_{fl}, E_m)$) and 99% confidence interval (*CI*) of all the SCF data contained in the grid, as follows:

$$\overline{C}(D/d_f, V_f, E_{fl}, E_m) = \frac{\sum C(D/d_f, V_f, E_{fl}, E_m)}{n} \qquad \textbf{Equation 2-14}$$

$$CI(99\%) = \overline{C}(D/d_f, V_f, E_{fl}, E_m) \pm t_{(0.5\%, n-1)} \frac{S}{\sqrt{n}} \qquad \textbf{Equation 2-15}$$

where n and S are the number and variance of the datapoints in the grid, respectively. Note that the t-distribution was used to calculate the CI.

The concept underlying this procedure is summarized in **Figure 2-9**. We performed the procedure repeatedly for all grids in the $D/d_f - V_f$ plane. All stress concentration data within the grid were replaced with the corresponding average and CI data. All 28,500 manipulated data points are presented in **Figure 2-10**.

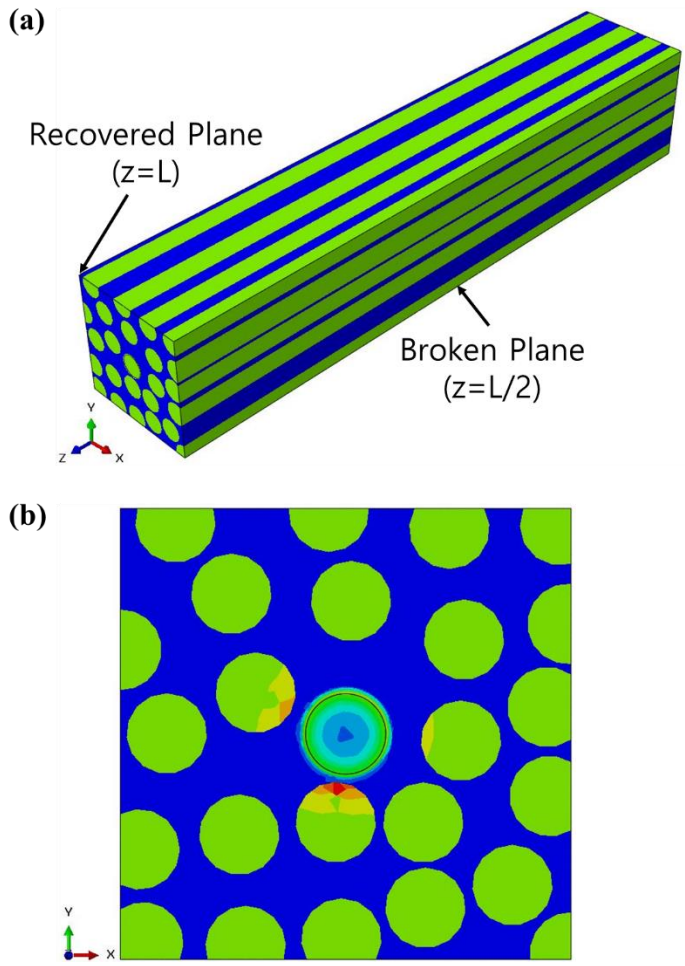

Figure 2-7 Typical example of simulation results in (a) three- and (b) two-dimensional views on the broken plane

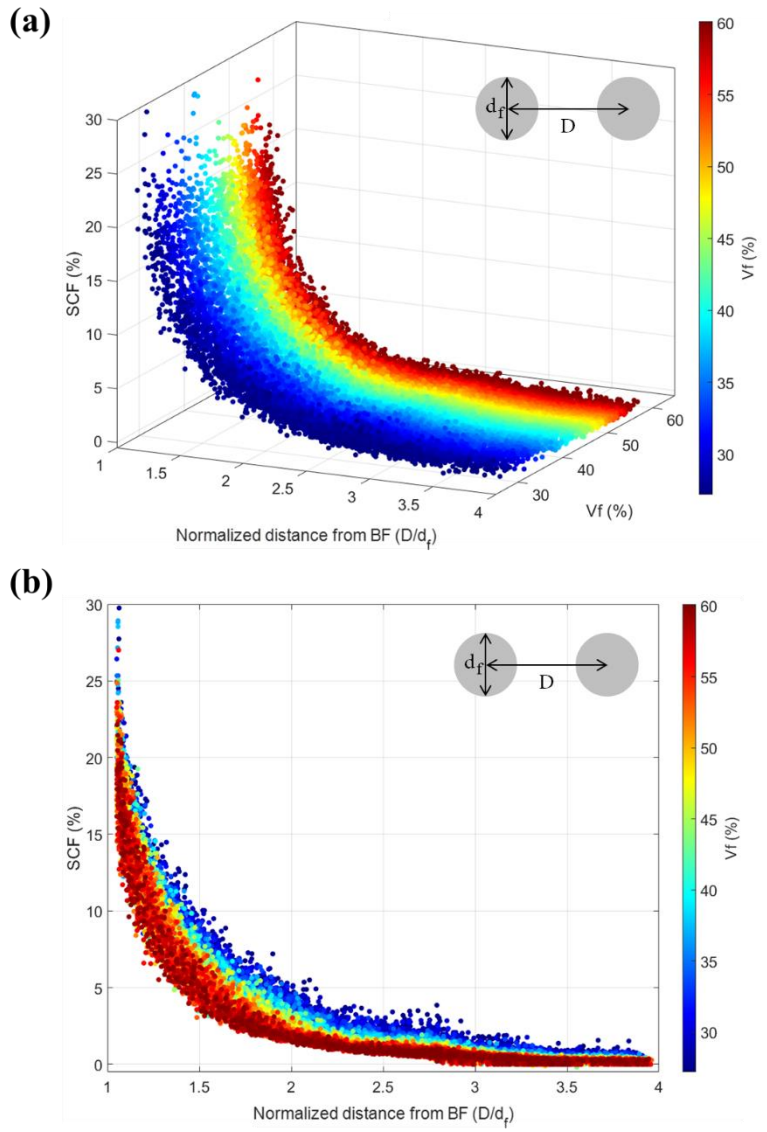

Figure 2-8 Scatter plot of stress concentration factor versus normalized center distance from the broken fiber in (a) three- and (b) two-dimensional views

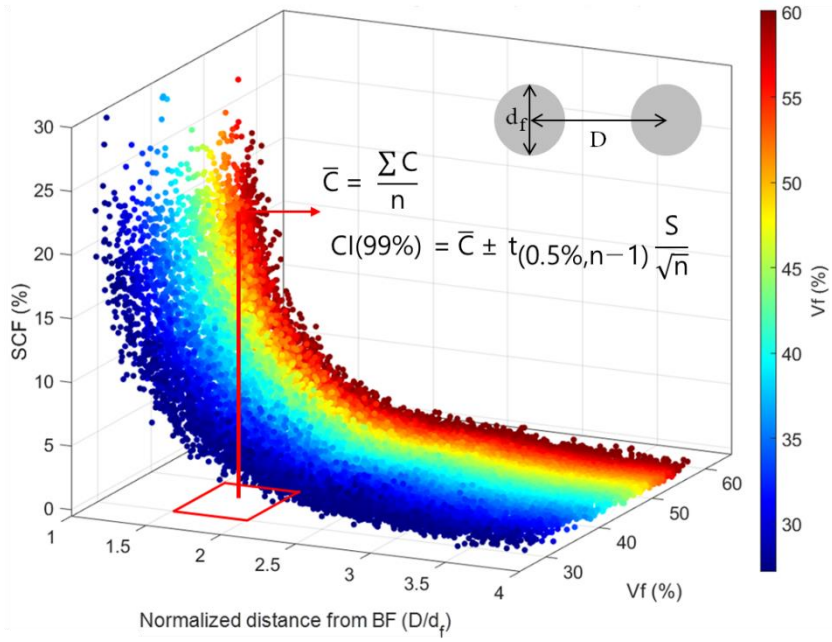

Figure 2-9 Schematic diagram of the statistical process for manipulating the stress concentration factor data

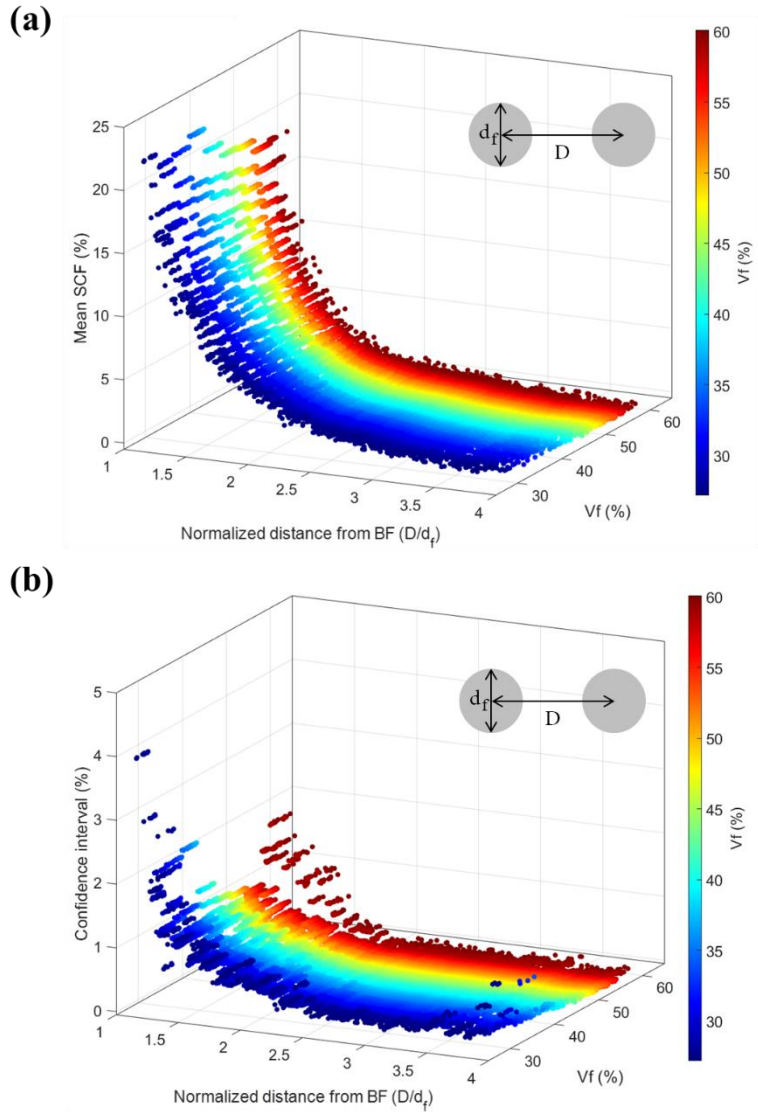

Figure 2-10 Scatter plots of the (a) average and (b) confidence interval for 28,500 manipulated stress concentration factor data points

2.3.2. Training an ANN with stress concentration factor data

An ANN is a computing system inspired by biological neural networks [83]. There have been many attempts to apply ANNs in the field of composites research [84-92]. Herein, we trained an ANN with the manipulated SCF data using MATLAB Deep Learning Toolbox.

The optimal ANN architecture was determined. For the input and output layers, two input variables (D/d_f, V_f) and two output variables ($\overline{C}$ and CI) were considered. When inappropriate numbers of hidden layers and neurons are used, low training accuracy or overfitting may occur. Vujicic et al. [93] compared methods proposed for determining the number of hidden neurons, and concluded that the best way to determine the optimal topology of a neural network to address a specific problem is to train and test the network using different numbers of hidden layers and neurons, where different methods provide different results depending on the dataset.

To determine the most appropriate hidden layer architecture to address our problem, preliminary training was performed by varying the numbers of hidden layers and neurons in each layer between 1 and 10. A Bayesian regularization backpropagation algorithm (trainbr) was used for model training. Mean squared error (mse) was the performance metric. The hyperbolic tangent sigmoid (tansig) transfer function was applied to the input and hidden layers, while a linear transfer function (purelin) was applied to the output layer. The input data (28,500) were randomly divided into training,

testing, and validation datasets (proportions of 70%, 15%, and 15%, respectively). To prevent overfitting, the training epoch was stopped if the error increased more than six times during the validation procedure (max_fail). The preliminary training results, i.e., the training time and validation performance as functions of the number of hidden layers and neurons, are presented in **Figure 2-11(a)** and **Figure 2-11(b)**, respectively. Note that the logarithm of the mse shown in **Figure 2-11(b)** was calculated to show the trends more clearly. The tensile strength prediction results calculated using the method described later in **Section 2.3.3** are presented in **Figure 2-11(c)**. It was confirmed that the tensile strength prediction results converged when the combination of hidden layer and hidden neuron was between 3/3 and 7/7. The tensile strength predictions were out of trend in extreme cases (e.g., 1/1, 10/1, and 10/10), because of the underfitting or overfitting problem due to improper hidden layer architectures [94].

Among the converged combinations, both training time and validation performance were excellent when there were six hidden layers and six neurons. Therefore, the optimal ANN configuration was determined to be six hidden neurons in each of six hidden layers, as shown in **Figure 2-12**.

The 28,500 input and output datasets were trained with the optimized ANN configuration. The max_fail value was set to 20, while the rest of the conditions the same those for the preliminary training. The training results are presented as a regression plot, “training state” plot, performance plot, and error histogram in **Figure 2-13**. The best performance was achieved at the

382nd epoch (R = 0.99924). This result confirmed that an ANN model is capable of providing statistical information about the average value ($\overline{C}$) and uncertainty (CI) of the SCF for a UD composite material with arbitrary fiber volume fraction (V_f) and distance from the broken fiber (D/d_f).

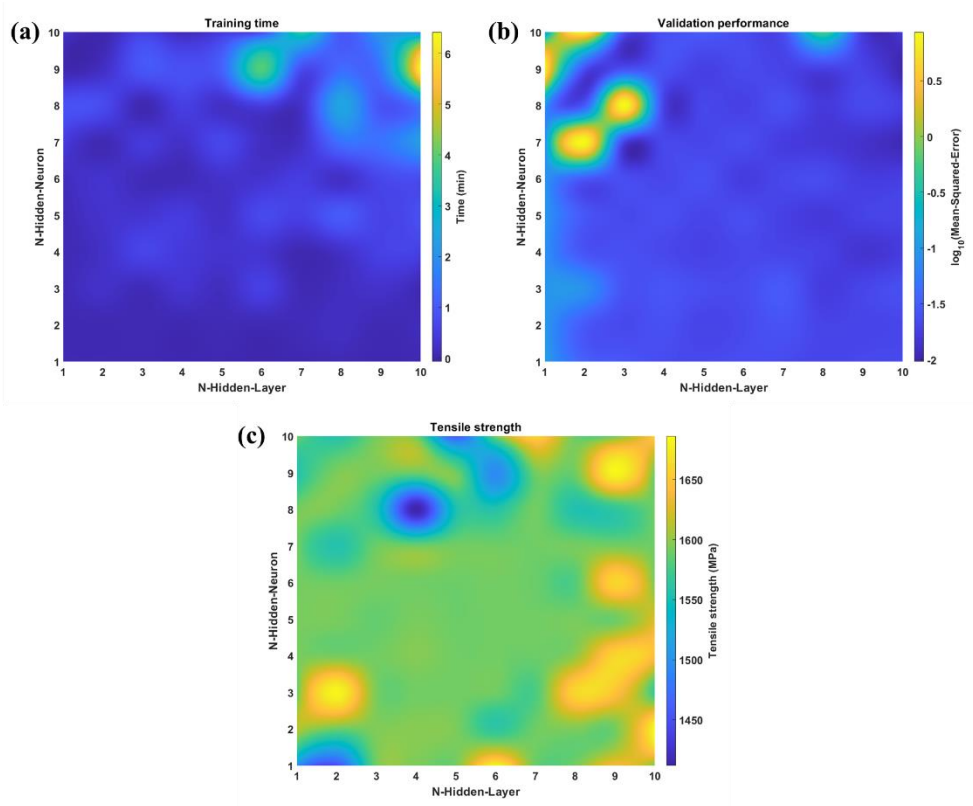

Figure 2-11 The effect of the number of hidden layer and neurons on (a) training time, (b) validation performance, and (c) tensile strength prediction result

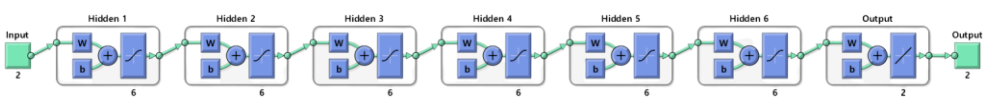

Figure 2-12 Optimized artificial neural network configuration with six hidden neurons in each of six hidden layers

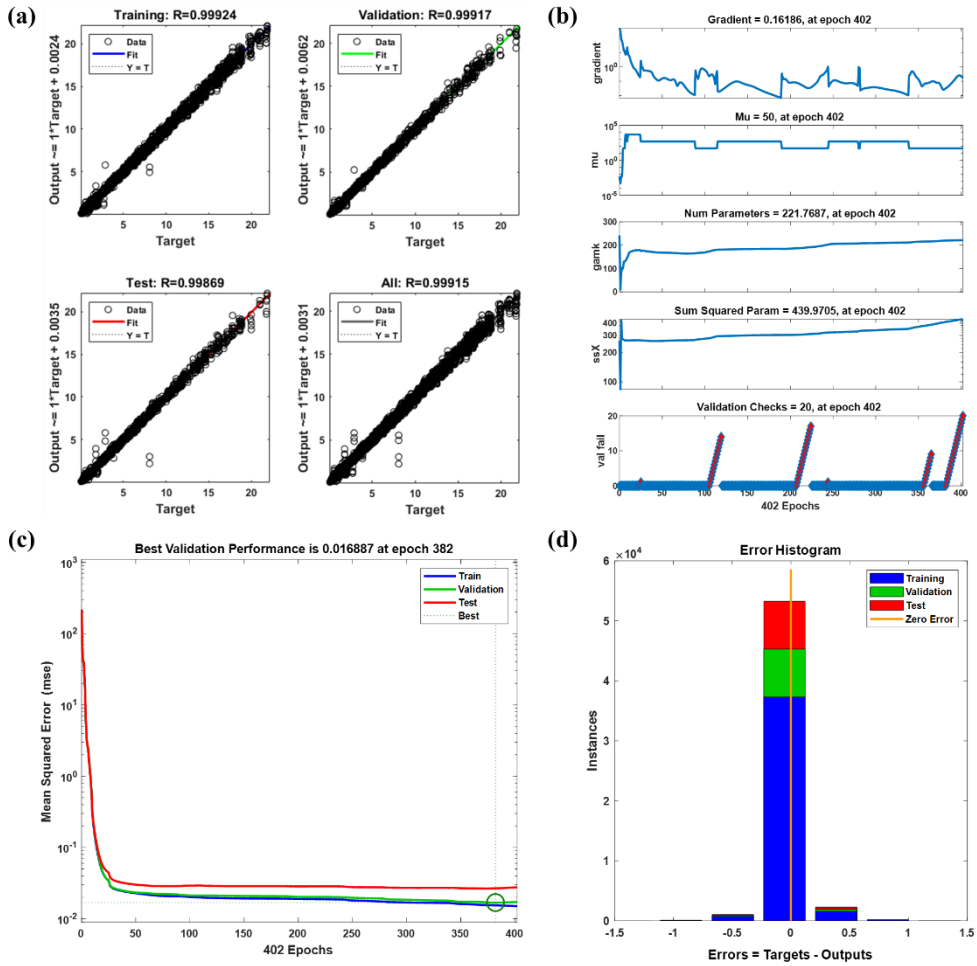

Figure 2-13 Training results for the 28,500 SCF and *CI* datasets obtained using the optimized ANN configuration. (a) Regression plot, (b) training state plot, (c) performance plot, and (d) error histogram

2.3.3. Tensile strength prediction and validation

We sequentially calculated d_{ij}, C_{ij}, and e_{ij} using the neural network model described above. To validate the model, 30 RFAs with a volume fraction of 51% were generated and used for strength prediction; we later compared these predictions with experimental data. Details of the experimental procedure can be found in a previous study [1]. First, the analytical composite strengths ($\sigma_{c,analytical}$) of 30 RFAs were obtained using **Equation 2-14**, as described in **Section 2.3.1**. Next, their statistical composite strengths ($\sigma_{c,statistical}$) were calculated using the recurrence relation (**Equation 2-10** in **Section 2.2.1.**), fiber fracture sequence determination algorithm (**Section 2.2.2.**), and ANN model (**Section 2.3.2.**). **Figure 2-14(a)** shows a typical example plot of $\sigma_{c,analytical}$ and $\sigma_{c,statistical}$. We also predicted these strengths for an HCP fiber array, as presented in **Figure 2-14(b)**. The $\sigma_{c,statistical}$ plot in **Figure 2-14(b)** is smoother than that in **Figure 2-14(a)** because the inter-fiber distance is constant in the HCP array.

Finally, the tensile strength of each of the 30 RFAs was obtained by finding the intersections of their analytical and statistical composite strength plots, as discussed in **Section 2.2.3**. The details of the parameters are provided in **Table 2-2**, and the results are shown in **Figure 2-15**. The composite strength obtained by assuming an HCP fiber array is also presented for comparison. Note that, in the figure, the scatter and error bars originate from the array's intrinsic randomness and the SCF's CI. Across the 30 RFAs, the

difference between the maximum and minimum values of the calculated composite strength is 27.51 MPa.

We then considered the microstructural features of the generated RFAs to identify essential factors for determining tensile strength. Because the HCP structure is ideal for dispersing stress concentration, the composite strength is highest for composites with HCP arrays. Indeed, **Figure 2-15** shows that the calculated composite strength assuming an HCP fiber array lies at the upper limit of the experimental data. Therefore, it can easily be deduced that the strength of a composite will be determined by the similarity of its fiber arrangement to HCP, i.e., the maximum and minimum values will be for the most and least similar to HCP, respectively. We investigated this considering the inter-fiber distance, as follows.

Figure 2-16 shows the probability density function of the smallest inter-fiber distance in the array, serving as a quantitative measure of that array's similarity to HCP. Because the smallest inter-fiber distances are all the same in an HCP fiber array, its probability density function appears as a very sharp peak at 1.0. Therefore, the probability density functions of the RFAs showing the highest strengths exhibit more positive kurtosis than those with the lowest tensile strengths. Note that, in **Figure 2-16**, the smallest inter-fiber distances obtained from all 30 RFAs were used for the calculation.

The cross-section of a real UD composite is a combination of various structures; in particular, the extreme cases of HCP and fibers with large separation can coexist. When external stress is applied to a composite with

this structure, the initiation of a single fiber fracture occurs probabilistically according to the Weibull distribution in both phases. The stress concentration will be well dispersed in the HCP-like phase, and the critical multiple fracture number will not be reached easily. By contrast, the concentration will not be well dispersed in the other phase, and this number will be reached at a lower stress. In this case, the fibers fail simultaneously after the statistical composite stress exceeds the analytical composite strength. The composite failure behavior is governed by the macroscopic damage propagation. Thus, the lowest strength value (i.e., the weakest part) determines the composite strength. **Figure 2-15** shows that the lowest strength of the simulated RFAs predicts the experimental tensile strength values with better accuracy than the HCP array. In conclusion, the macroscopic composite strength is determined by the critical multiple fractures initiated in a phase that is least similar to HCP. The tensile strength ranges from 1,552.2 to 1,579.7 MPa depending on the fiber arrangement; in particular, its microstructural similarity to HCP. This demonstrates that the model developed in this paper predicts tensile strength suitably, while also quantifying uncertainty.

In this study, the range of the fiber volume fraction with range of 25 ~ 60 % was chosen due to the following two reasons. First, this range was chosen to ensure the stress concentration between the fibers. In the case of UD composite with a low volume fraction, the probability that the breakage of one fiber affects the other fiber will decrease because the distance between fibers is stochastically longer. Second, the continuous fibers in UD

composites are closely packed due to the pressure applied during the manufacturing processes such as resin transfer or autoclave molding. As a result, UD composites exhibit high volume fraction (> 20 %). Due to the nature of artificial neural network (artificial neural network will show good performance within the training range), the performance of the current model for UD composite with fiber volume fraction less than 20%, outside our training range (25 ~ 60 %), cannot be guaranteed. UD composites with lesser fiber volume fraction (< 20 %) will be considered and reported in a near future.

Table 2-2 Definitions and values of parameters in **Equation 2-11** [1]

Parameter	Value
Fiber volume fraction (V_f)	51.0 %
Fiber radius (R_f)	3.5 μm
Weibull distribution parameter (β)	12.01
Weibull distribution parameter (γ)	3.93 GPa
Ineffective length (λ)	18.8 μm
Reference length (L_0)	10.0 mm
Interfacial shear stress (τ_b)	37.0 MPa

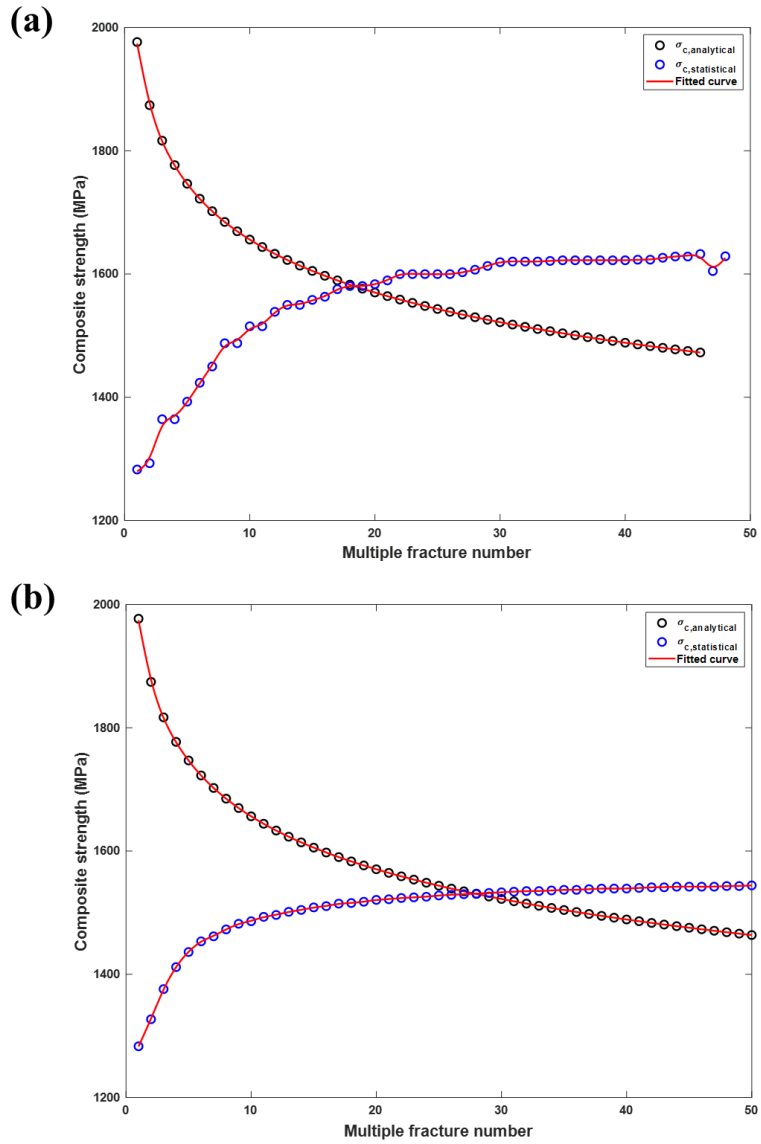

Figure 2-14 Typical example of an analytical and statistical composite strength plot for (a) a random fiber array (RFA) and (b) a hexagonal close packing (HCP) fiber array, according to the fracture number

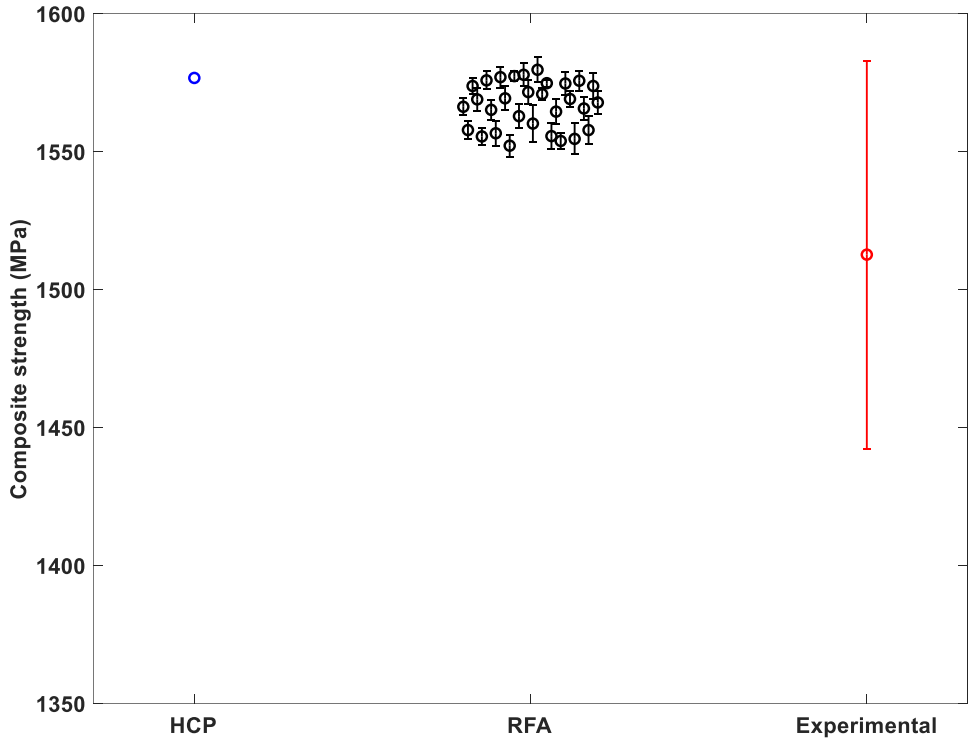

Figure 2-15 Comparison of composite strength prediction results for hexagonal close packing (HCP) arrays and random fiber arrays (RFAs), and experimental values

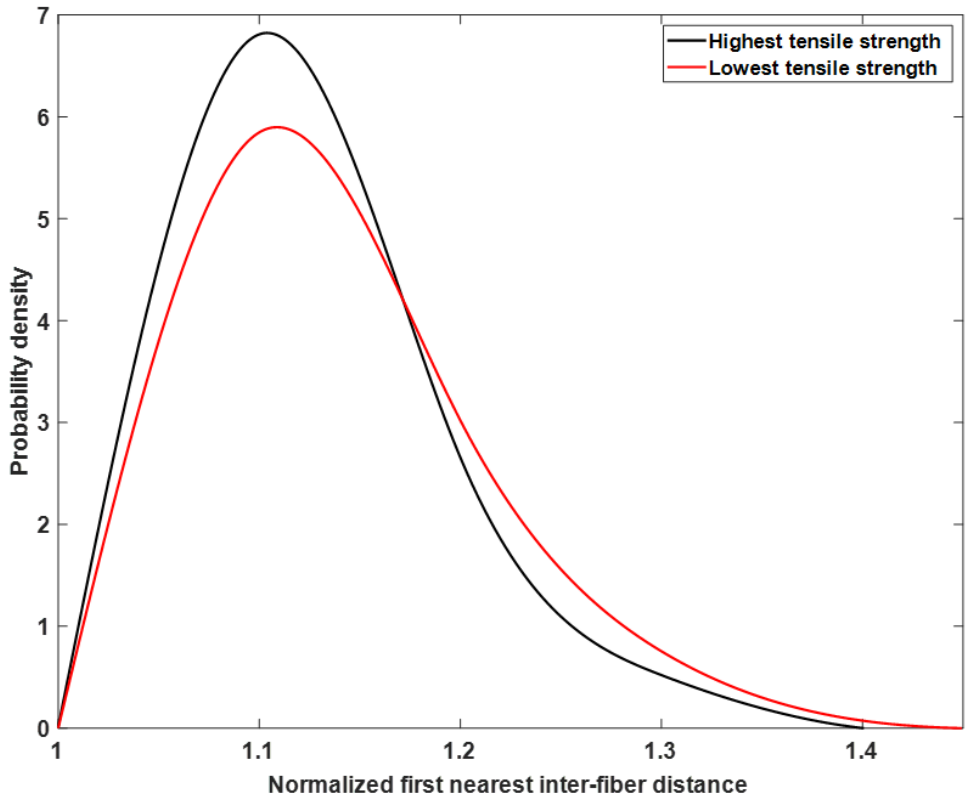

Figure 2-16 Probability density function of the smallest inter-fiber distance, plotted for the random fiber arrays with the highest and lowest tensile strengths

2.4. Summary

Stress concentration factor (SCF) is the dominant factor to determine the tensile strength of UD fiber-reinforced composites because it can effectively model a progressive contribution of broken fibers to the tensile strength. Nevertheless, an analytical model for calculating the SCF of randomly distributed fibers in UD composites has not been proposed. A machine learning approach was proposed to predict SCF by constructing and training an ANN with extensive finite element analysis results. Then, SCFs could be obtained whenever needed without actual finite element calculation, enabling to develop a novel method for predicting the tensile strength of UD fiber-reinforced composites. A new algorithm for determining the fiber fracture sequence was also developed and combined with the ANN, confirming the applicability of machine learning-assisted modelling strategy of SCF. Overall, the predicted tensile strength showed a good agreement with experiments, however its variability was predicted about 30 MPa, which was four times lower than the variation observed in the experimental tensile strength. For more realistic uncertainty modeling of the tensile strength, other parameters, e.g., microstructural randomness such as the variation in fiber diameter or misalignment in the longitudinal direction should be considered in the ANN.

Chapter 3. Machine learning-assisted pseudograin decomposition procedure in short fiber composites

3.1. Research background

The demand for short fiber-reinforced plastics (SFRPs) in the automotive and the aerospace industries is increasing owing to their design freedom, cost effectiveness, and superior specific mechanical properties [95-98]. Automotive parts made of SFRPs are generally subjected to complex loading, thus necessitating a capability of predicting or simulating such complex behavior of the parts. Therefore, a fundamental approach that can simulate the mechanical response of SFRPs is required.

The most versatile method for simulating the mechanical responses of such SFRPs involves performing direct finite element simulation to obtain the effective properties of the representative volume element (RVE) containing all geometric information, including polymer matrix and short fibers with a specific orientation [99-101]. However, this direct simulation method is extremely time consuming even with modern computing power [101]. Instead, mean-field homogenization methods based on Eshelby's single inclusion theory [40], such as the Mori–Tanaka model [41], self-consistent model [102], double-inclusion model [103], and differential-scheme model [104], are widely used. However, these homogenization models are unsuitable for interpreting SFRPs as they lead to physically unacceptable results because these models require the target composite to have inclusions of similar shape

and orientation [105].

To overcome these limitations, a two-step homogenization procedure based on pseudograin approach was first proposed by Pierard et al. [105] and has been studied by numerous studies [106-113]. The first step of the two-step homogenization procedure is the decomposition of SFRP RVE into a set of pseudograins, followed by mean-field homogenization of each pseudograin based on the Mori–Tanaka model or Double-Inclusion model. The second step of the two-step homogenization procedure is performing homogenization of all pseudograins based on uniform strain assumption (Voigt model [44]), uniform stress assumption (Reuss model [114]), or a combination of both (Voigt–Reuss model [111]). The matrix phase is assumed to be viscoelastic [115-119] or viscoelastic–viscoplastic [110, 120-123]. The short fibers within each pseudograin are assumed to be elastic and unidirectionally aligned in a representative orientation, which is determined by processing orientation distribution function (ODF) with equivalent orientation approach [124] or iso-size facets algorithm [125].

Local microstructures of SFRP vary depending on the geometry or the flow conditions of the manufacturing process (i.e., injection molding) [126-128]. Hence, ODF information must be acquired at all positions within the injection-molded SFRPs to effectively perform the two-step homogenization. Injection molding simulations can obtain local microstructures; however, they provide only orientation tensor information by solving the Folgar–Tucker equation owing to the numerical cost issue. Therefore, reconstructing ODF

from orientation tensor is essential, and the two widely used reconstruction methods are maximum entropy (ME) [129] and spherical harmonics (SH) methods [130]. ME method is known to be suitable for reconstructing ODF of injection molded SFRPs [131, 132], of which local microstructures have fiber orientations that maximize the entropy [133]. However, this method includes an iterative minimization problem to determine the optimum parameters of bivariate Bingham distribution to obtain the ODF with the highest entropy and therefore may not be suitable for massive simulation of the SFRP part.

Numerous attempts have been made to apply an artificial neural network (ANN) in the field of constitutive modeling of composite materials to reduce computational costs, owing to increasing computing power and advanced algorithms [90]. Recently, several studies [101, 134-136] utilized the machine learning approach to predict the elastic or elasto–plastic properties of SFRPs. Breuer et al. [101] randomly generated approximately thousands of SFRP RVEs with various parameter combinations, including the elastic modulus of matrix, fiber aspect ratio, fiber volume fraction, and fiber orientation tensor. Short fibers were randomly distributed within the RVEs according to the ODF. The effective stiffness tensor of each RVE was calculated through numerical simulation with periodic boundary conditions rather than the two-step homogenization procedure. RVE parameters and effective stiffness tensor components were set as input features and output features of ANN, respectively. They reported that the trained ANN model exhibited equal or

slightly better performance compared with the two-step homogenization procedure. However, RVE-based approach has a limitation that an additional time-consuming data accumulation and training procedures are required for new materials with properties outside the input feature training range. Therefore, a combination of machine learning approach and two-step homogenization is essential.

In this chapter, we proposed a machine learning-assisted two-step homogenization framework of SFRPs. First, 10,000 pieces of arbitrary orientation tensor were generated. Subsequently, the ODF reconstruction procedure was performed using these data via the ME method. Next, the pseudograin decomposition procedure was performed with reconstructed ODF using the weighted k-means clustering algorithm. Subsequently, the orientation tensor, reconstructed ODF, and pseudograin decomposition data were used to construct and train several ANNs in a series–parallel arrangement. Finally, the machine learning-assisted two-step homogenization procedure comprising ANNs, Mori–Tanaka model, and Voigt model was implemented into the ABAQUS user material subroutine (UMAT), and its validity was confirmed via comparison with the experimental tensile test results. The graphical abstract of the overall procedure of this chapter is provided in **Figure 3-1**.

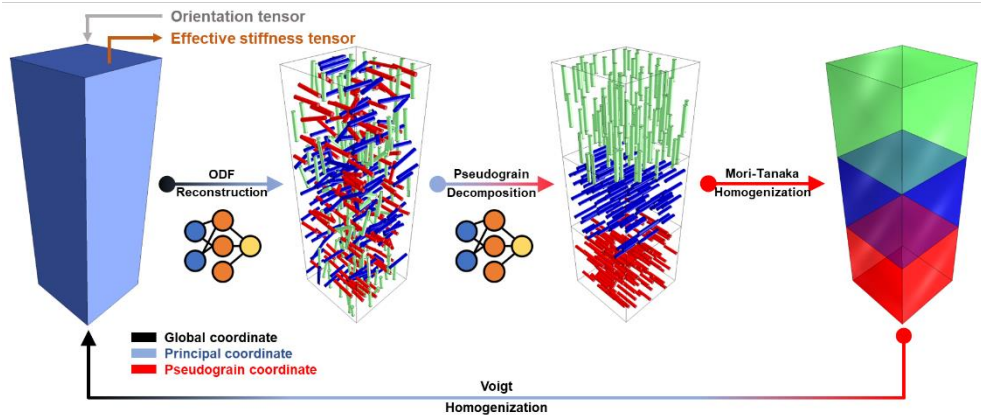

Figure 3-1 Graphical abstract of the overall procedure; the color change of the arrow indicates the rotation of the coordinates

3.2. Methods

3.2.1. Fiber orientation distribution function (ODF) and tensor

The fiber orientation unit vector $\boldsymbol{p}$ of a single ellipsoidal short fiber can be defined as follows.

$$\boldsymbol{p} = (\cos\theta\cos\phi,\ \sin\theta\cos\phi,\ \sin\phi) \qquad \textbf{Equation 3-1}$$

where θ is the angle between the x_1 axis and the projection of $\boldsymbol{p}$ on the $x_1 - x_2$ plane; and ϕ is the angle between $\boldsymbol{p}$ and the $x_1 - x_2$ plane (see **Figure 3-2**). To ensure the uniqueness of (θ, ϕ) combinations, the ranges of both θ and ϕ are limited to $\left[-\pi/2,\ \pi/2\right]$.

Given that numerous short fibers exist per unit volume of SFRP, treating all these orientation vectors is practically impossible. Therefore, to process orientation vector information statistically, the concept of orientation distribution function (ODF) $\psi(\boldsymbol{p})$, which corresponds to the probability of obtaining the fiber in direction $\boldsymbol{p}$, was proposed. The normalization condition of the ODF within the domain Ω is given by

$$\int_{\Omega} \psi(\boldsymbol{p})\, d\boldsymbol{p} = 1. \qquad \textbf{Equation 3-2}$$

To obtain the ODF information of SFRP manufactured *via* the injection molding process, the following Fokker–Plank equation, which describes the change of a distribution function of fluctuating macroscopic variables, is solved [132, 137].

$$\frac{\partial \psi}{\partial t} = -\nabla \cdot (\dot{\mathbf{p}}\psi) + D_r \nabla^2 \psi, \qquad \textbf{Equation 3-3}$$

where D_r is the fiber interaction coefficient determined by experimental results. However, solving **Equation 3-3** for 3D injection molding simulation is extremely time consuming. Instead, the commercial injection molding simulation software (such as MOLDEX3D and MOLDFLOW) adopts the fiber orientation model, i.e., Folgar–Tucker equation [138] (**Equation 3-4**), to describe the change of the second-order fiber orientation tensor a_{ij} during the manufacturing process, as follows.

$$\frac{\partial a_{ij}}{\partial t} = -\frac{1}{2}\left(\omega_{ik}a_{kj} - a_{ik}\omega_{kj}\right) + \frac{\lambda}{2}\left(\dot{\gamma}_{ik}a_{kj} + a_{ik}\dot{\gamma}_{kj} - 2a_{ijkl}\dot{\gamma}_{kl}\right) + 2D_r\left(\delta_{ij} - 3a_{ij}\right), \textbf{ Equation 3-4}$$

where ω_{ij} is the vorticity tensor; $\dot{\gamma}_{ij}$ is the deformation rate tensor; and a_{ijkl} is the fourth-order fiber orientation tensor, which should be obtained from the orthotropic [139] or hybrid [140] closure approximation. Bauer has reported details on how to obtain the orientation tensor a_{ij} or a_{ijkl} from the ODF $\psi(\boldsymbol{p})$ [141].

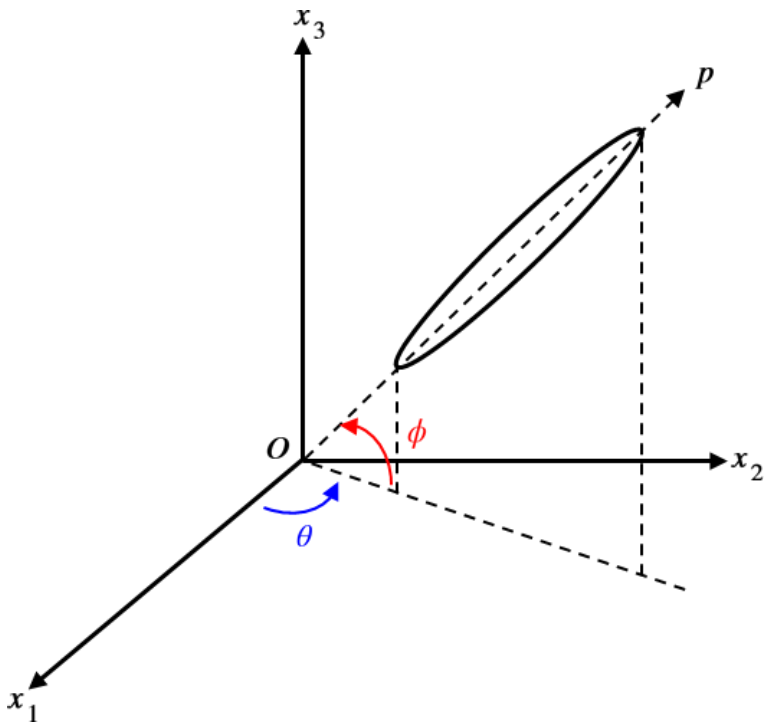

Figure 3-2 Schematic of the fiber orientation unit vector $\boldsymbol{p}$ of a single ellipsoidal short fiber in the global Cartesian coordinate system

3.2.2. ODF reconstruction

Using the orientation tensor for the mechanical simulation of SFRP presents a critical problem because two completely different ODFs (e.g., unidirectional with two maxima and planar isotropy [132]) may have the same orientation tensor. Therefore, a reconstruction model that can specify an ODF for a given orientation tensor is required. The most widely used model is maximum entropy (ME) method [129], which was developed based on empirical observation that the microstructures of injection molded SFRPs tend to have the maximum entropy. In this study, the interpretation of Breuer et al. [132] to determine the ODF with maximum entropy with a bivariate Bingham distribution on the unit sphere was adopted.

The first step of the ME reconstruction is to divide (θ, ϕ) of a unit sphere into several equivalent triangular meshes based on the icosphere concept. The 0^{th}-order icosphere is a regular icosahedron comprising 20 equivalent triangular meshes. Note that the coordinates of the centroid of each triangle represent the orientation unit vector $\boldsymbol{p}$. The $(n+1)^{th}$-order icosphere is generated by dividing each triangular mesh of the n^{th}-order icosphere into four smaller triangles.

Next, $\mathbb{P}_k = \left(P_{1k}, P_{2k}, P_{3k} \right)$ is defined as a unit direction vector vertical to the k^{th} surface of icosphere as shown in **Figure 3-3**. Accordingly, $\psi\left(\mathbb{P}_k \right)$ is defined using the following form of a bivariate Bingham distribution.

$$\psi\left(\mathbb{P}_k \right) = Ce^{-\alpha P_{3k}^2 + \beta P_{1k}^2}, \qquad \textbf{Equation 3-5}$$

where α and β are two Bingham distribution parameters; and C is a normalization constant obtained from the normalize condition in **Equation 3-2**. The orientation tensor a_{ij} and the entropy S in the given situation can be calculated using the following **Equation 3-6** and **Equation 3-7**.

$$a_{ij} = \sum_k P_{ik} P_{jk} \psi\left(\mathbb{P}_k\right), \qquad \textbf{Equation 3-6}$$

$$S = -\sum_k \psi\left(\mathbb{P}_k\right) \ln\left(\psi\left(\mathbb{P}_k\right)\right). \qquad \textbf{Equation 3-7}$$

The final step is the determination of α and β values that maximize the entropy *via* minimization procedure. However, this procedure is not straightforward because it requires minimizing two objective functions f_1 and f_2 simultaneously:

$$f_1(\alpha,\beta) = \sum_{ij} \left(\frac{a_{ij}^{given} - a_{ij}(\alpha,\beta)}{a_{ij}^{given}} \right)^2, \qquad \textbf{Equation 3-8}$$

$$f_2(\alpha,\beta) = \left(\frac{S_{max}^{global} - S(\alpha,\beta)}{S_{max}^{global}} \right)^2, \qquad \textbf{Equation 3-9}$$

where a_{ij}^{given} is the target orientation tensor; and S_{max}^{global} is the global maximum entropy of 8.54 corresponding to $a_{ij} = \left[1/3,\ 1/3,\ 1/3\right]$. Herein, a Pareto optimization method was employed to minimize two objective functions simultaneously.

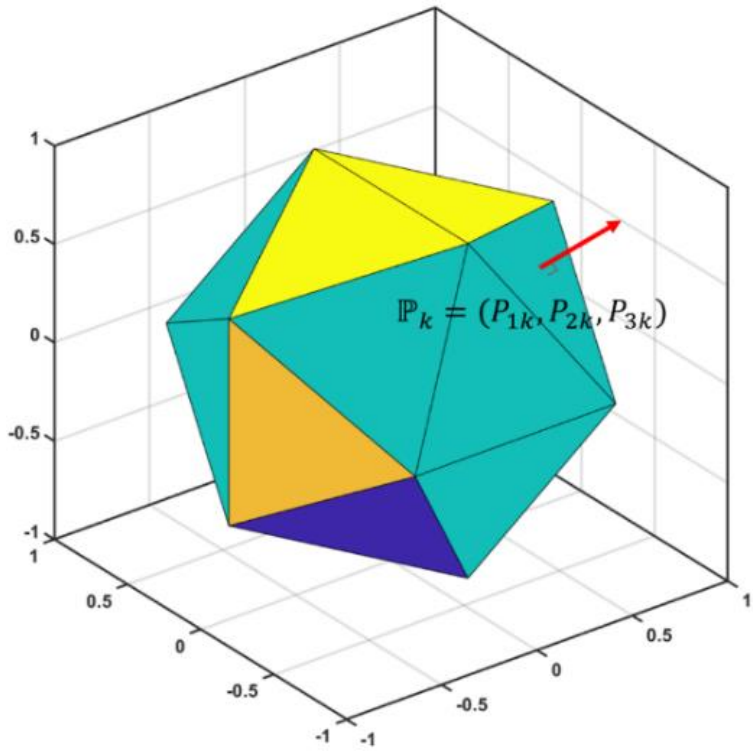

Figure 3-3 Unit direction vector vertical to the k^{th} surface of 0^{th}-order icosphere

3.2.3. Pseudograin decomposition

Upon completion of the reconstruction procedure, the ODF is decomposed into several pseudograins with unidirectionally aligned short fibers. The decomposition procedure is intended to satisfy the requirement of the homogenization models that the target composite must have inclusions of similar shape and orientation.

Typically, pseudograin decomposition methodologies are of two types: iso-facets algorithm and equivalent orientation approach. Numerous homogenization studies [111, 142] employed the iso-size facet algorithm proposed by Weber et al. [125] to form infinitesimal pseudograins. In this algorithm, the surface of the unit sphere is divided into facets of almost equal areas with the equal-sized increments of θ and the corresponding values of ϕ. Each facet represents a single pseudograin, and typically, hundreds to thousands of infinitesimal pseudograins can be defined. Gommers et al. [124] introduced a new concept of "equivalent orientations." The requirement for the equivalent orientations is that they have the same 4^{th} order orientation tensor a_{ijkl} as the original ODF. The solution could be found by treating the set of non-linear equations as a minimization problem.

Ogierman et al. [112] performed comparative analysis between the abovementioned two pseudograin decomposition methods. They fixed the number of equivalent orientations at nine and 18 and found the optimum orientations using an evolutionary algorithm. Two conclusions of the study

conducted by Ogierman et al. can be summarized as follows. 1) Nine pseudograins were sufficient for an appropriate representation of the original ODF. 2) Equivalent orientation determined by the evolutionary algorithm provided more accurate result compared with the existing studies. However, the high computational cost caused by the evolutionary algorithm was a problem to be solved. In this study, a weighted k-means clustering algorithm was employed instead of evolutionary algorithm to dramatically reduce the computation time while maintaining a high accuracy.

k-means clustering algorithm, also known as Lloyd's algorithm [143], is an algorithm that partitions a set of n data points $\mathbb{X} = \left(x_1, x_2, \cdots, x_n \right)$ into k $(\leq n)$ clusters. The algorithm starts with defining a set of k arbitrary centroids $\mathbb{C} = \left(c_1, c_2, \cdots, c_k \right)$ that is chosen uniformly at random from $\mathbb{X}$. Each data point in $\mathbb{X}$ is assigned to the nearest centroid in terms of the Euclidean distance, and the data points assigned to the same centroid form a cluster. Thereafter, Centroid $\mathbb{C}$ is updated with the center of mass of data points in the same cluster, and this process is repeated until the change in centroid position becomes smaller than the tolerance value. Different from general k-means clustering, weighted k-means clustering assigns weights $\mathbb{W} = \left(w_1, w_2, \cdots, w_n \right)$ to each data point $\mathbb{X}$ when calculating the new center of mass $\mathbb{C}$.

3.3. Experimental

3.3.1. Materials and specimens

The proposed homogenization framework in this study was validated by comparing tensile test results with numerical simulation results of SFRP named as PP-GF30, in which short glass fibers (GF) with a weight fraction of 30 % were embedded in a polypropylene (PP) matrix. Note that a fiber weight fraction of 30 % corresponds to the fiber volume fraction of 13.09 %. The material properties of constituents PP and GF are listed in **Table 3-1**.

The PP pellet and GF were mixed and were injection-molded into a flat mold with dimensions of 300 × 160 × 4 mm^3. Tensile test specimens were cut from the center region of PP-GF30 plate in accordance with Type 1A test specimen dimension of ISO 527-2 standard [144]. Five PP-GF30-0D specimens were prepared, whereby they were cut parallel to the flow direction. The details of the tensile test specimen are provided in **Figure 3-4**.

Table 3-1 Material properties of polypropylene (PP) and short glass fiber (GF)

Material	**PP**	**PP**
Density (ρ)	0.90 g/cm^3	2.56 g/cm^3
Elastic modulus (E)	1.91 GPa	72.40 GPa
Poisson's ratio (v)	0.43	0.22
Fiber aspect ratio (a_r)	-	25

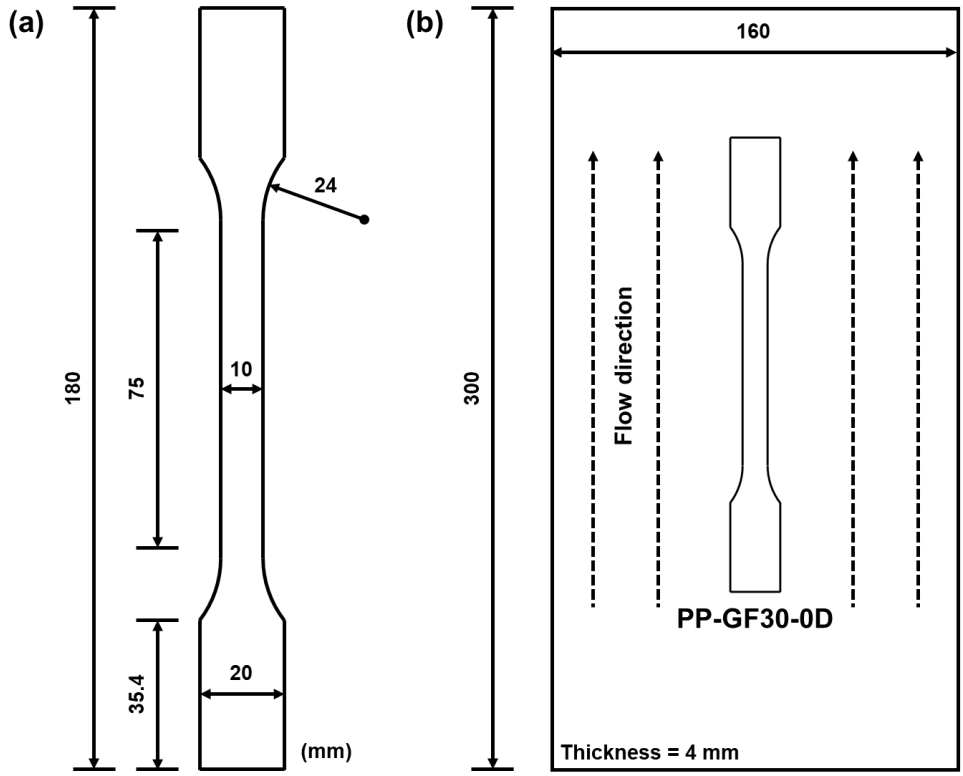

Figure 3-4 Schematic of (a) Type 1A test specimen dimension of ISO 527-2 standard and (b) PP-GF30-0D from PP-GF30 plate

3.3.2. Tensile test conditions

Tensile tests were performed using a tensile testing machine (Instron 8801; Instron, Norwood, MA, USA) at a recommended test speed of 5 mm/min and room temperature (25 ℃). A digital image correlation (DIC) system (Vic-3D v7; Correlated Solutions, Inc., Irmo, SC, USA) was used to obtain the full-field displacement distribution and tensile strain. Black-and-white speckled patterns were sprayed on the tensile test specimens for DIC measurement. The details of the experiment are shown in **Figure 3-5**.

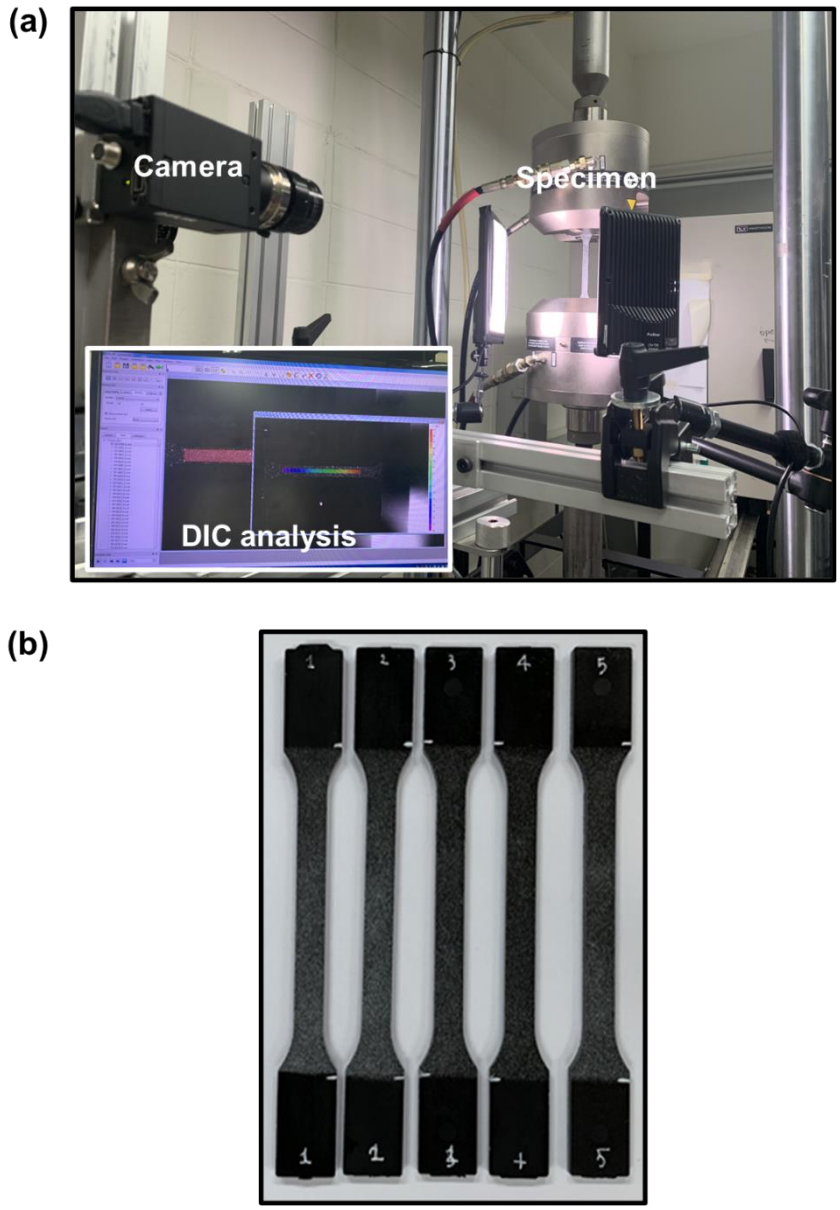

Figure 3-5 (a) Experimental setup for the tensile test with DIC system, and (b) five tensile test specimens with black-and-white speckled pattern

3.4. Results and Discussion

3.4.1. Implementation of pseudograin decomposition procedure

The details of the implementation of ODF reconstruction and pseudograin decomposition procedure in MATLAB are discussed. Note that only diagonal orientation tensors were considered because any arbitrary orientation tensor with an off-diagonal term can be transformed into a diagonal tensor by coordinate transformation (using eigen values and vectors). In this section, an example of ODF reconstruction result using ME and pseudograin decomposition result using weighted k-means clustering for a diagonal orientation tensor of $a_{ij} = \left[0.7,\ 0.15,\ 0.15\right]$ is explained. A workstation with Intel(R) Core(TM) i7-10700K CPU @ 3.80 GHz (8 cores) and 16GB RAM is used.

3.4.1.1. Implementation of ODF reconstruction procedure

The ODF reconstruction procedure introduced in **Section 3.2.2** was implemented in MATLAB. As previously mentioned, ODF reconstruction using ME model requires two objective functions f_1 (**Equation 3-8**) and f_2 (**Equation 3-9**) to be minimized simultaneously to obtain the optimum α and β values of a bivariate Bingham distribution in **Equation 3-5**. However, this multi-objective optimization problem is rather complicated because the solution is not a single point where both objective functions are at their optimum but rather a set of non-dominated points where one objective function cannot be improved without having a detrimental effect on the other [145]. These sets of non-dominated points are also called Pareto front. Pareto optimization method [146] based on genetic algorithm was used to determine the Pareto front of our reconstruction problem.

The 4^{th}-order icosphere with 5,120 triangular meshes (see **Figure 3-6(a)**) was used for the reconstruction problem, which demonstrated adequate performance in terms of both the computational cost and accuracy. Note that half of the total triangular meshes was considered, essentially accounting for the symmetry of a unit sphere. The target diagonal orientation tensor and the ranges of both α and β were set to $a_{ij} = [0.7,\ 0.15,\ 0.15]$ and $[0,\ 10]$, respectively. A random initial population of α and β was created with a uniform distribution. Pareto optimization was performed under these conditions (see **Figure 3-7**). A total of 20 red circles can be observed in

Figure 3-7, each corresponding to a local minimum for a given multi-objective optimization problem. Given that the target diagonal orientation tensor must be strictly recovered, the red circle located at the top left was selected as the final ODF reconstruction result. If another red circle is selected, a high entropy value can be obtained, but the original purpose is lost because the difference with the target orientation tensor becomes large. The finally determined values of α and β were 0.09 and 3.91, respectively. The α and β values provide the diagonal orientation tensor of $a_{ij} = [0.6999,\ 0.1502,\ 0.1499]$ and entropy of 7.84. The 3D plot of reconstructed ODF is shown in **Figure 3-6(b)**, which indicates the feasibility of the reconstruction procedure.

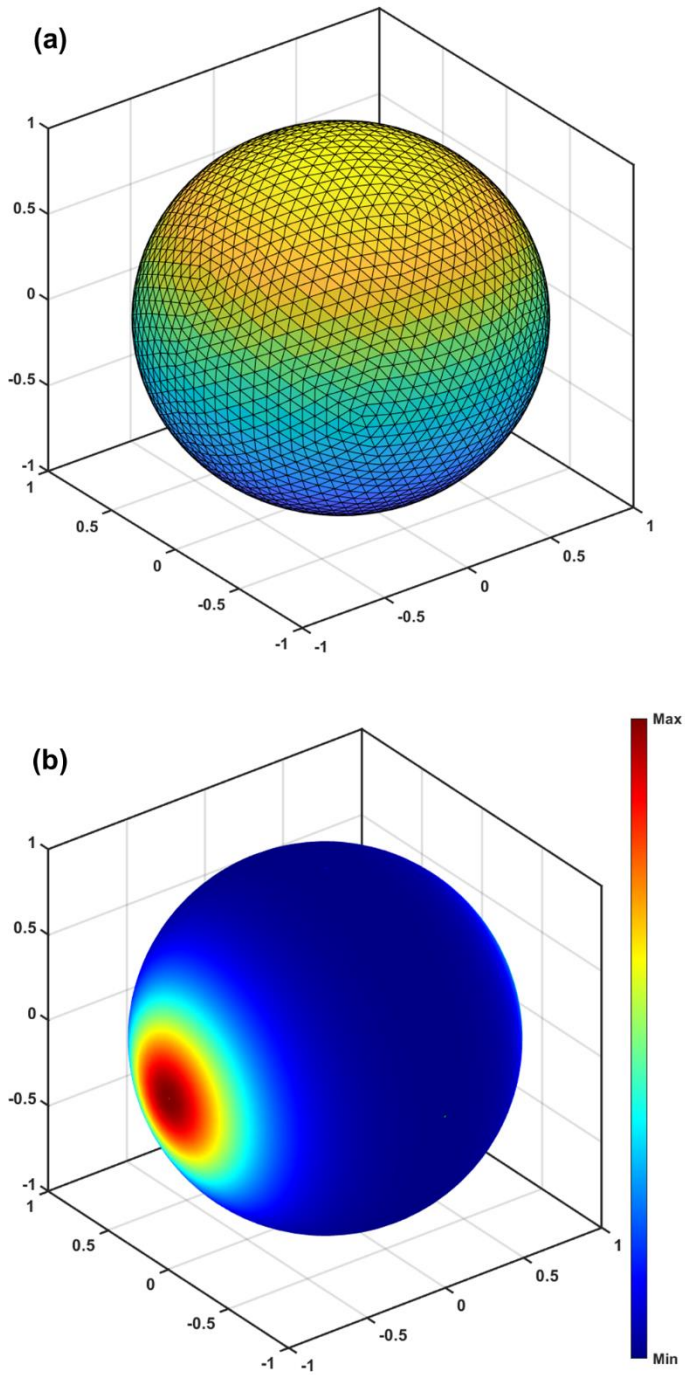

Figure 3-6 (a) Total of 5,120 triangular meshes of 4th-order icosphere and (b) reconstructed ODF from the diagonal orientation tensor $a_{ij} = [0.7,\ 0.15,\ 0.15]$

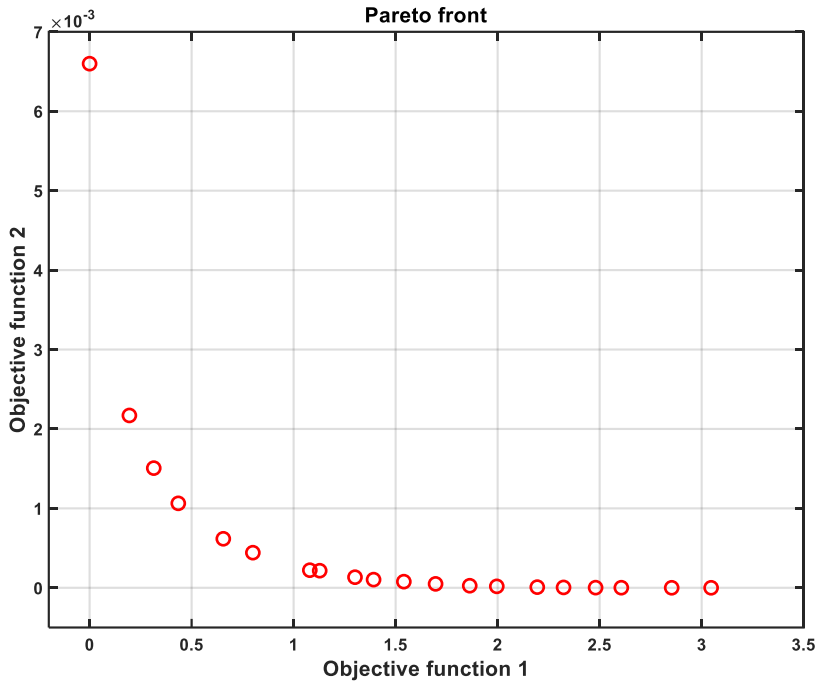

Figure 3-7 Pareto front of the reconstruction problem of the diagonal orientation tensor $a_{ij} = [0.7,\ 0.15,\ 0.15]$; the objective functions 1 and 2 correspond to **Equation 3-8** and **Equation 3-9**, respectively

3.4.1.2. Implementation of pseudograin decomposition procedure

The pseudograin decomposition procedure using a weighted k-means clustering algorithm was implemented in MATLAB. In our problem of applying weighted k-means clustering to pseudograin decomposition procedure, the 6th-order icosphere with 81,920 triangular meshes was used, which demonstrated adequate performance in terms of both computational cost and accuracy. Note that half of the total triangular meshes were considered due to the symmetry of a unit sphere. The set of data points $\mathbb{X}$ is defined with a unit direction vector vertical to the surfaces of the 6th-order icosphere, as follows.

$$\mathbb{X} = \left(\mathbb{P}_1, \mathbb{P}_2, \cdots, \mathbb{P}_{40960} \right). \qquad \textbf{Equation 3-10}$$

The set of weights $\mathbb{W}$ of each data point in $\mathbb{X}$ is defined with the ODF ψ defined in **Equation 3-5**, as follows.

$$\mathbb{W} = \left(\psi\left(\mathbb{P}_1 \right), \psi\left(\mathbb{P}_2 \right), \cdots, \psi\left(\mathbb{P}_{40960} \right) \right). \qquad \textbf{Equation 3-11}$$

An illustration of the sets $\mathbb{X}$ and $\mathbb{W}$ in $\theta - \phi$ space for the reconstructed ODF in **Figure 3-6(b)** is given in **Figure 3-8(a)**. The number of clusters, i.e., pseudograins, were fixed to 12 [112, 147]. As can be seen in **Figure 3-8(a)**, the bivariate Bingham distribution used for ODF reconstruction was symmetric with respect to the x-axis, y-axis, and the origin of $\theta - \phi$ space. Therefore, a strategy was proposed to obtain a total of 12 pseudograins by performing k = 3 clustering in the first quadrant and reflecting the result about the x-axis, y-axis, and the origin in sequence. This

strategy will not only reduce the computational cost of the decomposition procedure itself but also enhance the trainability of artificial neural network by simplifying the data structure. For defining a set of initial arbitrary centroids, k -means++ seeding algorithm proposed by Arthur and Vassilvitskii [148] was used.

The first quadrant of **Figure 3-8(a)** was decomposed into three pseudograins via weighted k-means clustering using the above datasets under the aforementioned conditions, and the clustering result is shown in **Figure 3-8(b)**. The centroid of each cluster indicated by "x" mark corresponds to the equivalent orientation (θ, ϕ) of each pseudograin. The sum of ODF in each cluster $\sum_{i \in cluster} \psi\left(\mathbb{P}_i\right)$ corresponds to the volume fraction of a pseudograin. These data for pseudograin 1 (PG1), pseudograin 2 (PG2), and pseudograin 3 (PG3) are summarized in **Table 3-2**. Note that the sequence of the pseudograins was determined by the centroid's distance from the origin.

Table 3-2 Equivalent orientations and volume fractions of pseudograins in **Figure 3-8(b)**

Pseudograin	Equivalent orientation	Volume fraction
PG1	(0.24, 0.19)	58.36 %
PG2	(0.29, 0.65)	22.96 %
PG3	(0.93, 0.40)	18.68 %

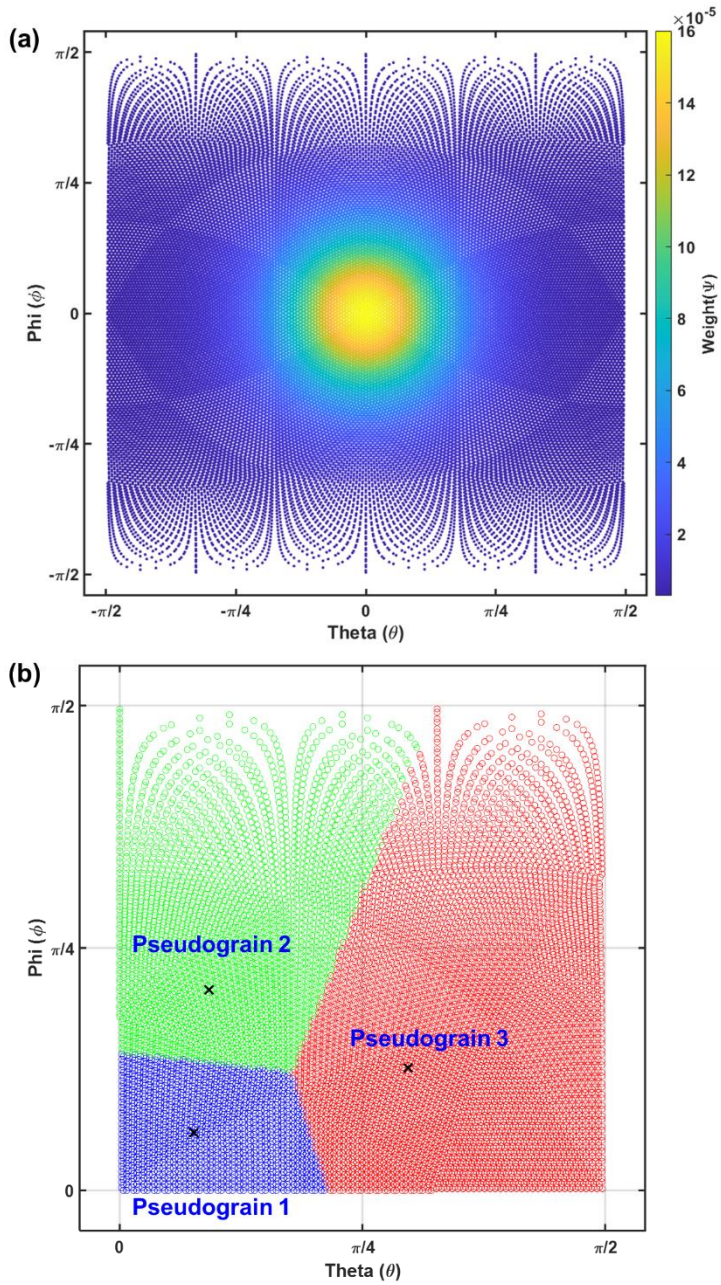

Figure 3-8 (a) Illustration of the sets $\mathbb{X}$ and $\mathbb{W}$ in $\theta-\phi$ space for the reconstructed ODF in **Figure 3-6(b)**; sets $\mathbb{X}$ and $\mathbb{W}$ are represented with circles and colormap, respectively. (b) Pseudograin decomposition result of the first quadrant of (a); the centroid of each pseudograin is indicated by "x" mark

3.4.2. Construction of artificial neural network system

ODF reconstruction and pseudograin decomposition procedure implemented in MATLAB are based on iterative minimization procedures. When these are combined with user material subroutines for part-level simulation with different orientation tensor information for each element, the computation time inevitably increases exponentially. Therefore, a concept of ANN trained with an extensive amount of pre-calculated ODF reconstruction and pseudograin decomposition data was adopted herein.

3.4.2.1. Series–parallel artificial neural network system

A series–parallel ANN system consisting of five fully connected ANNs was proposed to train ODF reconstruction and pseudograin decomposition procedures. The schematic of this ANN system is presented in **Figure 3-9**. The first ANN is named "OT2AB", which implies that it outputs α and β (AB) of bivariate Bingham distribution from the diagonal orientation tensor (OT) input data. The same nomenclature was adopted for the rest of the ANNs. The 2nd–4th ANNs are named "AB2TPi" ($i = 1.\ 2.\ 3$), which imply that they provide equivalent orientations ($\theta,\ \phi$) of PG1, PG2, and PG3, respectively, from α and β input data obtained from OT2AB. The last ANN is named "AB2VF", which implies that it outputs volume fractions of PG1, PG2, and PG3 from α and β input data obtained from OT2AB. The remaining information of PG4 to PG12 were generated by reflecting the information of PG1–PG3 about the x-axis, y-axis, and the origin in sequence.

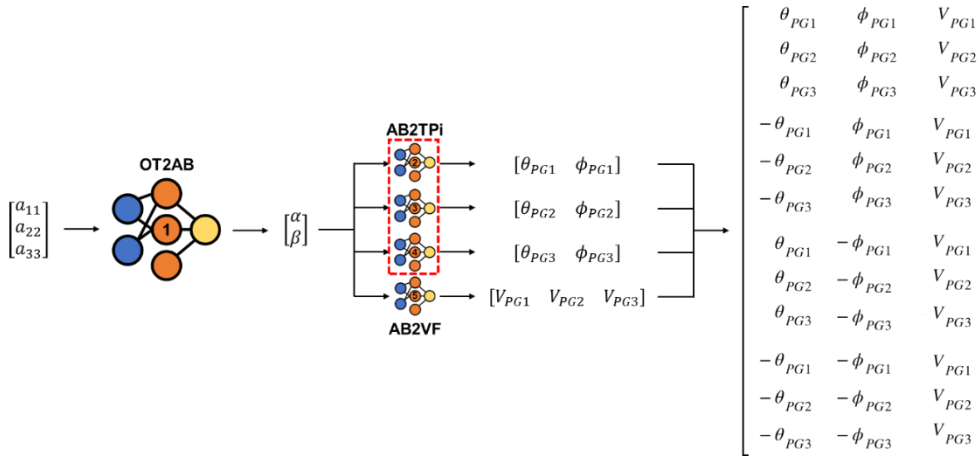

Figure 3-9 Schematic of a series–parallel artificial neural network system

3.4.2.2. Generation of input data and calculation of output data

To train the series–parallel artificial neural network system, 10,000 diagonal orientation tensors were generated from 10 a_{11} intervals, as presented in **Table 3-3**. To generate one input diagonal orientation tensor data $[a_{11}, a_{22}, a_{33}]$, a_{11} is chosen uniformly at random from an interval, and the remaining two components a_{22} and a_{33} are determined based on the following two conditions ($a_{11}+a_{22}+a_{33}=1$ and $a_{11}>a_{22}>a_{33}$). The intervals and number of data are concentrated on both extremes to capture the sharp change of the reconstruction result.

ODF reconstruction and pseudograin decomposition procedures implemented in **Section 3.4.1** were repeatedly performed using the generated input data. A typical example for orientation tensors [0.98, 0.01, 0.01], [0.56, 0.27, 0.14], [0.49, 0.49, 0.02], and [0.34, 0.33, 0.33] are presented in **Table 3-4** and **Figure 3-10**.

Table 3-3 Ten a_{11} intervals in which input diagonal orientation tensor data are generated

a_{11} **interval**	**Number of data**	a_{11} **interval**	**Number of data**
[0.333, 0.340)	1000	[0.700, 0.800)	1000
[0.340, 0.400)	1000	[0.800, 0.900)	1000
[0.400, 0.500)	1000	[0.900, 0.950)	1000
[0.500, 0.600)	1000	[0.950, 0.995)	1000

Table 3-4 Typical example of ODF reconstruction and pseudograin decomposition result

$\left[a_{11}, a_{22}, a_{33}\right]$	**[0.97, 0.02, 0.01]**	**[0.56, 0.27, 0.14]**	**[0.49, 0.48, 0.03]**	**[0.35, 0.33, 0.32]**
α	29.21	1.98	16.67	0.08
β	23.91	1.21	0.13	0.15
$\left(\theta_{PG1}, \phi_{PG1}\right)$	(0.07, 0.04)	(0.32, 0.21)	(0.24, 0.14)	(0.32, 0.49)
$\left(\theta_{PG2}, \phi_{PG2}\right)$	(0.08, 0.15)	(0.44, 0.74)	(0.77, 0.14)	(1.13, 0.30)
$\left(\theta_{PG3}, \phi_{PG3}\right)$	(0.24, 0.07)	(1.12, 0.33)	(1.29, 0.14)	(1.02, 1.01)
$\left(V_{PG1}, V_{PG2}, V_{PG3}\right)$	(0.50, 0.25, 0.25)	(0.47, 0.18, 0.35)	(0.32, 0.35, 0.33)	(0.42, 0.34, 0.24)

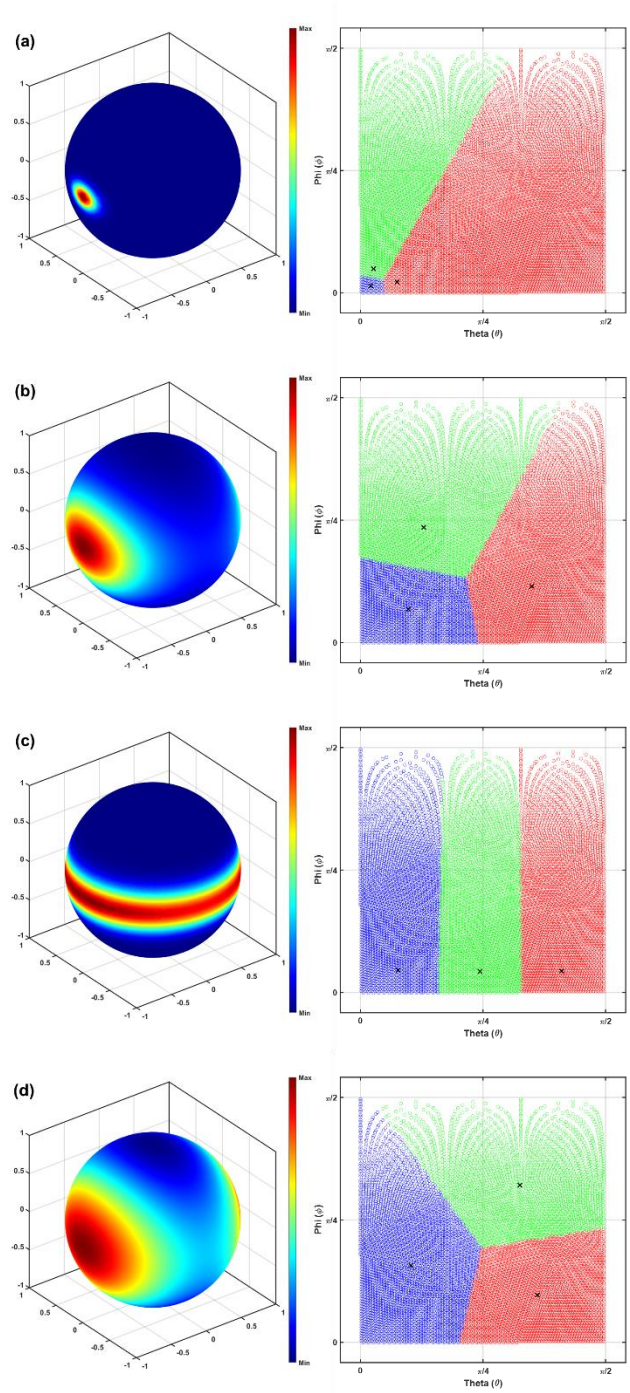

Figure 3-10 Typical example of ODF reconstruction and pseudograin decomposition result for orientation tensors (a) [0.97, 0.02, 0.01], (b) [0.56, 0.27, 0.14], (c) [0.49, 0.48, 0.03], and (d) [0.35, 0.33, 0.32]

3.4.2.3. Training series-parallel ANN system

Herein, the proposed series–parallel ANN system was trained with the accumulated data from **Section 3.4.2.2.** using MATLAB Deep Learning Toolbox. All ANNs (OT2AB, AB2PG1, AB2PG2, AB2PG3, and AB2VF) were designed to have five hidden layers and 10 hidden neurons in each of hidden layer. Bayesian regularization backpropagation algorithm was used, and the mean squared error was used as the performance metric. The hyperbolic tangent sigmoid transfer function was applied to the input and hidden layers. The linear transfer function was applied to the output layer. Furthermore, 10,000 input data were randomly divided into training, testing, and validation datasets in proportions of 70, 15, and 15 %, respectively. The training epoch was stopped if the error increased more than 20 times during the validation procedure to prevent overfitting.

The training result for OT2AB is presented in **Figure 3-11** as a regression plot and training state plot. The best performance was achieved at the 764^{th} epoch with an approximated R-square value of 1, thus indicating that the training process was successful. The training results for the remaining four ANNs (AB2PG1, AB2PG2, AB2PG3, and AB2VF) are also presented in **Figure 3-12**, essentially demonstrating the successful training process again.

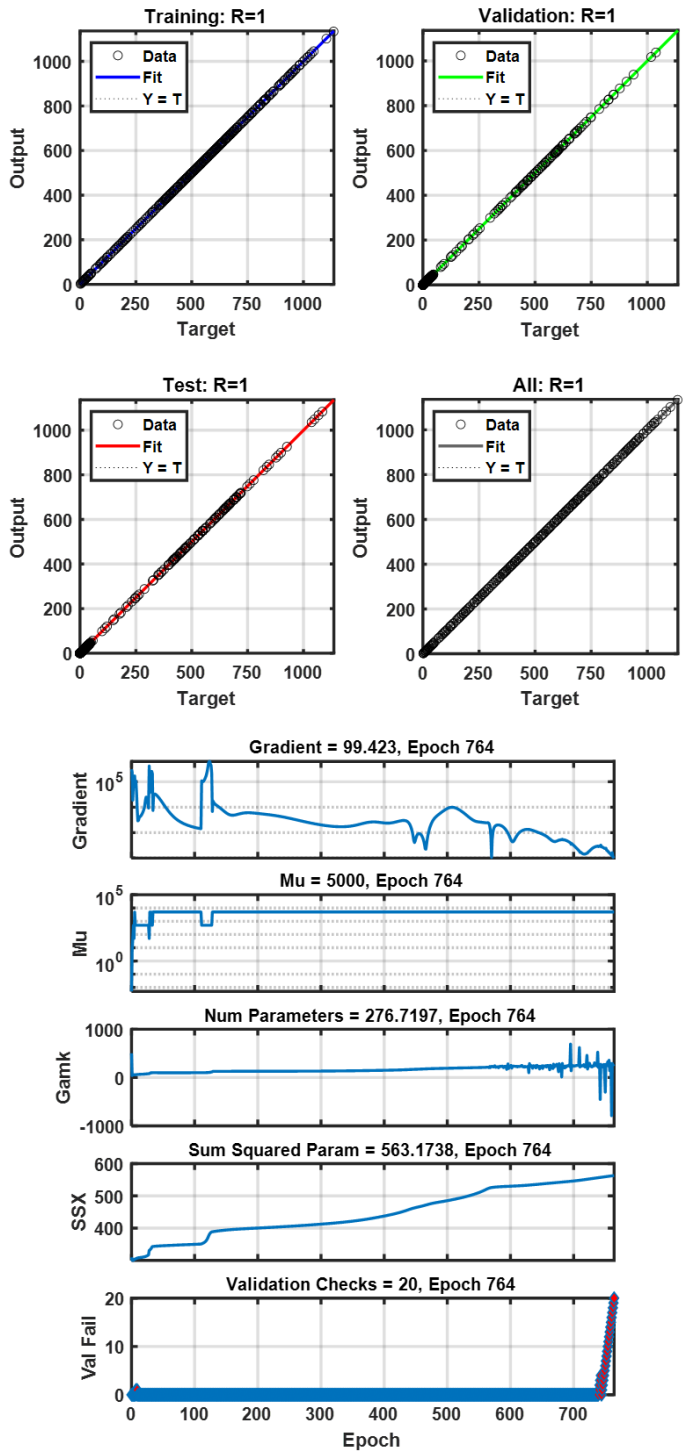

Figure 3-11 Regression and training state plot of OT2AB training result

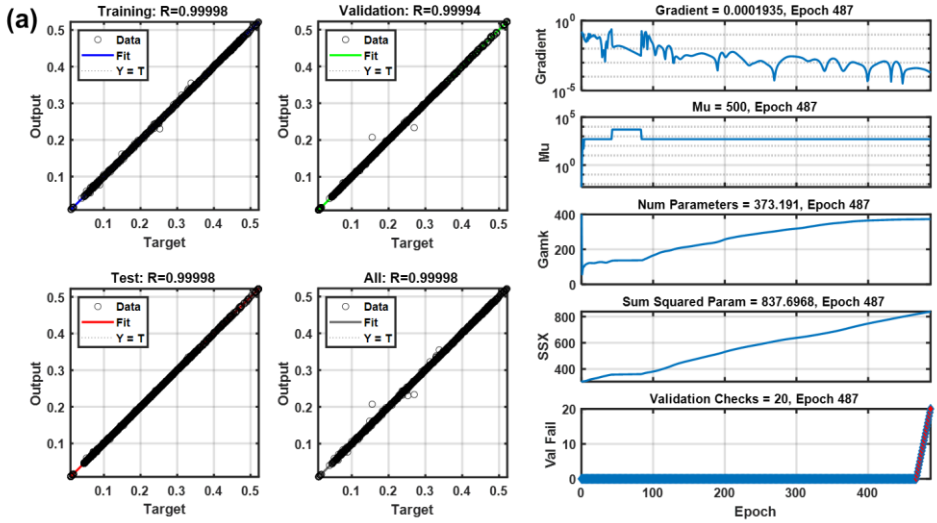
(a)
Training: R=0.99998
Validation: R=0.99994
Test: R=0.99998
All: R=0.99998
Data
Fit
Y = T
Output
Target
Gradient = 0.0001935, Epoch 487
Mu = 500, Epoch 487
Num Parameters = 373.191, Epoch 487
Sum Squared Param = 837.6968, Epoch 487
Validation Checks = 20, Epoch 487
Gradient
Mu
Gamk
SSX
Val Fail
Epoch

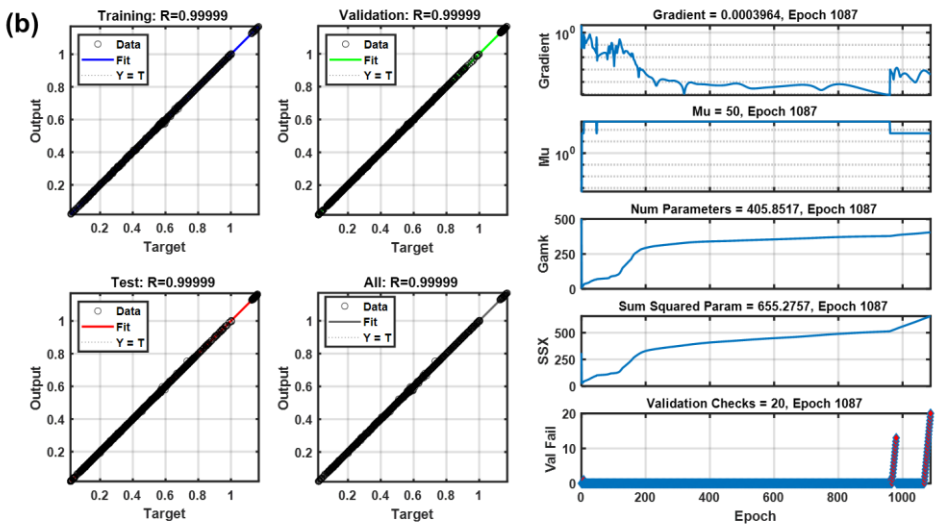
(b)
Training: R=0.99999
Validation: R=0.99999
Test: R=0.99999
All: R=0.99999
Data
Fit
Y = T
Output
Target
Gradient = 0.0003964, Epoch 1087
Mu = 50, Epoch 1087
Num Parameters = 405.8517, Epoch 1087
Sum Squared Param = 655.2757, Epoch 1087
Validation Checks = 20, Epoch 1087
Gradient
Mu
Gamk
SSX
Val Fail
Epoch

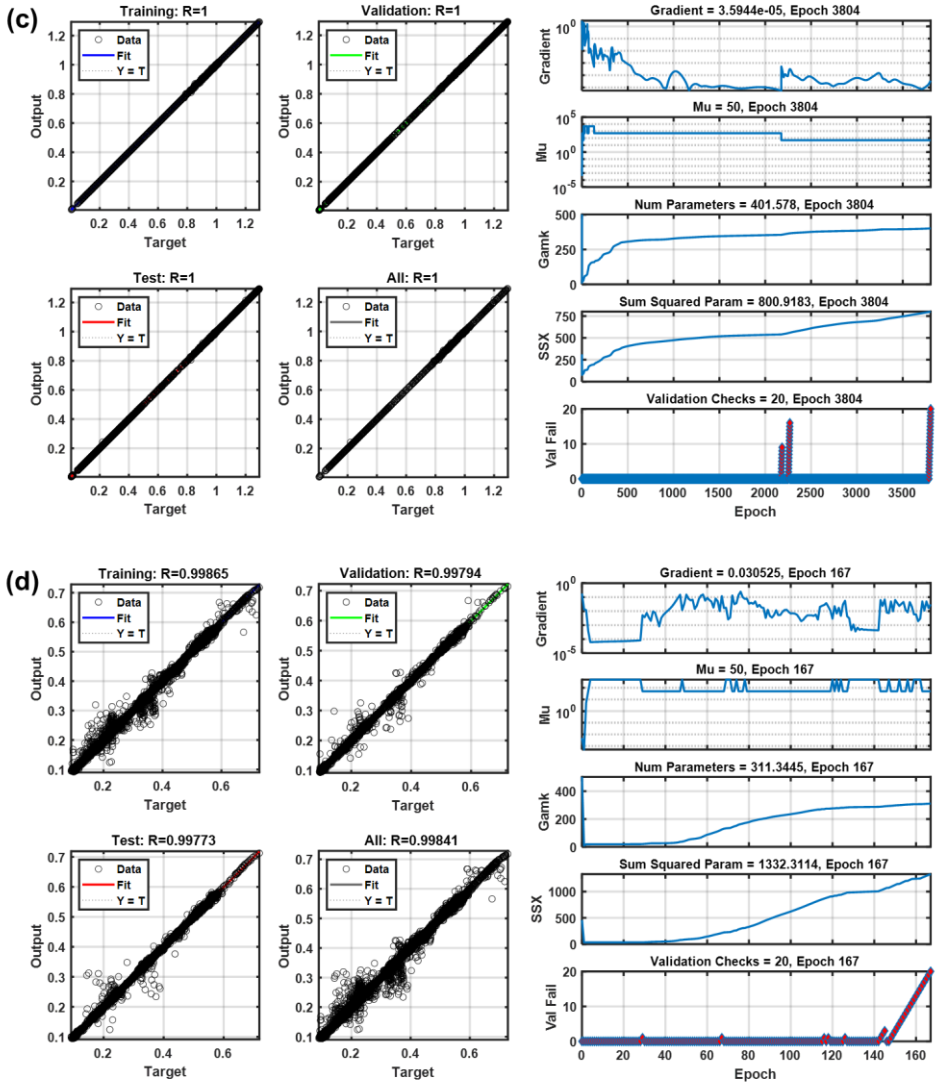

Figure 3-12 Regression and training state plots of (a) AB2PG1, (b) AB2PG2, (c) AB2PG3, and (d) AB2VF training results

3.4.3. Numerical implementation and validation

A machine learning-assisted two-step homogenization procedure comprising a series–parallel ANN system, Mori–Tanaka model, and Voigt model (recall **Figure 3-1**) was implemented in ABAQUS using a user material subroutine (UMAT). First, the algorithmic implementation of UMAT was validated by solving a simple tensile problem using both UMAT and DIGIMAT. Next, the UMAT was validated by comparing the UMAT re-simulation result with the experimental tensile test result.

3.4.3.1. Comparison of UMAT results with DIGIMAT for a simple tensile problem

A simple tensile problem was performed using both UMAT and DIGIMAT to validate the algorithmic implementation of UMAT. A cubic geometry of dimension 4 × 4 × 4 mm^3 was created and meshed with a C3D8 element of dimension 0.04 × 0.04 × 0.04 mm^3. The x- (U1 = UR2 = UR3 = 0), y- (U2 = UR1 = UR3 = 0), and z-symmetry (U3 = UR1 = UR2 = 0) boundary conditions were applied to the plane perpendicular to the x-, y-, and z-axis in the negative direction, respectively. A displacement boundary condition of 0.004 mm was applied to the plane perpendicular to the x-axis in the positive direction, such that the applied tensile strain was 0.1 %.

Two extreme diagonal orientation tensors and six non-diagonal orientation tensors were considered. The effective stiffness tensors corresponding to each orientation tensor were calculated using the UMAT and DIGIMAT-MF module with the material properties in **Table 3-1**. Note that the skin-core structure of SFRP is not considered in this case. The tensile stress–strain curves and von Mises stress distribution obtained by UMAT and DIGIMAT are compared in **Figure 3-13** and **Figure 3-14**, respectively. Evidently, the tensile stress–strain curves obtained by UMAT exhibited computation time within 1 s, and good performance within 2 % error on average compared with DIGIMAT regardless of the features of target orientation tensor.

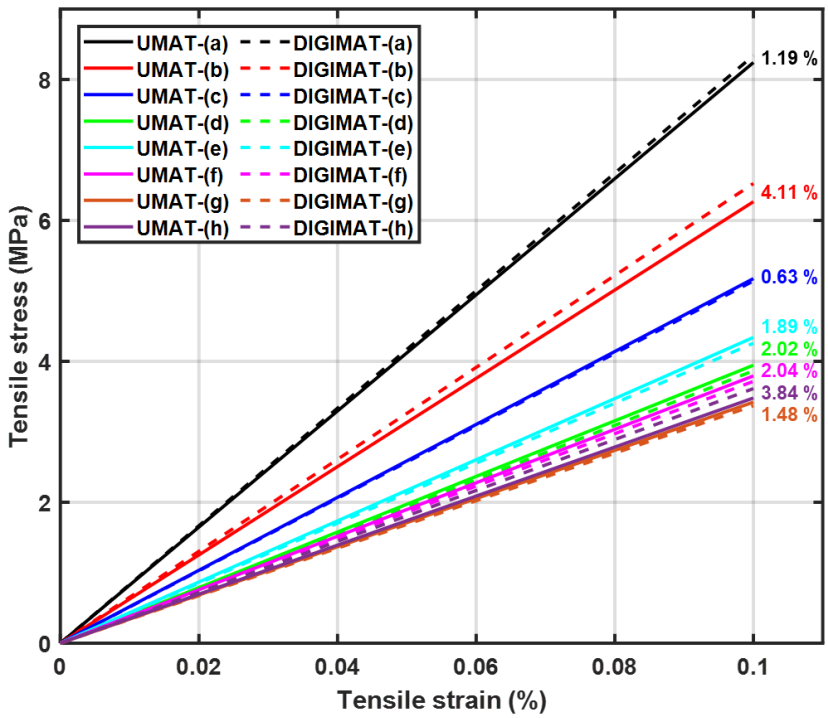

$$\begin{bmatrix} 0.97 & 0 & 0 \\ & 0.02 & 0 \\ & & 0.01 \end{bmatrix} \quad (a) \qquad \begin{bmatrix} 0.89 & -0.18 & 0.08 \\ & 0.04 & -0.01 \\ & & 0.06 \end{bmatrix} \quad (b)$$

$$\begin{bmatrix} 0.73 & 0.19 & -0.14 \\ & 0.18 & -0.04 \\ & & 0.09 \end{bmatrix} \quad (c) \qquad \begin{bmatrix} 0.63 & -0.34 & -0.06 \\ & 0.25 & 0.02 \\ & & 0.12 \end{bmatrix} \quad (d)$$

$$\begin{bmatrix} 0.58 & 0.22 & -0.02 \\ & 0.21 & -0.01 \\ & & 0.21 \end{bmatrix} \quad (e) \qquad \begin{bmatrix} 0.45 & -0.21 & -0.08 \\ & 0.49 & -0.07 \\ & & 0.06 \end{bmatrix} \quad (f)$$

$$\begin{bmatrix} 0.36 & 0.19 & -0.03 \\ & 0.45 & -0.05 \\ & & 0.20 \end{bmatrix} \quad (g) \qquad \begin{bmatrix} 0.35 & 0 & 0 \\ & 0.33 & 0 \\ & & 0.32 \end{bmatrix} \quad (h)$$

Figure 3-13 Comparison of tensile stress–strain curves obtained by UMAT and DIGIMAT

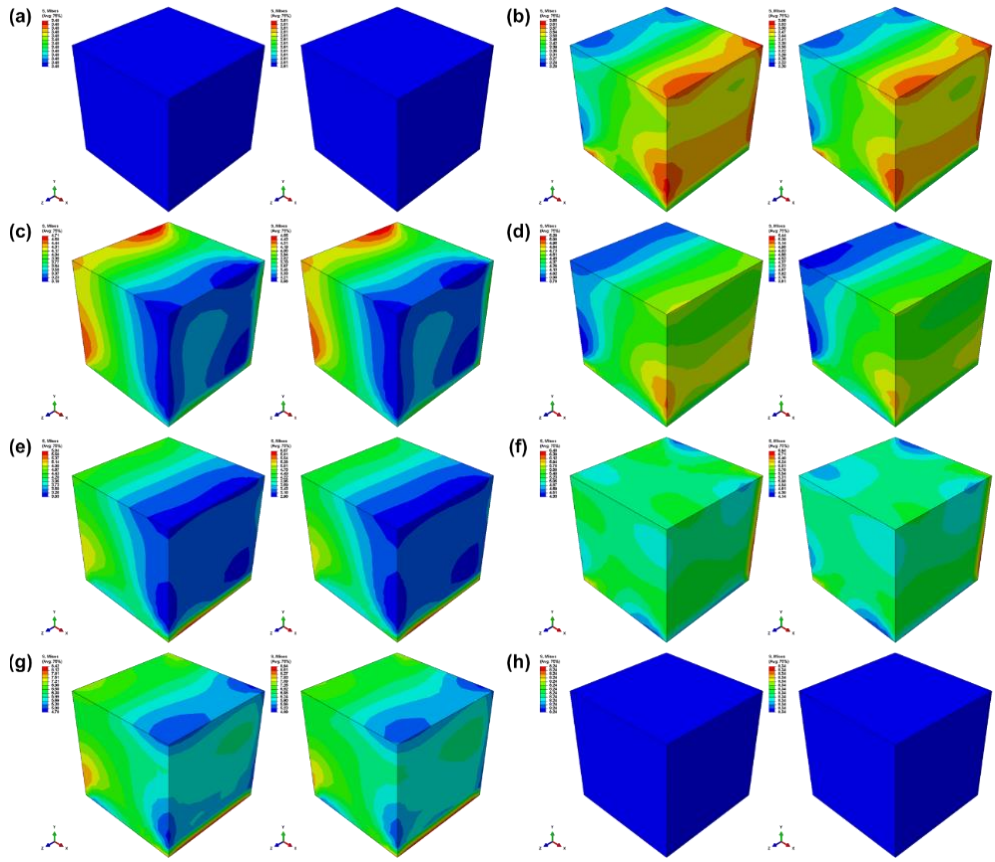

Figure 3-14 Comparison of von Mises stress distribution obtained by UMAT (right) and DIGIMAT (left); the orientation tensor information is consistent with **Figure 3-13**

3.4.3.2. Comparison of UMAT results with tensile test results

The UMAT was validated by comparing its results with experimental ones. First, the tensile test results of PP-GF30-0D were obtained. Next, the orientation tensor of the tensile specimen was obtained by performing injection molding simulation with MOLDEX3D software. Finally, the tensile test procedure was re-simulated using UMAT, and was compared with experimental results.

Four experimental tensile stress–strain curves among the five specimens are presented in **Figure 3-15**. The experimental elastic tensile modulus of PP-GF30-0D was determined to be 6.97 ± 0.44 GPa by the linear regression slope in the tensile strain interval, [0.05 %, 0.25 %].

The injection molding of a PP-GF30 plate in **Figure 3-4(b)** was simulated using MOLDEX3D to obtain the internal microstructural information, which is necessary for re-simulating the tensile test procedure. iARD-RPR model developed by Tseng et al. [149, 150] was used as a fiber orientation model. All the material properties including the shear rate-viscosity curve, PVT diagram, crystallinity, specific heat, thermal conductivity, etc. were referred to Thermylene® P6-30FM-Y249B (Asahi Kasei Corp., Tokyo, Japan) in MOLDEX3D material database, which has similar properties to our constituents. The sprue gate with upper diameter of 5 mm and lower diameter of 8 mm was used. The simulation geometry and result are shown in **Figure 3-16(a)**. 15 probes were chosen and the first orientation components (a_{11}) were extracted along the through-thickness

direction in each probe (see **Figure 3-16(b)**). Two skin layers with preferential orientation to the flow direction and a core layer with orientation perpendicular to the flow direction were investigated as in previous studies [151, 152]. The orientation of the skin layer was consistent in all probes. In the core layer, however, the value of a_{11} varied from 0.66 to 0.76. This is because the side edges of the plate also act as a cooling source, causing slower cooling rate and lower shearing [153]. For this reason, the tensile test results may vary depending on where the tensile specimen was cut from the plate, which can explain the significant standard deviation of the experimental tensile modulus in **Figure 3-15**.

The re-simulation of tensile test was performed. The orientation tensor from MOLDEX3D simulation (donor mesh) was mapped to 5 tensile specimens' geometries in ABAQUS (receiving mesh) using DIGIMAT-MAP module. These procedures are summarized in **Figure 3-17**. Note that C3D8 element was used, and finer mesh was used in thickness direction. The elastic stiffness tensor of each element was calculated by UMAT using the material properties in **Table 3-1** and mapped orientation tensor. An encastre boundary condition and displacement boundary condition of 1.092 mm (corresponding to 1% strain) was applied to the left and right side of the grip regions, respectively.

The re-simulation results are presented in **Figure 3-18**. The tensile stress was extracted from the center of the specimens and averaged as shown in **Figure 3-18(a)**. The comparison between average experimental and UMAT

re-simulation stress–strain curves are shown in **Figure 3-18(b)**. The elastic tensile modulus was determined to be 6.62 ± 0.08 GPa by UMAT (recall experimental tensile modulus of 6.97 ± 0.44 GPa). The proposed UMAT was confirmed to predict the elastic behavior of SFRP with high accuracy (3.68 % error) with low computation time (less than 6 s per specimen), thus demonstrating that the application of a series–parallel ANN system for UMAT simulation is a valid strategy. However, as the tensile strain increases, the increase in difference is inevitable owing to the viscoelastic–viscoplastic nature of the PP matrix. To overcome such discrepancies, the homogenization scheme proposed in this study will be expanded to include the viscoelastic–viscoplastic behavior of matrix in the future study.

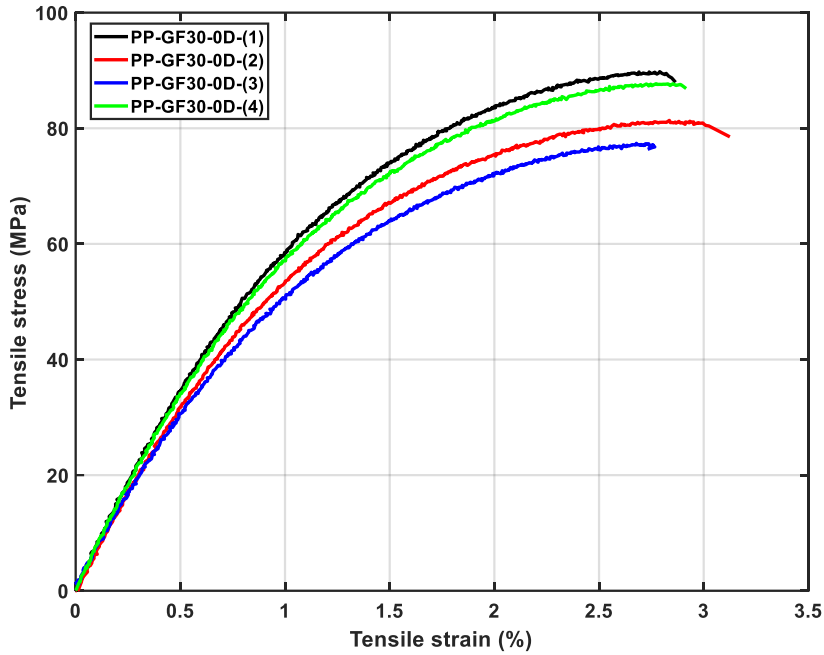

Figure 3-15 Four experimental tensile stress–strain curves of PP-GF30-0D

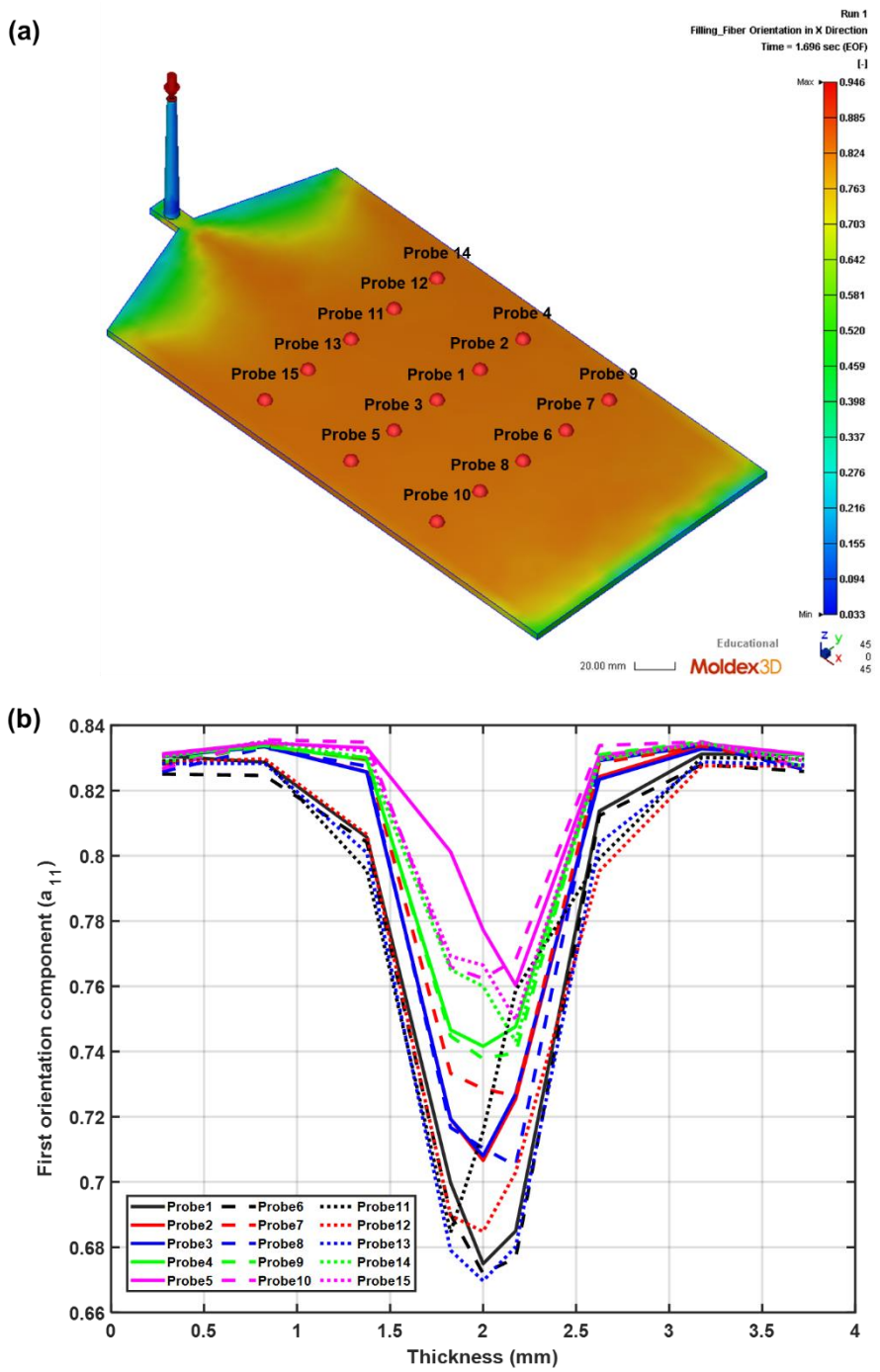

Figure 3-16 (a) Injection molding simulation geometry and result. (b) Distribution of the first orientation components (a_{11}) along through-thickness direction

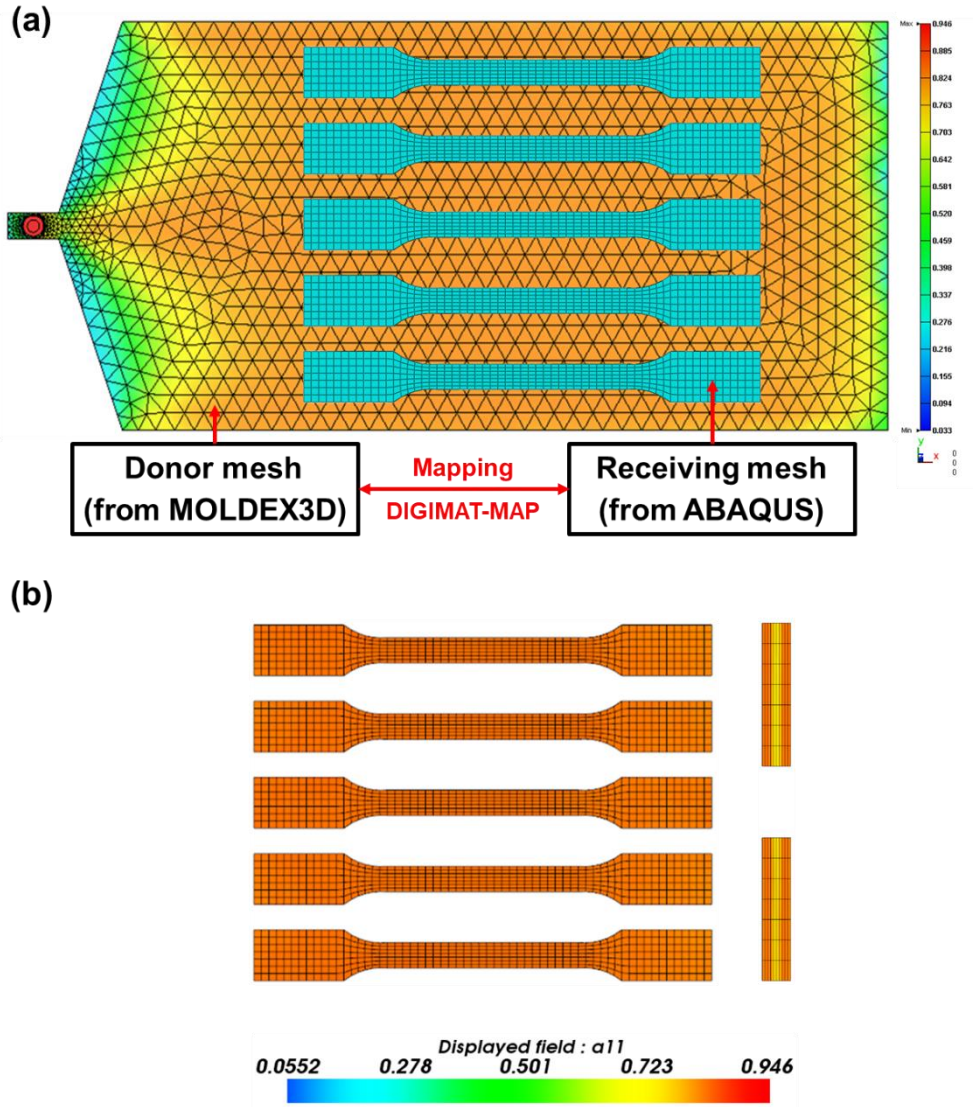

Figure 3-17 (a) Schematic diagram of orientation tensor mapping procedure, and (b) mapping result

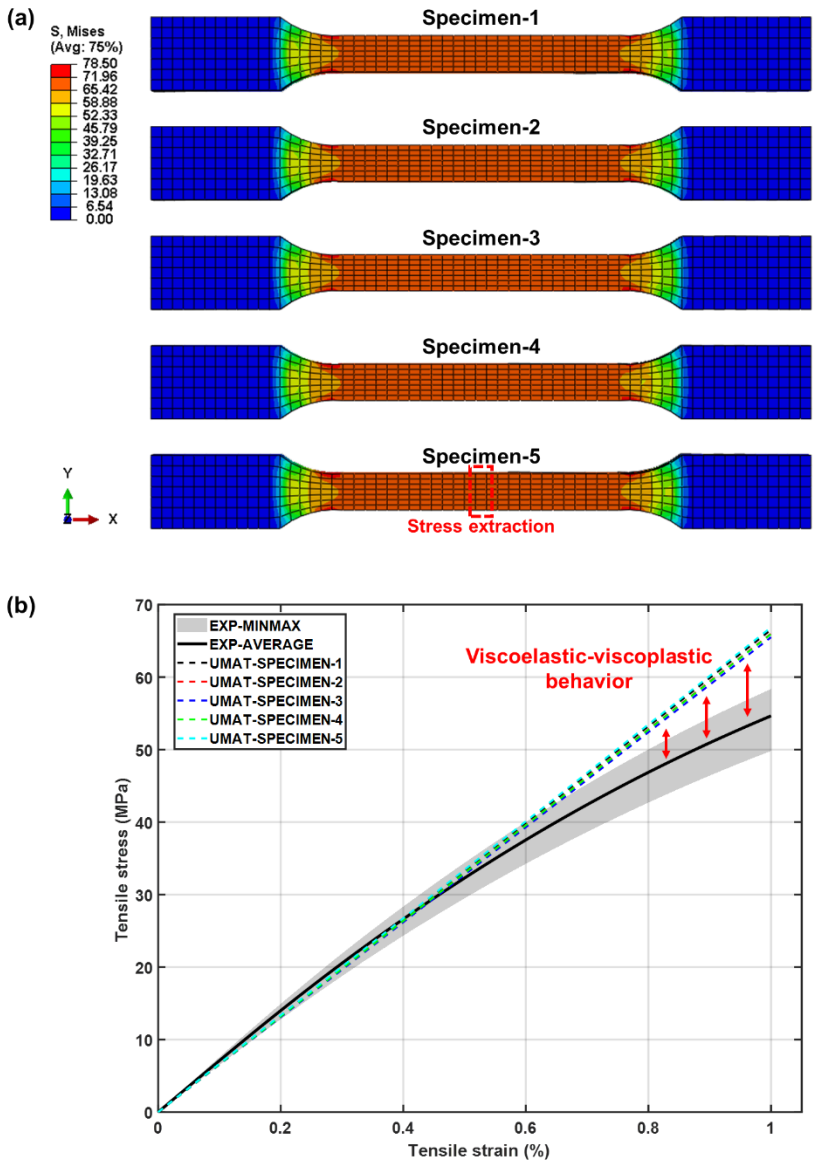

Figure 3-18 (a) Five von Mises stress distribution, and (b) comparison between average experimental and UMAT re-simulation stress–strain curves

3.5. Summary

In this chapter, a machine learning-assisted two-step homogenization framework of SFRPs was proposed. ME reconstruction model and weighted k-means clustering algorithm were used to construct 12 pseudograins with effective orientations and volume fractions for a given arbitrary orientation tensor. However, this methodology was computationally intensive and unsuitable for implementation in user material subroutine of commercial finite element analysis software because both models are based on the iterative optimization procedures. A series–parallel ANN system was constructed and trained with pre-calculated input and output data to overcome the limitation. The series–parallel ANN system, Mori–Tanaka model, and Voigt model were implemented into ABAQUS UMAT subroutine to form a two-step homogenization framework. The predicted elastic modulus values using UMAT exhibited good performance within 3.68 % error compared with experimental values. The total time required for specimen-level UMAT simulation was less than 10 s in a workstation with Intel(R) Core(TM) i7-10700K CPU @ 3.80 GHz (8 cores) and 16GB RAM, thus demonstrating that our machine learning-assisted homogenization framework is highly suitable for implementation into UMAT subroutine.

Chapter 4. Machine learning-assisted thermomechanical homogenization framework considering size effect of inclusion

4.1. Research background

In general, FRPs are excellent in terms of mechanical properties, but has the weaknesses of low electrical and thermal conductivity. However, the need for multifunctionality as well as mechanical property is also growing as it is increasingly used in various industrial fields. For example, high electrical conductivity to deal with lightning strike and high thermal conductivity to deal with ice accumulation in aerospace engineering [154] (see **Figure 4-1** [4]). Therefore, recent trend in the field of FRPs focuses on the development of so called smart FRPs or multifunctional FRPs, which are combination of traditional FRPs (comprised of a polymer matrix and reinforcing fibers) with functional materials (such as metal alloys, and carbon nanomaterials) to achieve enhanced material properties including mechanical, thermal, or electrical properties.

Among various functional materials, carbon-based nanomaterials such as carbon nanotube (CNT) and graphene is determined to be most promising thanks to their outstanding mechanical, thermal, and electrical properties [155]. CNT or graphene are introduced into FRPs either via matrix modification (i.e., dispersion into matrix) or reinforcement modification (i.e.,

grafting on reinforcing fibers). Schematic illustration of these is provided by Islam et al. in **Figure 4-2** [4].

Imran et al. introduced 1.0 % of graphene nanoplatelets (GNPs) into epoxy resin and fabricated GNP-carbon fiber (CF)-epoxy composite by hand lay-up followed by vacuum bagging and compression molding [156]. The electrical conductivity of GNP-CF/epoxy composite was increased by 1.31×10^{-3} S m^{-1} (+132%) compared to the normal CF/epoxy composite. Wang et al. introduced reduced graphene oxide (rGO) into epoxy resin and fabricated rGO-CF/epoxy composite by percolating-assisted resin film infusion (RFI) method [157]. The electrical conductivity of rGO-CF/epoxy composite was increased by 4.40 S m^{-1} compared to the normal CF/epoxy composite.

Diez-Pascual et al. introduced 1.0 % of single-walled CNT (SWCNT) into Polyether ether ketone (PEEK) thermoplastic resin and fabricated SWCNT-glass fiber (GF)-PEEK composite by hot press method [158]. The thermal conductivity of SWCNT-GF/PEEK composite was increased by 0.34 W m^{-1} K^{-1} (+53%) compared to the normal GF-PEEK composite. Kandare et al. introduced 1.0 % of GNP into epoxy resin and fabricated GNP-CF/epoxy composite by wet lay-up method [159]. The thermal conductivity of GNP-CF/epoxy was increased by 0.42 W m^{-1} K^{-1} (+9%) compared to the normal CF/epoxy composite.

Kamaraj et al. introduced 0.1 % of GNP into epoxy resin and fabricated GNP-Flax/epoxy composite by vacuum-assisted resin infusion (VARI)

method [160]. The tensile strength of GNP-Flax/epoxy composite was increased by 61%. Wang et al. introduced 0.5 % of multi-walled CNT (MWCNT) into epoxy resin and fabricated MWCNT-Flax/epoxy composite by hand lay-up method [161]. The tensile strength and modulus were increased by 31.8 % and 12.1 %, respectively.

In this chapter, we will expand the machine learning-assisted mechanical homogenization framework developed in **Chapter 3** to solve thermo-mechanical homogenization problem for smart FRPs with carbon-based nanofillers. First, the concept of the third phase called “interphase” with constant thickness will be introduced to describe the size effect during homogenization. Next, the proposed thermomechanical homogenization models will be studied. Finally, thermomechanical homogenization models considering matrix, fiber, and interphase will be implemented into MATLAB. The validity of this work will be confirmed by comparing experimental or simulation results provided by another research.

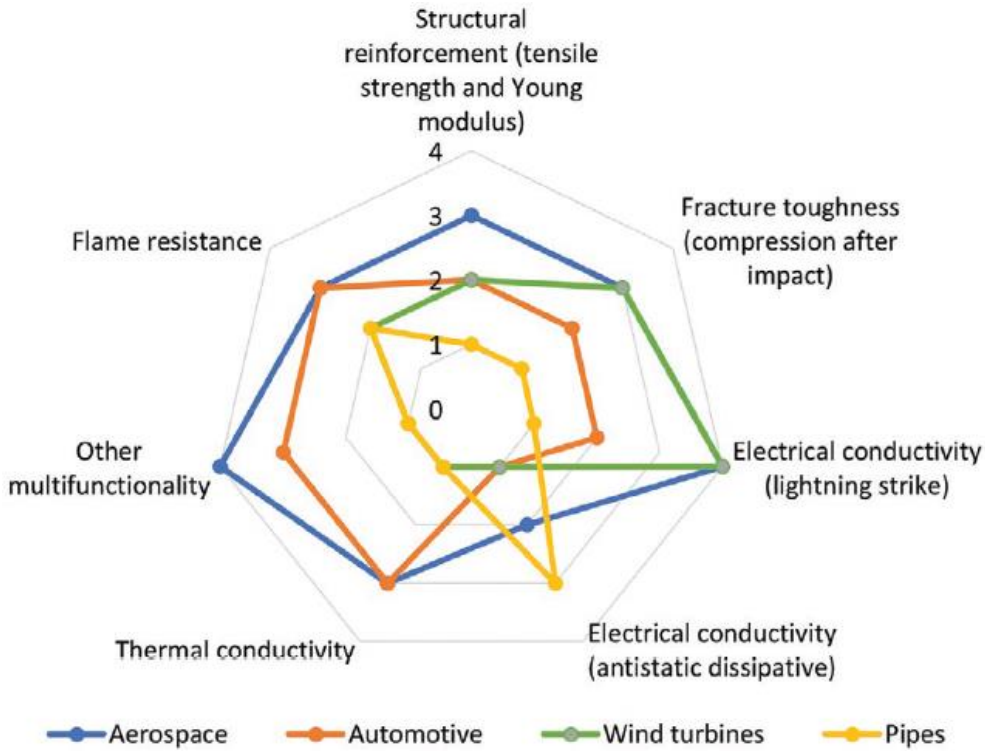

Figure 4-1 A chart comparing smart FRPs performance for various industrial applications [4]

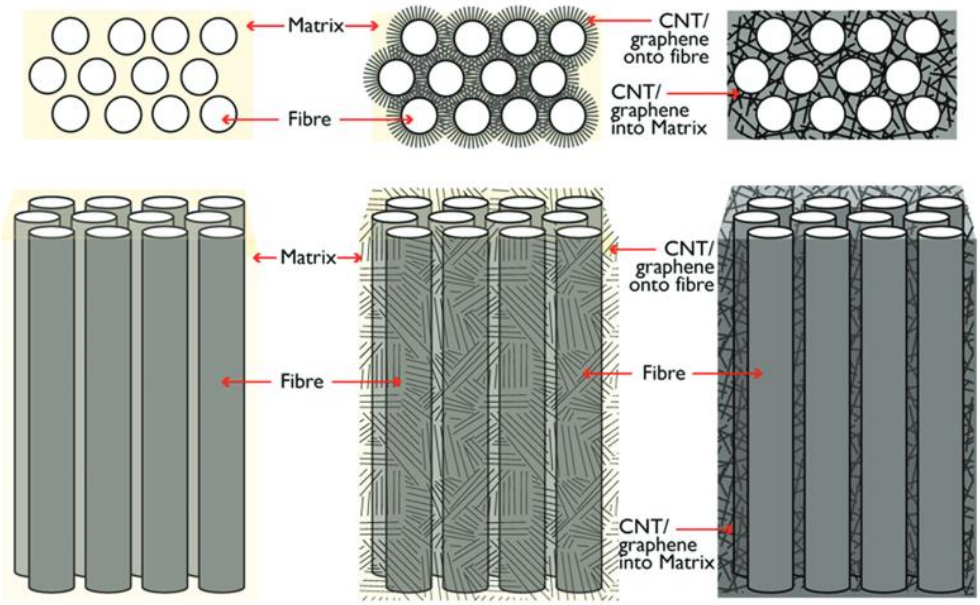

Figure 4-2 Schematic illustration of fabrication techniques of conventional FRP composites and CNT/graphene-based FRP composites using reinforcement modification (chemical grafting) or resin modification (resin mixed) [4]

4.2. Limitation of conventional homogenization scheme

As mentioned in **Section 4.1.**, many experimental achievements of incorporating carbon-based nanofillers into polymeric matrix for enhancement of mechanical, thermal, or electrical properties. However, design of such smart FRPs has not been actively conducted due to the following two reasons.

First, conventional homogenization methodologies do not consider the effect of inclusion size. Experimental works revealed that the size of the inclusion clearly affects not only elastic property but also other material properties such as thermal conductivity or electrical conductivity [162, 163]. However, Eshelby's original formulation is based on classical elasticity, and the resulting Eshelby tensor for an ellipsoidal inclusion depends only on Poisson's ratio of the matrix and the aspect ratio of the inclusion (see **Section 1.3.3.**). Consequently, homogenization methods developed using classical elasticity-based Eshelby tensors cannot account for the inclusion size effect on the elastic properties.

Second, there has not been general methodology to consider orientations of nanofillers and reinforcing fibers timely. Most of the homogenization studies regarding the hybridized FRPs was limited to isotropic spherical particles to avoid consideration of orientation of nanofillers. Recently, to account for the orientation information of nanofillers, related studies generated a representative volume element (RVE) with all the geometrical

information implemented [11, 164] (sufficient inclusions embedded in the matrix to describe given orientation distribution function) or adopted a simple numerical orientation averaging method [13].

4.3. A new homogenization approach considering interphase

4.3.1. The concept of interphase

We will consider a concept of the third phase called “interphase” between polymeric matrix and reinforcing fibers [9, 165-167] to enable homogenization scheme to take the effect of size inclusion into account.

The interphase properties differ from the matrix properties even though it is basically a part of the matrix phase. This is because the matrix atoms in the vicinity of reinforcing atoms are in different chemical situation due to the non-bonding interaction (i.e., van der Waals interaction) between them (see **Figure 4-3**). The interphase properties can be either stiffer or weaker compared to the original matrix phase. If the effect of van der Waals non-bonding interactions between the inclusion atoms and the matrix atoms are dominant, a stiffer interphase is defined (e.g., SiC particles in epoxy matrix [9]). On the other hand, a weak interphase is defined if the inclusion acts as a defect rather than reinforcing material (glass fiber in epoxy matrix [10]).

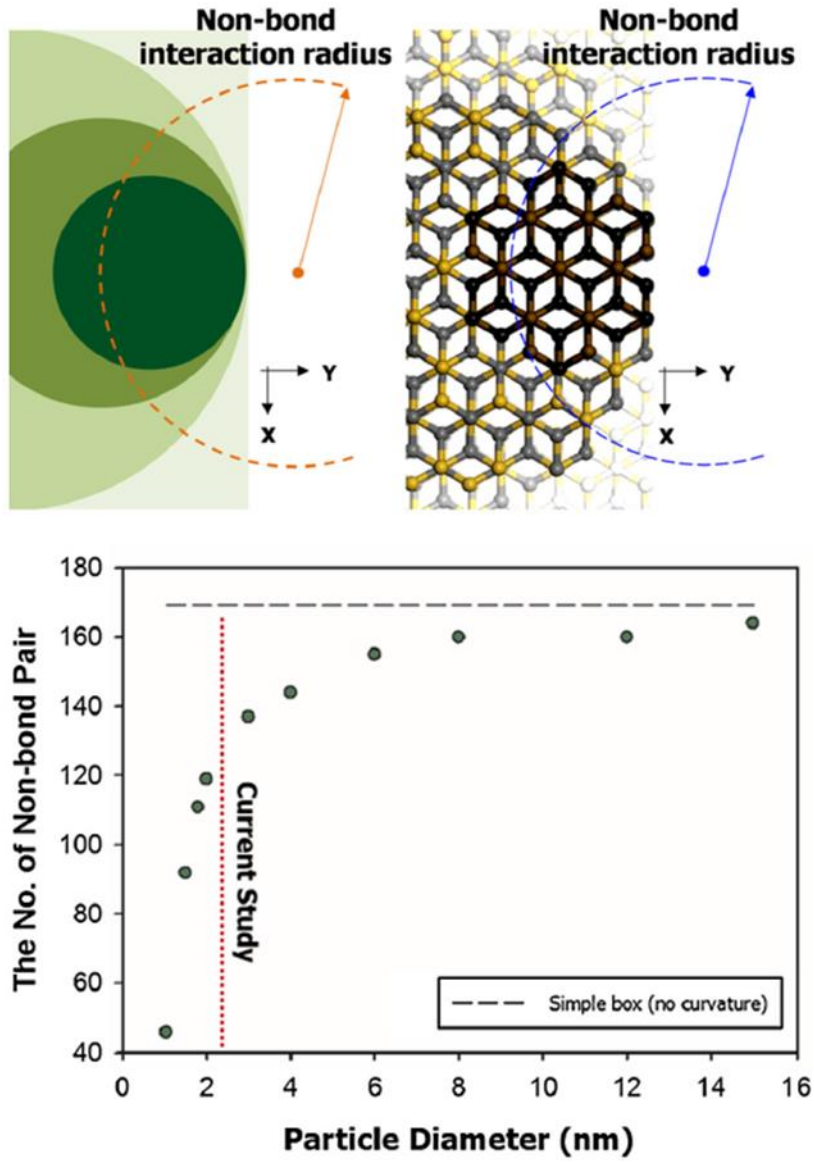

Figure 4-3 Relation between the nanoparticle curvature and the effective number of non-bond pairs [9]

4.3.2. Characterization of the interphase properties

There are three major approaches to characterize the interphase properties (including stiffness tensor, thermal conductivity, or thickness): 1) Experimental, 2) Molecular Dynamics (MD) simulation, or 3) Assumption.

The first approach is to characterize the interphase properties experimentally by directly observing it using Atomic Force Microscope (AFM). AFM is a type of scanning probe microscopy with resolution of a nanometer. The information of a material surface is gathered using a mechanical probe with piezoelectric elements. Riaño et al. cut the unidirectional glass fiber-reinforced epoxy composite perpendicular to the fiber, and observed the elastic modulus at the vicinity of a fiber using AFM (**Figure 4-4** [10]). The interphase thickness was determined to be 200 nm whereas the diameter of the fiber was 15 μm, and the interphase elastic modulus was determined to be 1.7 GPa. Bhuiyan et al. fabricated CNT/PP composite by injection molding and determined the thickness and modulus of CNT/PP interphase using AFM (see **Figure 4-5** [11]). The interphase thickness was determined to be 20 nm whereas the diameter of the CNT was 25 nm, and the interphase elastic modulus was determined to be 0.7 GPa. In both cases, the interphase in each of the material system can be categorized into weak interphase, since Young's modulus of matrix was stiffer than the interphase.

The second approach is to characterize the interphase properties theoretically by MD simulations, FE simulations, or a combination of both.

Choi et al. proposed a model to design the elastic mechanical properties for particulate polymer nanocomposites, which involves matching the analysis results of MD and FE simulations [9]. Strong non-bonding interaction between nanoparticle surface and polymer segments significantly affects the properties of overall composites due to massive surface-to-volume ratio. The curvature effect is rapidly diminished after the particle diameter becomes larger than 10 nm, although the system still has nano-reinforcement features. The key conclusion of their work is that one can apply the saturated interphase thickness and its mechanical properties under a given volume fraction with sufficiently large particle diameter (see **Figure 4-3**). Another study characterized effective interfacial thermal conductivities containing three different CNTs by non-equilibrium molecular dynamics (NEMD) simulation (see **Figure 4-6** [12]).

The last approach is to find the optimum interphase properties by means of curve fitting, which give reasonable match between experimental results when the interphase is considered.

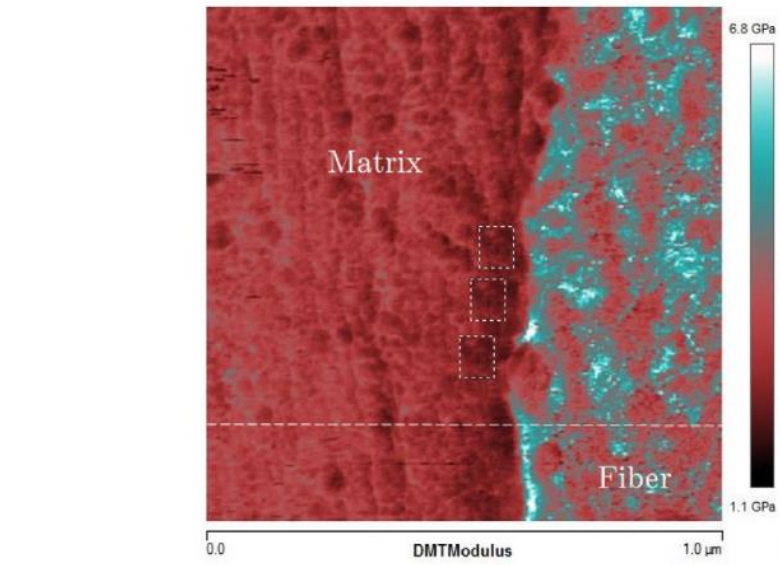

(a) Local modulus measurements.

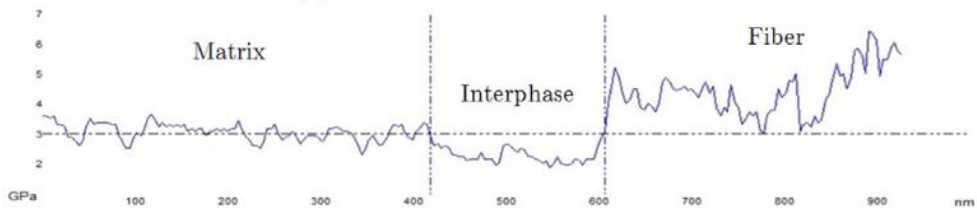

(b) Evolution of Young's modulus.

Figure 4-4 Elastic modulus observation of unidirectional glass fiber-reinforced epoxy composite using AFM [10]

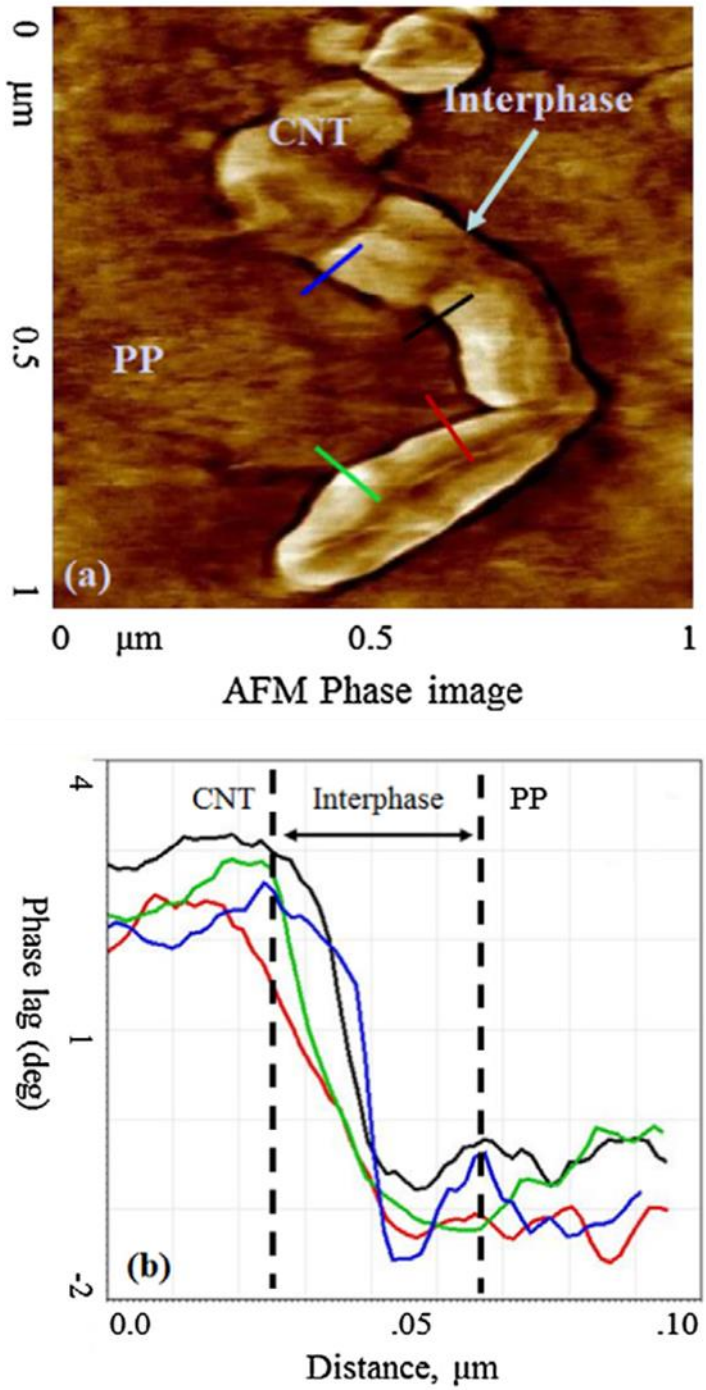

Figure 4-5 AFM phase image and property gradient profile used to determine the thickness and modulus of CNT/PP interphase [11]

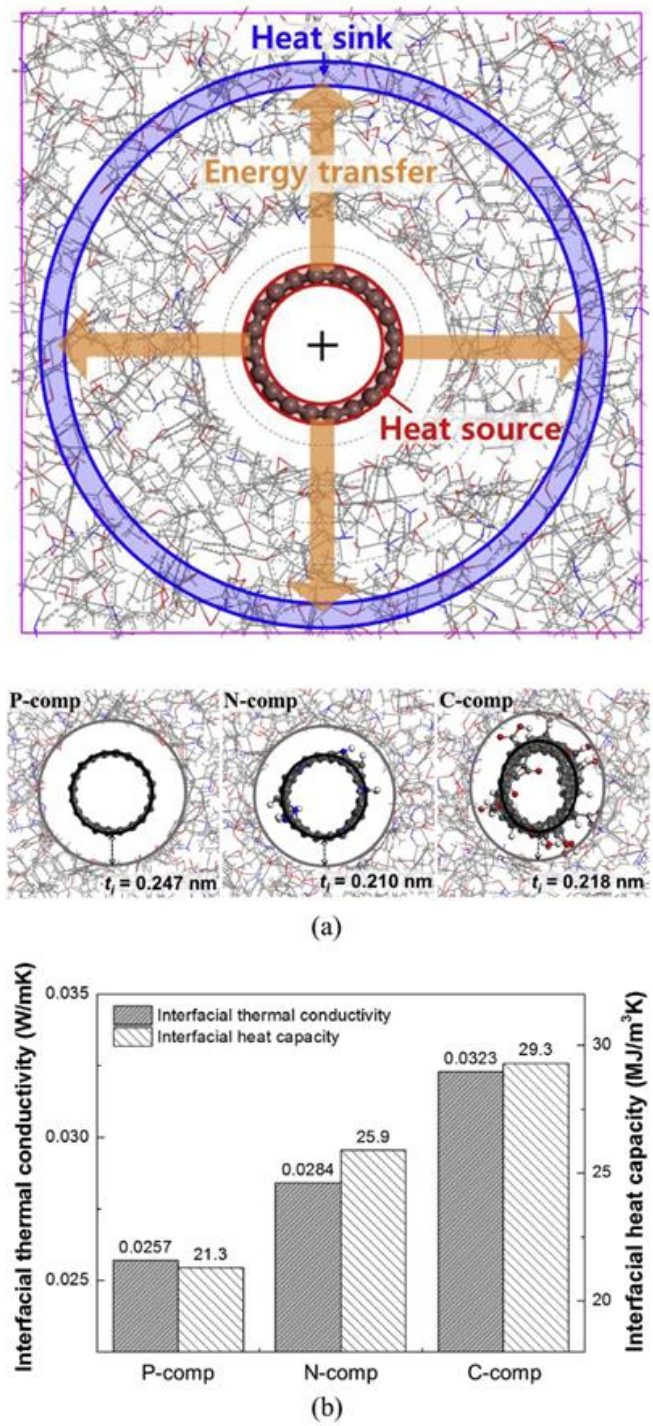

Figure 4-6 Concept of NEMD simulation for radial thermal conduction in nanocomposites and its interphase, and interphase characteristics of three different nanocomposites [12]

4.3.3. Expected outcomes

Based on the conclusion of the studies discussed in the previous **Section 4.3.2.**, we will assume that both reinforcing fibers with microscale and carbon-based nanofillers with nanoscale have constant (i.e., saturated) interphase properties. Note that thermomechanical properties of interphase can be either stiffer or weak, and the thickness of the interphase is nm scale (non-bonding interaction in nanoscale).

To understand the expected effect of the consideration of interphase during homogenization, assume a two-dimensional RVE comprised of three-phase (matrix, inclusion, and interphase) with the length of 5.

First, let us define the radius of a microscale inclusion as 1, the thickness of interphase as 0.05. In this case, the radius-to-thickness ratio is 20. The schematic illustration of this system is shown in **Figure 4-7**. Then, the area fraction of inclusion is equal to 12.57 %, whereas the area fraction of interphase is 1.29 %. As a next step, divide an inclusion into four identical inclusions with radius of 0.5, and the thickness of the interphase remains the same as 0.05. In this case, the radius-to-thickness ratio is 10. Then, the area fraction of inclusion remains the same as 12.57 %, whereas the area fraction of interphase is increased to 2.64 % (+104 %). Although the area fraction of interphase increased more than twice, the effect of interphase during homogenization is negligible because the absolute amount is very small.

Next, let us define the radius of a nanoscale inclusion as 1, the thickness of interphase as 0.25. In this case, the radius-to-thickness ratio is 4 (recall the

radius-to-thickness ratio of 20 in case of microscale inclusion). The schematic illustration of this system is shown in **Figure 4-8**. Then, the area fraction of inclusion is equal to 12.57 %, whereas the area fraction of interphase is 7.07 %. As a next step, divide an inclusion into four identical inclusions with radius of 0.5, and the thickness of the interphase remains the same as 0.25. In this case, the radius-to-thickness ratio is 2. Then, the area fraction of inclusion remains the same as 12.57 %, whereas the area fraction of interphase is increased to 15.71 % (+122 %). The area fraction of interphase increased more than twice, and the effect of interphase during homogenization is not negligible since its absolute amount is bigger than the inclusion.

As a result, we can say that introduction of an interphase with constant thickness to a material system enable us to take the size effect of inclusion into account.

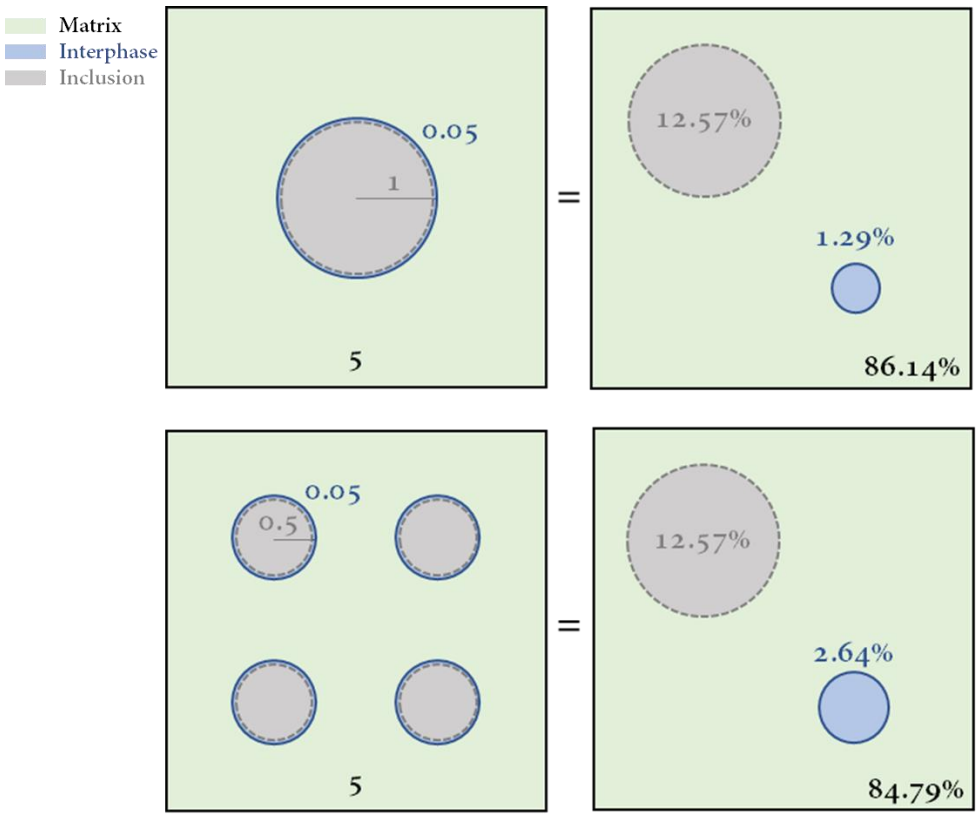

Figure 4-7 The effect of interphase on homogenization of microscale inclusions

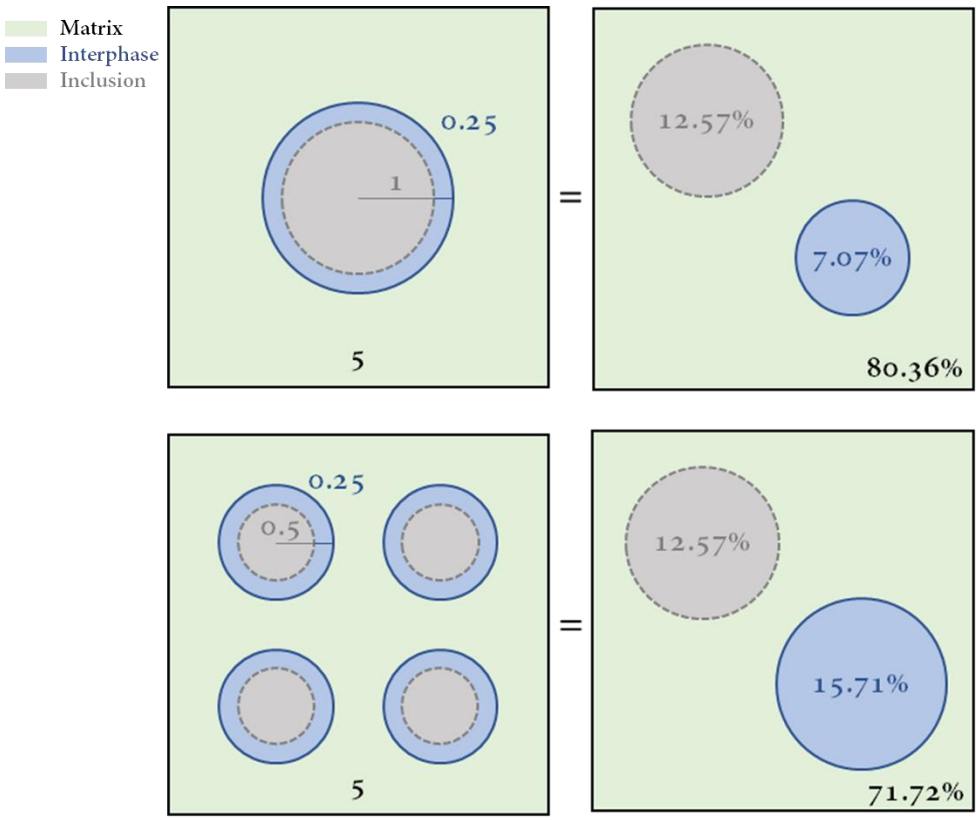

Figure 4-8 The effect of interphase on homogenization of nanoscale inclusions

4.4. Thermal homogenization models

In this chapter, two representative thermomechanical homogenization models to calculate the effective thermal conductivity (ETC) tensor (k) of SFRPs, which are reformulated by Mokarizadehhaghighishirazi et al. [13], will be presented.

Among those two models, the reformulation of Mori-Tanaka model for thermomechanical homogenization will be used in this chapter.

4.4.1. Reformulation of Giordano's model

The first model is the reformulation of Giordano's model [168], which was originally developed for calculation of effective electric permittivity of pseudo-oriented inclusions (**Equation 4-1** and **Equation 4-2**).

$$1-V_f=\frac{k_f-k_{11}}{k_f-k_m}\left(\frac{k_m}{k_{11}}\right)^{\frac{A}{E}}\left[\frac{Fk_m+Ek_f}{Fk_{zz}+Ek_f}\right]^{\frac{G}{EF}}$$

$$A=3L(1-2L)$$

$$E=2-3L-2S+6SL$$

$$F=1+3L+2S-6SL$$

$$G=2(1-3L)^2(2S+1)(1-S)$$

Equation 4-1

$$1-V_f=\frac{k_f-k_{33}}{k_f-k_m}\left(\frac{k_m}{k_{33}}\right)^{\frac{A}{B}}\left[\frac{Ck_m+Bk_f}{Ck_{zz}+Bk_f}\right]^{\frac{D}{BC}}$$

$$A=3L(1-2L)$$

$$B=2-3L+S-3SL$$

$$C=1+3L-S+3SL$$

$$D=(1-3L)^2(2+S)(1-S)$$

Equation 4-2

where V_f is the fiber volume fraction, k_f and k_m are the thermal conductivity of fiber and matrix, respectively. L is the depolarization factor defined with the fiber aspect ratio (a_r) as follows.

$$L=\frac{a_r}{4\left(a_r^2-1\right)^{3/2}}\left[2a_r\sqrt{a_r^2-1}+\ln\frac{a_r-\sqrt{a_r^2-1}}{a_r+\sqrt{a_r^2-1}}\right]$$

Equation 4-3

S is the orientational factor, which can be calculated by the following **Equation 4-4**.

$$S=\left(3a_{11}-1\right)/2=1-3a_{22}=1-3a_{33}$$

Equation 4-4

Typical examples of the orientation factor S are: $S=1$ when all fibers are aligned in x-direction, and $S=0$ when all fibers are perfectly randomly

oriented. Since the decomposed pseudograins are unidirectional (see **Section 3.2.3.**), $S=1$ can be applied. Therefore, **Equation 4-1** and **Equation 4-2** are simplified as follows.

$$1-V_f=\frac{k_f-k_{11}}{k_f-k_m}\left(\frac{k_m}{k_{11}}\right)^{\frac{A}{E}}$$

$$A=3L(1-2L)$$

$$E=3L$$

Equation 4-5

$$1-V_f=\frac{k_f-k_{33}}{k_f-k_m}\left(\frac{k_m}{k_{33}}\right)^{\frac{A}{B}}$$

$$A=3L(1-2L)$$

$$B=3-6L$$

Equation 4-6

In this model, the ETC tensor (k) of the composite is assumed to be transversely isotropic as follows.

$$k=\begin{bmatrix} k_{11} & 0 & 0 \\ 0 & k_{33} & 0 \\ 0 & 0 & k_{33} \end{bmatrix}$$

Equation 4-7

4.4.2. Reformulation of Mori-Tanaka model

Recall the general formulation of Mori-Tanaka model in **Section 1.3.3**. Mokarizadehhaghighishirazi et al. [13] reformulated to predict ETC of SFRPs,

$$k = k_m + V_f\left(k_f - k_m\right)A_{MT}^{ETC} \qquad \textbf{Equation 4-8}$$

where A_{MT}^{ETC} corresponds to the similar concept as the strain concentration tensor A^{ε} in elasticity, which correlates the average temperature gradient of inclusions with composite.

The following **Equation 4-9** will be used to define A_{MT}^{ETC}, which was proposed by Lielens et al. [169].

$$A_{MT}^{ETC} = \dot{A}\left[\left(1 - V_f\right)I + V_f\dot{A}\right]^{-1} \qquad \textbf{Equation 4-9}$$

Herein, the definition of $\dot{A}$ is as follows.

$$\dot{A} = \left[(1-f)\left(I + Sk_m^{-1}\left(k_f - k_m\right)\right) + f\left(I + Sk_f^{-1}\left(k_m - k_f\right)\right)^{-1}\right]^{-1} \qquad \textbf{Equation 4-10}$$

with interpolating factor $f = \left(V_f + {V_f}^2\right)\big/2$.

S is Eshelby tensor for thermal conductance, which depends on the shape of the inclusions. In case of prolate spheroid inclusion ($a_1 > a_2 = a_3$), S can be calculated as follows (recall **Equation 1-25**).

$$S = \begin{bmatrix} 1 - 2S_{22} & 0 & 0 \\ 0 & S_{22} & 0 \\ 0 & 0 & S_{22} \end{bmatrix} \qquad \textbf{Equation 4-11}$$

$$S_{22} = \frac{{a_3}^2 a_1}{2\left({a_1}^2 - {a_3}^2\right)^{3/2}}\left[\frac{a_1}{a_3}\left(\frac{{a_1}^2}{{a_3}^2} - 1\right)^{1/2} - \cosh^{-1}\left(\frac{a_1}{a_3}\right)\right]$$

4.5. Results and Discussion

4.5.1. Effect of interphase on mechanical homogenization

For mechanical homogenization, machine learning-assisted two-step homogenization framework developed in **Chapter 3** was used. CNT can be represented as a hollow cylinder, but it is known that analytical solution of Eshelby tensor for hollow cylinders is not available yet [170]. Therefore, some simplifications suggested by Yanase et al. were also applied to this chapter: 1) CNT will be treated as a solid cylinder that neglects the hollow nature of CNT, and 2) any possible relative motion between the individual shells or tubes in a MWCNT will not be taken into account [171].

Consider an epoxy matrix reinforced with CNT with a volume fraction of 1.5 % (Guru et al. [2]). CNTs are aligned in one direction. The outer radius (r_o) and inner radius (r_i) of CNT is 0.7125 nm and 0.3725 nm, respectively. As mentioned above, CNT is assumed to be an infinite solid cylindrical shape for convenience in calculation, of which effective modulus ($E_{CNT,eff}$) is defined from the original modulus (E_{CNT}) of hollow cylindrical shape as follows.

$$E_{CNT,eff} = E_{CNT} \cdot \frac{\left({r_o}^2 - {r_i}^2 \right)}{{r_o}^2} \qquad \textbf{Equation 4-12}$$

The interphase thickness (t) is assumed to be 0.17, 0.34, and 0.45 nm, while effective modulus of interphase ($E_{int,eff}$) was calculated similarly from the original modulus (E_{int}) using **Equation 4-12**. The material properties and

geometric characteristics of CNT, epoxy matrix, and CNT/epoxy interphase are summarized in **Table 4-1**. Note that interphase thicknesses of 0.17 nm, 0.34 nm, and 0.45 nm are considered.

The comparison of obtained effective elastic modulus ($E_{11,eff}$) of CNT/epoxy composite by finite element simulation [2] and machine learning-assisted two-step homogenization framework is shown in **Figure 4-9**. Note that the data were obtained and manipulated using MATLAB GRABIT, since the original data were not distinguishable. From **Figure 4-9**, it was confirmed that our machine learning-assisted two-step homogenization scheme has the capability to obtain similar results to finite element simulation when interphase is considered.

Table 4-1 Mechanical properties and geometric characteristics of the constituents of CNT/epoxy composites [2]

Phase	**CNT**	**Epoxy**	**Interphase**
Young's modulus	866.45 GPa	4.06 GPa	40.60 GPa
Poisson's ratio	0.3	0.3	0.3
Outer radius	0.71 nm	-	0.88, 1.05, 1.16 nm
Inner radius	0.37 nm	-	0.71 nm

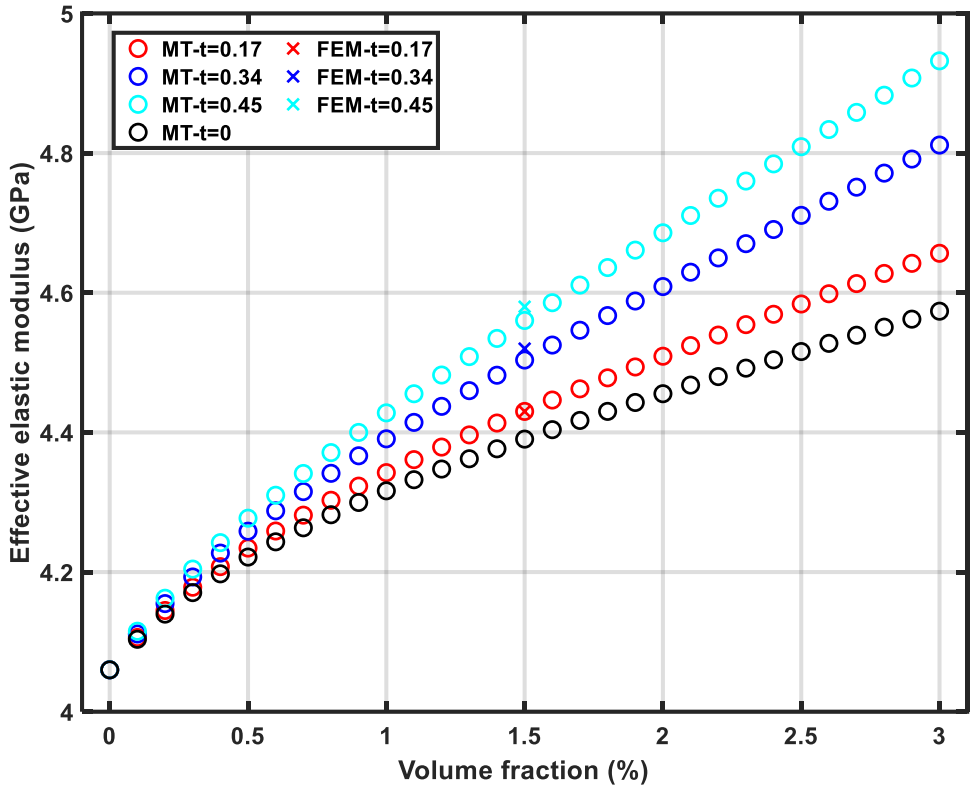

Figure 4-9 Comparison of obtained effective elastic modulus of CNT/epoxy composites considering interphase by FEM [2] and machine learning-assisted two-step homogenization framework

4.5.2. Effect of interphase on thermal homogenization

For thermal homogenization, machine learning-assisted two-step homogenization framework developed in **Chapter 3** was used. Only mechanical-based Mori-Tanaka model was replaced with the reformulated Mori-Tanaka model in **Section 4.4.2**. ODF reconstruction from the given orientation tensor, and pseudograin decomposition procedures were performed.

Consider a PA6 matrix reinforced with short glass fibers with a volume fraction of 10 % (Mokarizadehhaghighishirazi et al. [13]). The length and diameter of an ellipsoidal short glass fiber is 50 μm and 5 μm, respectively. The orientation tensor is [0.33 0.33 0.33]. The isotropic thermal conductivities of matrix and fibers are 72.0 and 32.0 W m^{-1} K^{-1}, respectively. The interphase thickness (t) is assumed to be 0.1 μm, 1.0 μm, 2 μm, and 5 μm, while thermal conductivity of interphase is assumed to be 45.0 W m^{-1} K^{-1}.

The comparison of obtained effective thermal conductivity of short glass fiber-reinforced composite by finite element simulation [13] and machine learning-assisted two-step homogenization framework is shown in **Figure 4-10**. Note that author was not able to find the reference of FEM simulation of thermal homogenization, and therefore only FEM result with zero interphase thickness is given in **Figure 4-10**. From **Figure 4-10**, it was confirmed that our machine learning-assisted two-step homogenization scheme has capability to consider interphase in thermal problem.

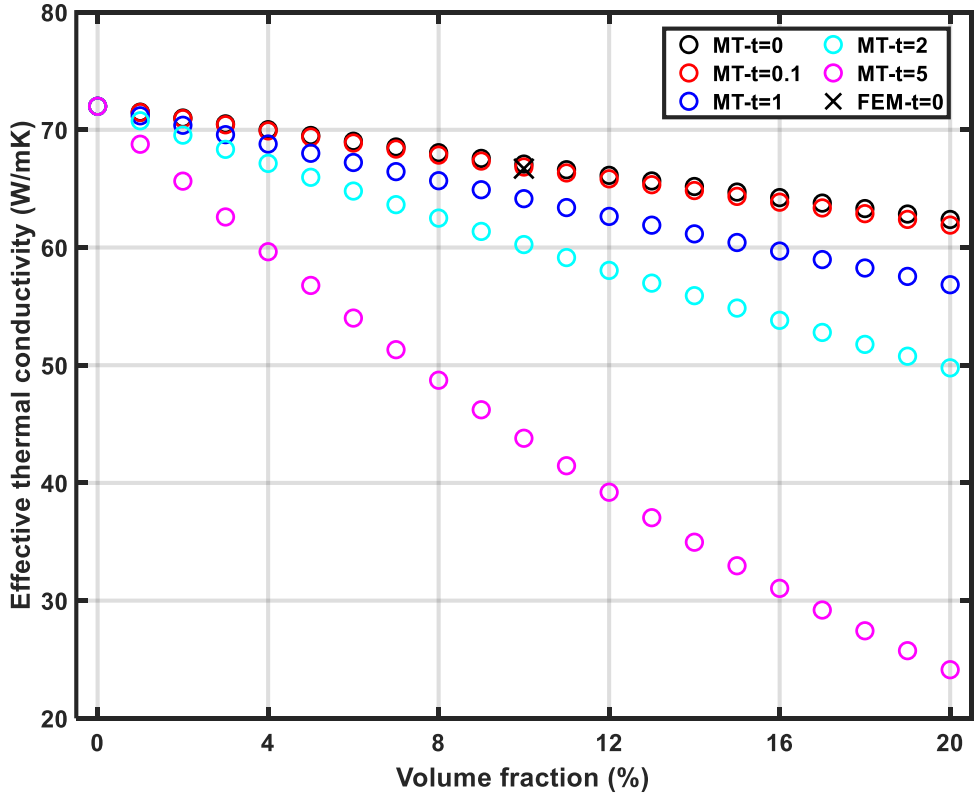

Figure 4-10 Comparison of obtained effective thermal conductivity of injection molded SFRP by FEM [13] and machine learning-assisted two-step homogenization framework

4.6. Summary

Recent trend in the field of FRPs focuses on the development of so called smart FRPs or multifunctional FRPs, which are combination of traditional FRPs (comprised of a polymer matrix and reinforcing fibers) with functional materials (such as metal alloys, and carbon nanomaterials) to achieve enhanced material properties including mechanical, thermal, or electrical properties. In this chapter, proposed machine learning-assisted two-step homogenization scheme in **Chapter 3** was updated to describe the thermomechanical behavior of carbon-based (CNT and graphene) smart FRPs in the following two ways. First, interphase, which is the third phase between inclusion and matrix, was considered. Next, the reformulated Mori-Tanaka model to describe thermal behavior was introduced. With updated machine learning-assisted two-step homogenization scheme, finite element simulation results considering all the microstructures were successfully reproduced with simple homogenization technique, demonstrating the excellence of our work.

Chapter 5. Concluding remarks

In this study, a machine learning-assisted thermomechanical homogenization framework considering the microstructural variation was presented.

In Chapter 2, we applied machine learning strategy to predict stress concentration factor (SCF) of UD FRPs where the constitutive equation is not defined. SCF is the dominant factor to determine the tensile strength of UD fiber-reinforced composites because it can effectively model a progressive contribution of broken fibers to the tensile strength. Nevertheless, an analytical model for calculating the SCF of randomly distributed fibers in UD composites has not been proposed. A machine learning approach was proposed to predict SCF by constructing and training an ANN with extensive finite element analysis results. Then, SCFs could be obtained whenever needed without actual finite element calculation, enabling to develop a novel method for predicting the tensile strength of UD fiber-reinforced composites. A new algorithm for determining the fiber fracture sequence was also developed and combined with the ANN, confirming the applicability of machine learning-assisted modelling strategy of SCF. Overall, the predicted tensile strength showed a good agreement with experiments, however its variability was predicted about 30 MPa, which was four times lower than the variation observed in the experimental tensile strength. For more realistic uncertainty modeling of the tensile strength, other parameters, e.g.,

microstructural randomness such as the variation in fiber diameter or misalignment in the longitudinal direction should be considered in the ANN.

In Chapter 3, we applied machine learning strategy to model orientation distribution function (ODF) reconstruction and pseudograin decomposition procedures of SFRPs, which are based on iterative calculation and therefore very time-consuming. ME reconstruction model and weighted k-means clustering algorithm were used to construct 12 pseudograins with effective orientations and volume fractions for a given arbitrary orientation tensor. However, this methodology was computationally intensive and unsuitable for implementation in user material subroutine of commercial finite element analysis software because both models are based on the iterative optimization procedures. A series–parallel ANN system was constructed and trained with pre-calculated input and output data to overcome the limitation. The series–parallel ANN system, Mori–Tanaka model, and Voigt model were implemented into ABAQUS UMAT subroutine to form a two-step homogenization framework. The predicted elastic modulus values using UMAT exhibited good performance within 3.68 % error compared with experimental values. The total time required for specimen-level UMAT simulation was less than 10 s in a workstation with Intel(R) Core(TM) i7-10700K CPU @ 3.80 GHz (8 cores) and 16GB RAM, thus demonstrating that our machine learning-assisted homogenization framework is highly suitable for implementation into UMAT subroutine.

In Chapter 4, our proposed machine learning-assisted two-step homogenization scheme in Chapter 3 was updated to describe the thermomechanical behavior of carbon-based (CNT and graphene) smart FRPs. Recent trend in the field of FRPs focuses on the development of so called smart FRPs or multifunctional FRPs, which are combination of traditional FRPs (comprised of a polymer matrix and reinforcing fibers) with functional materials (such as metal alloys, and carbon nanomaterials) to achieve enhanced material properties including mechanical, thermal, or electrical properties. The homogenization scheme was updated in the following two ways. First, interphase, which is the third phase between inclusion and matrix, was considered. Next, the reformulated Mori-Tanaka model to describe thermal behavior was introduced. With updated machine learning-assisted two-step homogenization scheme, finite element simulation results considering all the microstructures were successfully reproduced with simple homogenization technique, demonstrating the excellence of our work.

Reference

1. Na, W., et al., *Prediction of the tensile strength of unidirectional carbon fiber composites considering the interfacial shear strength.* Composite Structures, 2017. **168**: p. 92-103.

2. Guru, K., et al., *Effect of interface on the elastic modulus of CNT nanocomposites.* Journal of Nanomechanics and Micromechanics, 2016. **6**(3): p. 04016004.

3. Balasubramanian, M., *Composite materials and processing*. 2014: CRC press Boca Raton.

4. Islam, M.H., et al., *Graphene and CNT-Based Smart Fiber-Reinforced Composites: A Review.* Advanced Functional Materials, 2022. **32**(40): p. 2205723.

5. Ramprasad, R., et al., *Machine learning in materials informatics: recent applications and prospects.* npj Computational Materials, 2017. **3**(1): p. 1-13.

6. Pattnaik, P., et al., *Role of machine learning in the field of Fiber reinforced polymer composites: A preliminary discussion.* Materials Today: Proceedings, 2021. **44**: p. 4703-4708.

7. Gu, G.X., et al., *Bioinspired hierarchical composite design using machine learning: simulation, additive manufacturing, and experiment.* Materials Horizons, 2018. **5**(5): p. 939-945.

8. Vignoli, L.L., et al., *Comparative analysis of micromechanical models for the elastic composite laminae.* Composites Part B: Engineering, 2019. **174**: p. 106961.

9. Choi, J., et al., *The influence of nanoparticle size on the mechanical*

properties of polymer nanocomposites and the associated interphase region: A multiscale approach. Composite Structures, 2015. **119**: p. 365-376.

10. Riaño, L., et al., *Effect of interphase region on the elastic behavior of unidirectional glass-fiber/epoxy composites.* Composite Structures, 2018. **198**: p. 109-116.

11. Bhuiyan, M.A., et al., *Understanding the effect of CNT characteristics on the tensile modulus of CNT reinforced polypropylene using finite element analysis.* Computational Materials Science, 2013. **79**: p. 368-376.

12. Choi, H.K., et al., *Analysis of the influence of interphase characteristics on thermal conduction in surface-modified carbon nanotube-reinforced composites using an analytical model.* Composites Science and Technology, 2018. **168**: p. 145-151.

13. Mokarizadehhaghighishirazi, M., et al., *Homogenisation of the Local Thermal Conductivity in Injection-Moulded Short Fibre Reinforced Composites.* Polymers, 2022. **14**(16): p. 3360.

14. Soutis, C., *Carbon fiber reinforced plastics in aircraft construction.* Materials Science and Engineering: A, 2005. **412**(1-2): p. 171-176.

15. Piancastelli, L., et al., *A comparison between CFRP and 2195-FSW for aircraft structural designs.* International Journal of Heat and Technology, 2013. **31**(1): p. 17-24.

16. Bussadori, B., K. Schuffenhauer, and A. Scattina, *Modelling of CFRP crushing structures in explicit crash analysis.* Composites Part B: Engineering, 2014. **60**: p. 725-735.

17. Kelly, J.C., et al., *Impacts of vehicle weight reduction via material substitution on life-cycle greenhouse gas emissions.* Environmental science & technology, 2015. **49**(20): p. 12535-12542.

18. Fragassa, C., A. Pavlovic, and G. Minak, *On the structural behaviour of a CFRP safety cage in a solar powered electric vehicle.* Composite Structures, 2020. **252**: p. 112698.

19. Grace, N.F., et al., *Design-construction of bridge street bridge-first CFRP bridge in the United States.* PCI journal, 2002. **47**(5).

20. Peng, Y.L.F., *Applications and development of fiber-reinforced polymer in engineering structures [J].* China Civil Engineering Journal, 2006. **3**: p. 39.

21. Miyano, Y., et al., *Accelerated testing for long-term strength of innovative CFRP laminates for marine use.* Composites Part B: Engineering, 2008. **39**(1): p. 5-12.

22. Duflou, J., et al., *Environmental impact analysis of composite use in car manufacturing.* CIRP annals, 2009. **58**(1): p. 9-12.

23. Samuel, A.L., *Some studies in machine learning using the game of checkers.* IBM Journal of research and development, 1959. **3**(3): p. 210-229.

24. Alpaydin, E., *Introduction to Machine Learning, 3rd Editio. ed*. 2014, The MIT Press.

25. El Naqa, I., R. Li, and M.J. Murphy, *Machine learning in radiation oncology: theory and applications*. 2015: Springer.

26. John, M.J. and S. Thomas, *Biofibres and biocomposites.* Carbohydrate polymers, 2008. **71**(3): p. 343-364.

27. Kushvaha, V. and H. Tippur, *Effect of filler shape, volume fraction and loading rate on dynamic fracture behavior of glass-filled epoxy.* Composites Part B: Engineering, 2014. **64**: p. 126-137.

28. Esnaola, A., et al., *Effect of the manufacturing process on the energy absorption capability of GFRP crush structures.* Composite Structures, 2018. **187**: p. 316-324.

29. Afrouzian, A., et al., *Effect of nano-particles on the tensile, flexural and perforation properties of the glass/epoxy composites.* Journal of reinforced plastics and composites, 2017. **36**(12): p. 900-916.

30. Tiryaki, S. and A. Aydın, *An artificial neural network model for predicting compression strength of heat treated woods and comparison with a multiple linear regression model.* Construction and Building Materials, 2014. **62**: p. 102-108.

31. Tapia, G., A. Elwany, and H. Sang, *Prediction of porosity in metal-based additive manufacturing using spatial Gaussian process models.* Additive Manufacturing, 2016. **12**: p. 282-290.

32. Khademi, F., et al., *Multiple linear regression, artificial neural network, and fuzzy logic prediction of 28 days compressive strength of concrete.* Frontiers of Structural and Civil Engineering, 2017. **11**(1): p. 90-99.

33. Gu, G.X., C.-T. Chen, and M.J. Buehler, *De novo composite design based on machine learning algorithm.* Extreme Mechanics Letters, 2018. **18**: p. 19-28.

34. Qi, C., A. Fourie, and Q. Chen, *Neural network and particle swarm optimization for predicting the unconfined compressive strength of cemented paste backfill.* Construction and Building Materials, 2018.

159: p. 473-478.

35. Yang, Z., et al., *Deep learning approaches for mining structure-property linkages in high contrast composites from simulation datasets.* Computational Materials Science, 2018. **151**: p. 278-287.

36. Hanakata, P.Z., et al., *Accelerated search and design of stretchable graphene kirigami using machine learning.* Physical review letters, 2018. **121**(25): p. 255304.

37. Hansoge, N.K., et al., *Materials by design for stiff and tough hairy nanoparticle assemblies.* ACS nano, 2018. **12**(8): p. 7946-7958.

38. Young, B.A., et al., *Can the compressive strength of concrete be estimated from knowledge of the mixture proportions?: New insights from statistical analysis and machine learning methods.* Cement and Concrete Research, 2019. **115**: p. 379-388.

39. Chen, C.-T. and G.X. Gu, *Machine learning for composite materials.* MRS Communications, 2019. **9**(2): p. 556-566.

40. Eshelby, J.D., *The determination of the elastic field of an ellipsoidal inclusion, and related problems.* Proceedings of the royal society of London. Series A. Mathematical and physical sciences, 1957. **241**(1226): p. 376-396.

41. Mori, T. and K. Tanaka, *Average stress in matrix and average elastic energy of materials with misfitting inclusions.* Acta metallurgica, 1973. **21**(5): p. 571-574.

42. Benveniste, Y., *A new approach to the application of Mori-Tanaka's theory in composite materials.* Mechanics of materials, 1987. **6**(2): p. 147-157.

43. Parsaee, A., M. Shokrieh, and M. Mondali, *A micro–macro homogenization scheme for elastic composites containing high volume fraction multi-shape inclusions.* Computational Materials Science, 2016. **121**: p. 217-224.

44. Voigt, W., *Ueber die Beziehung zwischen den beiden Elasticitätsconstanten isotroper Körper.* Annalen der physik, 1889. **274**(12): p. 573-587.

45. Mura, T., *Micromechanics of defects in solids*. 2013: Springer Science & Business Media.

46. Zhu, T.-L., *A reliability-based safety factor for aircraft composite structures.* Computers & Structures, 1993. **48**(4): p. 745-748.

47. Chiachio, M., J. Chiachio, and G. Rus, *Reliability in composites–A selective review and survey of current development.* Composites Part B: Engineering, 2012. **43**(3): p. 902-913.

48. Shiao, M.C., S.N. Singhal, and C.C. Chamis, *A method for the probabilistic design assessment of composite structures.* 1994.

49. Shiao, M.C. and C.C. Chamis, *Probabilistic evaluation of fuselage-type composite structures.* Probabilistic engineering mechanics, 1999. **14**(1-2): p. 179-187.

50. Chamis, C.C., *Probabilistic simulation of multi-scale composite behavior.* Theoretical and applied fracture mechanics, 2004. **41**(1-3): p. 51-61.

51. Matveev, M., A. Long, and I. Jones, *Modelling of textile composites with fibre strength variability.* Composites science and technology, 2014. **105**: p. 44-50.

52. Frantziskonis, G.N., *Stochastic modeling of heterogeneous materials–a process for the analysis and evaluation of alternative formulations.* Mechanics of Materials, 1998. **27**(3): p. 165-175.

53. Graham, L. and S. Baxter, *Simulation of local material properties based on moving-window GMC.* Probabilistic Engineering Mechanics, 2001. **16**(4): p. 295-305.

54. Spanos, P. and A. Kontsos, *A multiscale Monte Carlo finite element method for determining mechanical properties of polymer nanocomposites.* Probabilistic Engineering Mechanics, 2008. **23**(4): p. 456-470.

55. Huang, Y., K.K. Jin, and S.K. Ha, *Effects of fiber arrangement on mechanical behavior of unidirectional composites.* Journal of composite materials, 2008. **42**(18): p. 1851-1871.

56. Yushanov, S.P. and A.E. Bogdanovich, *Stochastic theory of composite materials with random waviness of the reinforcements.* International journal of solids and structures, 1998. **35**(22): p. 2901-2930.

57. Jeong, H. and R. Shenoi, *Probabilistic strength analysis of rectangular FRP plates using Monte Carlo simulation.* Computers & Structures, 2000. **76**(1-3): p. 219-235.

58. Onkar, A., C. Upadhyay, and D. Yadav, *Probabilistic failure of laminated composite plates using the stochastic finite element method.* Composite Structures, 2007. **77**(1): p. 79-91.

59. Lekou, D. and T. Philippidis, *Mechanical property variability in FRP laminates and its effect on failure prediction.* Composites Part B: Engineering, 2008. **39**(7-8): p. 1247-1256.

60. Sriramula, S. and M.K. Chryssanthopoulos, *Quantification of uncertainty modelling in stochastic analysis of FRP composites.* Composites Part A: Applied Science and Manufacturing, 2009. **40**(11): p. 1673-1684.

61. Ravandi, M., M. Banu, and M. Noorian, *Uncertainty analysis of mechanical behavior of natural fiber composites.* 2020.

62. Azzi, V. and S. Tsai, *Anisotropic strength of composites.* Experimental mechanics, 1965. **5**(9): p. 283-288.

63. Wu, E.M., *Phenomenological anisotropic failure criterion.* Composite materials, 1974. **2**: p. 353-431.

64. Puck, A. and H. Schürmann, *Failure analysis of FRP laminates by means of physically based phenomenological models*, in *Failure criteria in fibre-reinforced-polymer composites*. 2004, Elsevier. p. 832-876.

65. Zweben, C. and B.W. Rosen, *A statistical theory of material strength with application to composite materials.* Journal of the Mechanics and Physics of Solids, 1970. **18**(3): p. 189-206.

66. Hedgepeth, J.M. and P. Van Dyke, *Local stress concentrations in imperfect filamentary composite materials.* Journal of composite materials, 1967. **1**(3): p. 294-309.

67. Gücer, D. and J. Gurland, *Comparison of the statistics of two fracture modes.* Journal of the Mechanics and Physics of Solids, 1962. **10**(4): p. 365-373.

68. Nairn, J.A., *Fracture mechanics of unidirectional composites using the shear-lag model I: theory.* Journal of composite materials, 1988.

22(6): p. 561-588.

69. Shioya, M., S. Yasui, and A. Takaku, *Relation between interfacial shear strength and tensile strength of carbon fiber/resin composite strands.* Composite interfaces, 1998. **6**(4): p. 305-323.

70. Wright, P., et al., *Ultra high resolution computed tomography of damage in notched carbon fiber—epoxy composites.* Journal of composite materials, 2008. **42**(19): p. 1993-2002.

71. Na, W., D. Kwon, and W.-R. Yu, *X-ray computed tomography observation of multiple fiber fracture in unidirectional CFRP under tensile loading.* Composite Structures, 2018. **188**: p. 39-47.

72. Iizuka, K., et al., *Development of a three-dimensional finite element model for a unidirectional carbon fiber reinforced plastic based on X-ray computed tomography images and the numerical simulation on compression.* Advanced Composite Materials, 2019. **28**(1): p. 73-85.

73. Mehdikhani, M., et al., *Combining digital image correlation with X-ray computed tomography for characterization of fiber orientation in unidirectional composites.* Composites Part A: Applied Science and Manufacturing, 2020: p. 106234.

74. Daniels, H.E., *The statistical theory of the strength of bundles of threads. I.* Proceedings of the Royal Society of London. Series A. Mathematical and Physical Sciences, 1945. **183**(995): p. 405-435.

75. Coleman, B., *On the strength of classical fibres and fibre bundles.* Journal of the Mechanics and Physics of Solids, 1958. **7**(1): p. 60-70.

76. Hinrichsen, E.L., J. Feder, and T. Jøssang, *Geometry of random sequential adsorption.* Journal of statistical physics, 1986. **44**(5-6): p.

793-827.

77. Vaughan, T. and C. McCarthy, *A combined experimental–numerical approach for generating statistically equivalent fibre distributions for high strength laminated composite materials.* Composites Science and Technology, 2010. **70**(2): p. 291-297.

78. Yang, L., et al., *A new method for generating random fibre distributions for fibre reinforced composites.* Composites Science and Technology, 2013. **76**: p. 14-20.

79. Wang, W., et al., *Micromechanical modeling of fiber-reinforced composites with statistically equivalent random fiber distribution.* Materials, 2016. **9**(8): p. 624.

80. Park, S.-M., et al., *Efficient generator of random fiber distribution with diverse volume fractions by random fiber removal.* Composites Part B: Engineering, 2019. **167**: p. 302-316.

81. Park, S.-M., et al., *Prediction and Calibration of Transverse Mechanical Properties of Unidirectional Composites with Random Fiber Arrangement Considering Interphase Effect.* Composites Research, 2019. **32**(5): p. 270-278.

82. Barzegar, M., J. Costa, and C.S. Lopes, *High-fidelity computational micromechanics of first-fibre failure in unidirectional composites: Deformation mechanisms and stress concentration factors.* International Journal of Solids and Structures, 2020. **204**: p. 18-33.

83. Chen, Y.-Y., et al., *Design and implementation of cloud analytics-assisted smart power meters considering advanced artificial intelligence as edge analytics in demand-side management for smart homes.* Sensors, 2019. **19**(9): p. 2047.

84. Vassilopoulos, A.P., E.F. Georgopoulos, and V. Dionysopoulos, *Artificial neural networks in spectrum fatigue life prediction of composite materials.* International Journal of Fatigue, 2007. **29**(1): p. 20-29.

85. da Silva, A.M.L., et al., *Composite reliability assessment based on Monte Carlo simulation and artificial neural networks.* IEEE Transactions on Power Systems, 2007. **22**(3): p. 1202-1209.

86. Hassan, A.M., et al., *Prediction of density, porosity and hardness in aluminum–copper-based composite materials using artificial neural network.* Journal of materials processing technology, 2009. **209**(2): p. 894-899.

87. De Albuquerque, V.H.C., J.M.R. Tavares, and L.M. Durão, *Evaluation of delamination damage on composite plates using an artificial neural network for the radiographic image analysis.* Journal of Composite Materials, 2010. **44**(9): p. 1139-1159.

88. Dey, S., et al., *Uncertainty quantification in natural frequency of composite plates-An Artificial neural network based approach.* Advanced Composites Letters, 2016. **25**(2): p. 096369351602500203.

89. Kazi, M.-K., F. Eljack, and E. Mahdi, *Optimal filler content for cotton fiber/PP composite based on mechanical properties using artificial neural network.* Composite Structures, 2020. **251**: p. 112654.

90. Liu, X., et al., *A review of artificial neural networks in the constitutive modeling of composite materials.* Composites Part B: Engineering, 2021. **224**: p. 109152.

91. Sharan, A. and M. Mitra, *Prediction of static strength properties of carbon fiber-reinforced composite using artificial neural network.*

Modelling and Simulation in Materials Science and Engineering, 2022. **30**(7): p. 075001.

92. Chakravarty, S., et al., *Deep neural networks based predictive-generative framework with data augmentation for designing composite materials.* Modelling and Simulation in Materials Science and Engineering, 2022. **30**(7): p. 075003.

93. Vujicic, T., et al. *Comparative analysis of methods for determining number of hidden neurons in artificial neural network*. in *Central european conference on information and intelligent systems*. 2016. Faculty of Organization and Informatics Varazdin.

94. Heaton, J., *Introduction to neural networks with Java*. 2008: Heaton Research, Inc.

95. Gruber, G., A. Haimerl, and S. Wartzack, *Consideration of orientation properties of short fiber reinforced polymers within early design steps.* FEA Inf. Eng. J, 2013. **2**: p. 2167-2173.

96. Mortazavian, S. and A. Fatemi, *Fatigue behavior and modeling of short fiber reinforced polymer composites: A literature review.* International Journal of Fatigue, 2015. **70**: p. 297-321.

97. Fu, S.-Y., B. Lauke, and Y.-W. Mai, *Science and engineering of short fibre-reinforced polymer composites*. 2019: Woodhead Publishing.

98. Bernasconi, A., M. Carboni, and R. Ribani, *On the combined use of Digital Image Correlation and Micro Computed Tomography to measure fibre orientation in short fibre reinforced polymers.* Composites Science and Technology, 2020. **195**: p. 108182.

99. Sun, C.-T. and R.S. Vaidya, *Prediction of composite properties from a*

representative volume element. Composites science and Technology, 1996. **56**(2): p. 171-179.

100. Feyel, F., *Multiscale FE2 elastoviscoplastic analysis of composite structures.* Computational Materials Science, 1999. **16**(1-4): p. 344-354.

101. Breuer, K. and M. Stommel, *Prediction of short fiber composite properties by an artificial neural network trained on an rve database.* Fibers, 2021. **9**(2): p. 8.

102. Hill, R., *A self-consistent mechanics of composite materials.* Journal of the Mechanics and Physics of Solids, 1965. **13**(4): p. 213-222.

103. Nemat-Nasser, S. and M. Hori, *Micromechanics: overall properties of heterogeneous materials*. 2013: Elsevier.

104. McLaughlin, R., *A study of the differential scheme for composite materials.* International Journal of Engineering Science, 1977. **15**(4): p. 237-244.

105. Pierard, O., C. Friebel, and I. Doghri, *Mean-field homogenization of multi-phase thermo-elastic composites: a general framework and its validation.* Composites Science and Technology, 2004. **64**(10-11): p. 1587-1603.

106. Camacho, C.W., et al., *Stiffness and thermal expansion predictions for hybrid short fiber composites.* Polymer Composites, 1990. **11**(4): p. 229-239.

107. Friebel, C., I. Doghri, and V. Legat, *General mean-field homogenization schemes for viscoelastic composites containing multiple phases of coated inclusions.* International journal of solids

and structures, 2006. **43**(9): p. 2513-2541.

108. Kammoun, S., et al., *First pseudo-grain failure model for inelastic composites with misaligned short fibers.* Composites Part A: Applied Science and Manufacturing, 2011. **42**(12): p. 1892-1902.

109. Jain, A., et al., *Pseudo-grain discretization and full Mori Tanaka formulation for random heterogeneous media: Predictive abilities for stresses in individual inclusions and the matrix.* Composites science and technology, 2013. **87**: p. 86-93.

110. Kammoun, S., et al., *Micromechanical modeling of the progressive failure in short glass–fiber reinforced thermoplastics–First Pseudo-Grain Damage model.* Composites part A: applied science and manufacturing, 2015. **73**: p. 166-175.

111. Tian, W., et al., *Numerical evaluation on mechanical properties of short-fiber-reinforced metal matrix composites: Two-step mean-field homogenization procedure.* Composite Structures, 2016. **139**: p. 96-103.

112. Ogierman, W. and G. Kokot, *Homogenization of inelastic composites with misaligned inclusions by using the optimal pseudo-grain discretization.* International Journal of Solids and Structures, 2017. **113**: p. 230-240.

113. Ogierman, W., *A new model for time-efficient analysis of nonlinear composites with arbitrary orientation distribution of fibres.* Composite Structures, 2021. **273**: p. 114310.

114. Reuß, A., *Berechnung der fließgrenze von mischkristallen auf grund der plastizitätsbedingung für einkristalle.* ZAMM-Journal of Applied Mathematics and Mechanics/Zeitschrift für Angewandte Mathematik

und Mechanik, 1929. **9**(1): p. 49-58.

115. Takahara, A., T. Magome, and T. Kajiyama, *Effect of glass fiber-matrix polymer interaction on fatigue characteristics of short glass fiber-reinforced poly (butylene terephthalate) based on dynamic viscoelastic measurement during the fatigue process.* Journal of Polymer Science Part B: Polymer Physics, 1994. **32**(5): p. 839-849.

116. Sakaue, K., et al., *Evaluation of viscoelastic characteristics of short-fiber reinforced composite by indentation method.* Experimental mechanics, 2012. **52**(8): p. 1003-1008.

117. Celentano, D., et al., *Viscoelastic mechanical characterization of a short-fiber reinforced polyethylene tube: Experiments and modelling.* International Journal of Pressure Vessels and Piping, 2015. **134**: p. 82-91.

118. Sevostianov, I., V. Levin, and E. Radi, *Effective viscoelastic properties of short-fiber reinforced composites.* International Journal of Engineering Science, 2016. **100**: p. 61-73.

119. Zhang, Y.-Y., et al., *Experimental and theoretical investigations of the viscoelastic behaviour of short carbon fiber reinforced polyetherimide composites.* Composite Structures, 2022: p. 116016.

120. Nciri, M., et al., *Modelling and characterisation of dynamic behaviour of short-fibre-reinforced composites.* Composite Structures, 2017. **160**: p. 516-528.

121. Amiri-Rad, A., et al., *An anisotropic viscoelastic-viscoplastic model for short-fiber composites.* Mechanics of Materials, 2019. **137**: p. 103141.

122. He, G., et al., *Constitutive modeling of viscoelastic–viscoplastic behavior of short fiber reinforced polymers coupled with anisotropic damage and moisture effects.* Acta Mechanica Sinica, 2019. **35**(3): p. 495-506.

123. He, G., et al., *A combined viscoelasticity-viscoplasticity-anisotropic damage model with evolving internal state variables applied to fiber reinforced polymer composites.* Mechanics of Advanced Materials and Structures, 2021. **28**(17): p. 1775-1796.

124. Gommers, B., I. Verpoest, and P. Van Houtte, *The Mori–Tanaka method applied to textile composite materials.* Acta Materialia, 1998. **46**(6): p. 2223-2235.

125. Weber, B., et al., *Improvements of multiaxial fatigue criteria computation for a strong reduction of calculation duration.* Computational materials science, 1999. **15**(4): p. 381-399.

126. Lee, K.S., et al., *Measurement and numerical simulation of three-dimensional fiber orientation states in injection-molded short-fiber-reinforced plastics.* Journal of applied polymer science, 2003. **88**(2): p. 500-509.

127. Dean, A., et al., *Macro-mechanical modeling and experimental validation of anisotropic, pressure-and temperature-dependent behavior of short fiber composites.* Composite Structures, 2019. **211**: p. 630-643.

128. Li, Z., et al., *Multiscale modeling based failure criterion of injection molded SFRP composites considering skin-core-skin layered microstructure and variable parameters.* Composite Structures, 2022. **286**: p. 115277.

129. Wu, N., *The maximum entropy method*. Vol. 32. 2012: Springer Science & Business Media.

130. Jack, D.A., *Advanced analysis of short-fiber polymer composite material behavior*. 2006, University of Missouri--Columbia.

131. Müller, V., *Micromechanical modeling of short-fiber reinforced composites*. Vol. 6. 2016: KIT Scientific Publishing.

132. Breuer, K., M. Stommel, and W. Korte, *Analysis and evaluation of fiber orientation reconstruction methods.* Journal of Composites Science, 2019. **3**(3): p. 67.

133. Hine, P.J., H.R. Lusti, and A.A. Gusev, *On the possibility of reduced variable predictions for the thermoelastic properties of short fibre composites.* Composites science and technology, 2004. **64**(7-8): p. 1081-1088.

134. Friemann, J., *Predicting the elasto-plastic response of short fiber composites using deep neutral networks trained on micro-mechanical simulations.* 2021.

135. Mentges, N., B. Dashtbozorg, and S. Mirkhalaf, *A micromechanics-based artificial neural networks model for elastic properties of short fiber composites.* Composites Part B: Engineering, 2021. **213**: p. 108736.

136. Thomas, A.J., E. Barocio, and R.B. Pipes, *A machine learning approach to determine the elastic properties of printed fiber-reinforced polymers.* Composites Science and Technology, 2022. **220**: p. 109293.

137. Risken, H., *Fokker-planck equation*, in *The Fokker-Planck Equation*.

1996, Springer. p. 63-95.

138. Folgar, F. and C.L. Tucker III, *Orientation behavior of fibers in concentrated suspensions.* Journal of reinforced plastics and composites, 1984. **3**(2): p. 98-119.

139. Cintra Jr, J.S. and C.L. Tucker III, *Orthotropic closure approximations for flow-induced fiber orientation.* Journal of Rheology, 1995. **39**(6): p. 1095-1122.

140. Agboola, B.O., D.A. Jack, and S. Montgomery-Smith, *Effectiveness of recent fiber-interaction diffusion models for orientation and the part stiffness predictions in injection molded short-fiber reinforced composites.* Composites Part A: Applied Science and Manufacturing, 2012. **43**(11): p. 1959-1970.

141. Bauer, J.K. and T. Böhlke, *Variety of fiber orientation tensors.* Mathematics and Mechanics of Solids, 2022. **27**(7): p. 1185-1211.

142. Doghri, I. and L. Tinel, *Micromechanics of inelastic composites with misaligned inclusions: numerical treatment of orientation.* Computer methods in applied mechanics and engineering, 2006. **195**(13-16): p. 1387-1406.

143. Lloyd, S., *Least squares quantization in PCM.* IEEE transactions on information theory, 1982. **28**(2): p. 129-137.

144. ISO, *ISO 527-2: 2012. Plastics — Determination of tensile properties — Part 2: Test conditions for moulding and extrusion plastics*. 2012, ISO Geneva, Switzerland.

145. Schweidtmann, A.M., et al., *Machine learning meets continuous flow chemistry: Automated optimization towards the Pareto front of*

multiple objectives. Chemical Engineering Journal, 2018. **352**: p. 277-282.

146. Sengupta, R.N., A. Gupta, and J. Dutta, *Decision sciences: theory and practice*. 2016: Crc Press.

147. MSC Software Corporation, *DIGIMAT User's Manual.* 2019.

148. Arthur, D. and S. Vassilvitskii, *k-means++: The advantages of careful seeding*. 2006, Stanford.

149. Tseng, H.-C., R.-Y. Chang, and C.-H. Hsu, *An objective tensor to predict anisotropic fiber orientation in concentrated suspensions.* Journal of Rheology, 2016. **60**(2): p. 215-224.

150. Tseng, H.-C., R.-Y. Chang, and C.-H. Hsu, *Numerical prediction of fiber orientation and mechanical performance for short/long glass and carbon fiber-reinforced composites.* Composites Science and Technology, 2017. **144**: p. 51-56.

151. Vincent, M., et al., *Description and modeling of fiber orientation in injection molding of fiber reinforced thermoplastics.* Polymer, 2005. **46**(17): p. 6719-6725.

152. Yan, X. and S. Cao, *Structure and interfacial shear strength of polypropylene-glass fiber/carbon fiber hybrid composites fabricated by direct fiber feeding injection molding.* Composite Structures, 2018. **185**: p. 362-372.

153. Brezinová, J. and A. Guzanová, *Friction conditions during the wear of injection mold functional parts in contact with polymer composites.* Journal of Reinforced Plastics and Composites, 2010. **29**(11): p. 1712-1726.

154. Alemour, B., O. Badran, and M.R. Hassan, *A review of using conductive composite materials in solving lightening strike and ice accumulation problems in aviation.* Journal of Aerospace Technology and Management, 2019. **11**.

155. Yu, X., et al., *Graphene-based smart materials.* Nature Reviews Materials, 2017. **2**(9): p. 1-13.

156. Imran, K.A. and K.N. Shivakumar, *Graphene-modified carbon/epoxy nanocomposites: Electrical, thermal and mechanical properties.* Journal of Composite Materials, 2019. **53**(1): p. 93-106.

157. Wang, B., et al., *Fabrication of an enriched graphene surface protection of carbon fiber/epoxy composites for lightning strike via a percolating-assisted resin film infusion method.* Composites Science and Technology, 2018. **158**: p. 51-60.

158. Díez-Pascual, A.M., et al., *Influence of carbon nanotubes on the thermal, electrical and mechanical properties of poly (ether ether ketone)/glass fiber laminates.* Carbon, 2011. **49**(8): p. 2817-2833.

159. Kandare, E., et al., *Improving the through-thickness thermal and electrical conductivity of carbon fibre/epoxy laminates by exploiting synergy between graphene and silver nano-inclusions.* Composites Part A: Applied Science and Manufacturing, 2015. **69**: p. 72-82.

160. Kamaraj, M., E.A. Dodson, and S. Datta, *Effect of graphene on the properties of flax fabric reinforced epoxy composites.* Advanced Composite Materials, 2020. **29**(5): p. 443-458.

161. Wang, H., et al., *Mechanical and thermodynamic properties of unidirectional flax fiber reinforced CNT modified epoxy composites.* Fibers and Polymers, 2019. **20**(6): p. 1266-1276.

162. Cho, J., M. Joshi, and C. Sun, *Effect of inclusion size on mechanical properties of polymeric composites with micro and nano particles.* Composites Science and Technology, 2006. **66**(13): p. 1941-1952.

163. Kratochvíla, J., A. Boudenne, and I. Krupa, *Effect of filler size on thermophysical and electrical behavior of nanocomposites based on expanded graphite nanoparticles filled in low-density polyethylene matrix.* Polymer composites, 2013. **34**(2): p. 149-155.

164. Bhuiyan, M.A., R.V. Pucha, and K. Kalaitzidou, *3D RVE models able to capture and quantify the dispersion, agglomeration, and orientation state of CNT in CNT/PP nanocomposites.* Frontiers in Materials, 2016. **3**: p. 2.

165. Le, T.-T., *Probabilistic modeling of surface effects in nano-reinforced materials.* Computational Materials Science, 2021. **186**: p. 109987.

166. Firooz, S., P. Steinmann, and A. Javili, *Homogenization of composites with extended general interfaces: comprehensive review and unified modeling.* Applied Mechanics Reviews, 2021. **73**(4).

167. Chen, Q., et al., *Homogenization of size-dependent multiphysics behavior of nanostructured piezoelectric composites with energetic surfaces.* European Journal of Mechanics-A/Solids, 2022. **96**: p. 104731.

168. Giordano, S., *Order and disorder in heterogeneous material microstructure: Electric and elastic characterisation of dispersions of pseudo-oriented spheroids.* International journal of engineering science, 2005. **43**(13-14): p. 1033-1058.

169. Lielens, G., et al., *Prediction of thermo-mechanical properties for compression moulded composites.* Composites Part A: Applied

Science and Manufacturing, 1998. **29**(1-2): p. 63-70.

170. Schiebold, M., H. Schmidt, and J. Mehner, *A Finite Element Approach for Modeling and Simulation of CNT/Polymer Composites.* physica status solidi (a), 2019. **216**(19): p. 1800952.

171. Yanase, K., S. Moriyama, and J. Ju, *Effects of CNT waviness on the effective elastic responses of CNT-reinforced polymer composites.* Acta Mechanica, 2013. **224**(7): p. 1351-1364.

Abstract in Korean

섬유강화 플라스틱(FRP)은 우수한 비물성(낮은 밀도에 비하여 높은 기계적 특성 등)으로 인해 다양한 산업 제품에서 금속을 대체하여 중량 감소를 달성하는데 성공하였다. 섬유강화 플라스틱의 균질화 된 열기계적 특성을 예측하는 기능은 제품 설계 프로세스를 용이하게 하는 데 필수적이다. 그러나 이러한 특성의 균질화 과정은 섬유강화 플라스틱 내의 섬유가 갖는 미세 구조의 다양성으로 인해 간단하게 진행될 수 없다. 본 연구에서는 미세구조의 다양성을 고려하여 균질화 된 열기계적 특성을 높은 정확도로 계산할 수 있는 머신러닝 기반의 열기계적 균질화 프레임워크를 제시하고자 한다.

2장에서는 미세구조 섬유배열의 무작위성을 고려한 단방향(UD) 섬유강화 플라스틱의 기계학습 기반 인장강도 예측모델을 제안한다. 끊어진 섬유에 의해 생성된 응력집중계수(SCF)는 단방향 섬유강화 플라스틱의 인장강도를 결정하는 지배적인 특성이다. 그러나 일반적으로 단방향 섬유강화 플라스틱의 무작위로 분포된 섬유에 대하여 응력집중계수 계산을 위한 구성방정식은 제안 되어있지 않다. 저자는 임의의 단방향 섬유강화 플라스틱에서 응력집중계수를 일반적으로 계산해낼 수 있는 새로운 기계 학습 기반 모델링을 제안한다. 다양한 무작위 섬유 배열을 갖는 단방향 섬유강화 플라스틱에 대하여 막대한 양의 유한 요소 시뮬레이션을 수행하여 응력집중계수 데이터를 축적하였다. 획득한 응력집중계수 데이터로 인공 신경망(ANN)을 훈련하였고, 이를 사용하여 임의의 무작위 섬유 배열이 있는 복합 재료의 응력집중계수를 예측할 수 있는 것을 확인하였다. 인장 강도 예측 모델의 경우 섬유 파단 전파에 대한 새로운 점화식과 무작위 섬유 배열에 대한 파단 순서 결정 알고리즘을 기반으로 개발되었다. 개발된 방법론을 검증하기 위해 실제 단방향 섬유강화 플라스틱의 물성을 활용하여 인장 강도를 예측하고 이를 실험값과 비교하였으며, 이를 통해 기존 예측 방법보다 우수함이 입증되었다.

3장에서는 단섬유 강화 플라스틱(SFRP)에 대한 기계 학습 기반의

2단계 균질화 프레임워크를 제안한다. 함유물의 배향에 따라 열기계적 물성의 이방성이 서로 다르게 발현하기 때문에 배향에 대한 고려가 매우 중요하다. 시간이 많이 소요되는 섬유 배향 분포함수 재구축 및 유사결정립 분해 과정을 용이하게 하기 위해 직병렬 구조의 인공신경망 시스템을 구성하고 충분히 많은 양의 데이터로 훈련하였다. 직병렬 구조의 인공신경망 시스템, Mori-Tanaka 균질화 모델 및 Voigt 균질화 모델을 ABAQUS UMAT(User Material Subroutine)에 구현하였다. 개발된 UMAT에 의해 예측된 탄성 계수 값은 실험 값과 비교하여 잘 일치하는 것이 확인되었으며, 낮은 계산 소요를 보여주어 머신러닝 적용의 당위성 또한 확인되었다.

4장에서는 단섬유 강화 플라스틱에 대해 이전 장에서 개발된 2단계 균질화 프레임워크를 확장하기 위하여, 섬유와 함유물 사이에 일정한 나노 크기의 두께를 갖는 계면상의 개념을 도입하였고, 이를 통해 보다 일반적인 재료를 설명할 수 있게 되었다. 이 세 번째 계면상의 도입을 통해 추가적으로 함유물의 크기 효과 또한 균질화 프레임워크에서 고려될 수 있음이 확인되었다. 확장된 균질화 프레임워크의 재료 설계에의 적용 가능성이 유한 요소 시뮬레이션을 통해 얻은 균질화 된 열기계적 특성과 비교 검증되어 확인되었다.

주요어: 섬유강화 플라스틱, 복합재료, 2단계 균질화, 열기계적, 미세구조, 인공신경망

학 번: 2017-24086